IMPROVEMENT OF SILICON HETEROJUNCTION SOLAR CELL PERFORMANCE WITH NEW SURFACE STRUCTURE AND WIDE BAND GAP CARRIER SELECTIVE LAYERS

A THESIS SUBMITTED TO
THE GRADUATE SCHOOL OF NATURAL AND APPLIED SCIENCES
OF
MIDDLE EAST TECHNICAL UNIVERSITY

BY

ERGİ DÖNERÇARK

IN PARTIAL FULFILLMENT OF THE REQUIREMENTS
FOR
THE DEGREE OF DOCTOR OF PHILOSOPHY
IN
MICRO AND NANOTECHNOLOGY

OCTOBER 2021

Approval of the thesis:

IMPROVEMENT OF SILICON HETEROJUNCTION SOLAR CELL PERFORMANCE WITH NEW SURFACE STRUCTURE AND WIDE BAND GAP CARRIER SELECTIVE LAYERS

submitted by **ERGİ DÖNERÇARK** in partial fulfillment of the requirements for the degree of **Doctor of Philosophy** in **Micro and Nanotechnology, Middle East Technical University** by,

Prof. Dr. Halil Kalıpçılar
Dean, Graduate School of **Natural and Applied Sciences**

Prof. Dr. Almıla Güvenç Yazıcıoğlu
Head of the Department, **Micro and Nanotechnology**

Prof. Dr. Raşit Turan
Supervisor, **Physics, METU**

Assoc. Prof. Dr. Selçuk Yerci
Co-Supervisor, **Micro and Nanotechnology, METU**

Examining Committee Members:

Prof. Dr. Hüsnü Emrah Ünalan
Metallurgical and Materials Eng., METU

Prof. Dr. Raşit Turan
Physics, METU

Assist. Prof. Dr. Ayşe Seyhan Sürmegözlüer
Physics, Niğde Ömer Halisdemir University

Assoc. Prof. Dr. Tahir Çolakoğlu
Physics Eng., Ankara University

Assoc. Prof. Dr. Alpan Bek
Physics, METU

Date: 15.10.2021

I hereby declare that all information in this document has been obtained and presented in accordance with academic rules and ethical conduct. I also declare that, as required by these rules and conduct, I have fully cited and referenced all material and results that are not original to this work.

Name Last name : Ergi Dönerçark

Signature :

ABSTRACT

IMPROVEMENT OF SILICON HETEROJUNCTION SOLAR CELL PERFORMANCE WITH NEW SURFACE STRUCTURE AND WIDE BAND GAP CARRIER SELECTIVE LAYERS

Dönerçark, Ergi
Doctor of Philosophy, Micro and Nanotechnology
Supervisor: Prof. Dr. Raşit Turan
Co-Supervisor: Assoc. Prof. Dr. Selçuk Yerci

October 2021, 184 pages

The photovoltaic (PV) industry is dominated by silicon-based solar cells owing to the abundance of silicon and its full-fledged technology. The main road for the PV industry points out to enhance the conversion efficiency of solar cells while decreasing production costs, which is crucial for improving renewable energy market share. The silicon heterojunction solar cells (SHJ) are receiving attention on this road map due to their higher conversion efficiencies, simple process flow, and low-temperature fabrication sequence. In order to further enhance the SHJ device performance, both electrical and optical properties should be improved simultaneously.

In this Ph.D. thesis work, various aspects of SHJ solar cells, such as surface texturing, surface passivation, and material choices, were addressed. Firstly, surface texturing was studied to search for new approaches to reduce optical losses. Even though the well-established surface texturing method generating random pyramids on the surface reduces the reflection successfully, there is still room for improvement. A new and novel silicon surface texturing method based on copper-assisted chemical etching was developed for efficient light management on the surface. With this technique, tetragonal-star shaped inverted pyramids were formed, resulting in extremely low reflectance values.

Secondly, the surface passivation of silicon was studied using different process conditions and material systems. The SHJ solar cell performance was significantly improved by understanding the chemical passivation kinetics and improving the surface passivation quality.

Thirdly, wide band gap materials were integrated into the SHJ solar cell structure to decrease parasitic absorption losses. Furthermore, the free-carrier absorption losses were reduced significantly by tuning TCO's electrical and optical properties. Based on the theoretical and experimental explanations, the novel method for light trapping and integration of wide band gap materials to SHJ solar cell structure were shown to offer promising alternatives to existing technologies for future applications. With these new material systems and process improvements, we have achieved high-efficiency values of up to 21.2% in the SHJ solar cells fabricated at ODTÜ-GÜNAM.

Keywords: Silicon Heterojunction Solar Cells, Copper Assisted Chemical Etching, Surface Passivation, Wide Band Gap Material, Carrier Selective Contacts.

ÖZ

YENİ YÜZEY YAPISI VE GENİŞ BANT ARALIKLI TAŞIYICI SEÇİCİ KATMANLARIYLA SİLİKON HETEROEKLEM GÜNEŞ HÜCRESİ PERFORMANSININ İYİLEŞTİRİLMESİ

Dönerçark, Ergi
Doktora, Mikro ve Nanoteknoloji
Tez Yöneticisi: Prof. Dr. Raşit Turan
Ortak Tez Yöneticisi: Doç. Dr. Selçuk Yerci

Ekim 2021, 184 sayfa

Fotovoltaik endüstrisi, hammade çokluğu ve tam gelişmiş teknolojisine dayanarak silisyum tabanlı güneş hücreleri tarafından domine edilmiş durumdadır. Fotovoltaik endüstrisinin esas yol haritası, güneş hücrelerinin verim değerini arttırırken üretim maliyetlerini de düşürmektir. Bu yol haritasında silisyum heteroeklem güneş hücreleri görece yüksek dönüşüm verimi, basit üretim akışı ve düşük sıcaklık üretim adımları nedenleriyle dikkat çekmeye başlamıştır. Cihaz performansını daha da arttırmak için ise hem elektriksel hem de optik özellikler eş zamanlı geliştirilmelidir.

Bu doktora tez çalışmasında, SHJ güneş hücrelerinin yüzey yapısı, yüzey pasivasyonu ve malzeme seçimleri gibi çeşitli yönler ele alındı. İlk olarak, optik kayıpları azaltmak için yeni yaklaşımlarla yüzey yapılandırılması üzerinde çalışıldı. İyi bilinen yüzey yapılandırma metodu olan rastgele dağılımlı piramit oluşturma, spektral yansıma profilinde kayda değer bir iyileştirme sağlamasına rağmen, optik kayıpların azaltılması noktasında hala iyileştirme için yer bulunmaktadır. Yüzeyde daha iyi ışık yönetimi için bakır destekli kimyasal aşındırmaya dayalı yeni ve özgün bir silisyum yüzey yapılandırma yöntemi geliştirildi. Bu teknikle tetragonal yıldız taban şekilli ters piramitler oluşturularak son derece düşük yansıma değerleri elde edilmiştir.

İkinci olarak, farklı proses koşulları ve malzeme sistemleri kullanılarak silisyum yüzey pasivasyonu incelenmiştir. Kimyasal pasivasyon kinetiğini anlayarak ve yüzey pasivasyon kalitesini geliştirerek SHJ güneş hücre performansı önemli ölçüde iyileştirildi.

Üçüncü olarak, parazitik emilim kayıplarını azaltmak için SHJ güneş hücre yapısına geniş bant aralıklı malzemeler entegre edildi. Ayrıca, TCO'nun elektriksel ve optik özellikleri ayarlanarak serbest taşıyıcı emilim kayıpları önemli ölçüde azaltıldı. Teorik ve deneysel açıklamalara dayanarak, yeni geliştirilen ışık yakalama yöntemi ve geniş bant aralıklı malzemelerin SHJ güneş hücre yapısına entegrasyonu gelecekteki alternatif uygulamalar için umut verici sonuçlar sunmaktadır. Bu yeni malzeme sistemleri ve proses iyileştirmeleri ile ODTÜ-GÜNAM'da üretilen SHJ güneş hücrelerinde %21,2'ye varan yüksek verim değerleri elde ettik.

Anahtar Kelimeler: Silisyum Heteroeklem Güneş Hücreleri, Bakır Destekli Kimyasal Aşındırma, Yüzey Pasivasyonu, Geniş Bant Aralıklı Malzemeler, Taşıyıcı Seçici Kontaklar.

To my family

ACKNOWLEDGMENTS

First of all, I would like to thank my supervisor Prof. Dr. Raşit Turan, for the endless support, guidance, and inspiration during my study. I express my gratitude to him for his informative attitude about academic and professional points of view. I would like to give special thanks to my co-supervisor, Assoc. Prof. Dr. Selçuk Yerci, for his support and guidance during my study.

I am very grateful to members of the thesis monitoring committee, Prof. Dr. Hüsnü Emrah Ünalan, and Assist. Prof. Dr. Ayşe Seyhan Sürmegözlüer, for their suggestion, comments, and contributions during thesis study. I would like to present my sincere thanks to Prof. Dr. Ayşe Çiğdem Erçelebi for her valuable comments, informative discussion, and endless support.

I would like to express my deepest gratitude to Assoc. Prof. Dr. Tahir Çolakoğlu for giving ideas forming the basis of the thesis and sharing his experimental and theoretical knowledge. I would like to send my deepest thanks to E. Hande Çiftpınar for her endless support during experimental studies, friendship, and for sharing her knowledge with me. I also want to thank Salar H. Sedani for his support during the analyzes, fruitful discussions, and worthful friendship. Next, I am grateful to Deniz Türkay for his precious contributions, creative ideas, and nice friendship. I would also like to thank Dr. Hisham Nasser for his help during experimental studies. I would like to express my thanks to Dr. Mehmet Koç and Konstan Tsoi for their collaboration and kind friendship. I would also like to acknowledge the colleagues from SHJ group Dr. İsmail Kabaçelik, Arghavan Salimi, Alp Ege Aytaç, Seçil Güler, Seda Kılıçkaya, Büşra Altınsoy, Milad Ghasemikashtiban and Sümeyye Koçak.

I would like to thank my roommate Samet Özdemir for his friendship and support. I am grateful to Dr. Makbule Terlemezoğlu for her nice friendship, support, and motivational talks. I am grateful to Musa Kurtuluş Abak for his dignified friendship, kindness, creativity, and productivity.

I want to thank all ODTÜ-GÜNAM family, including researchers, administrative and technical personnel, for their support during thesis studies.

I acknowledge the financial support from the Scientific and Technological Research Council of Turkey (TÜBİTAK) under grant numbers 217M087, 217M203, and 20AG002.

My last words go to the people I owe the most. I would like to thank my lovely family, including “Prenses”. I am grateful to them for everlasting support, love, guidance, and help. I want to express my special gratitude to Dad (you will always be with us). Finally, my most significant appreciation goes to my love (Özün Candemir) and children: Tri, Çaki, and Junior. Without your endless support, love, understanding, care, and kisses. I could have never reached this step. I love you!

TABLE OF CONTENTS

LIST OF TABLES

LIST OF FIGURES

LIST OF ABBREVIATIONS

a-Si:H	Hydrogenated amorphous silicon
AM1.5	Air Mass 1.5
Al	Aluminum
ARC	Antireflection coating
BSF	Back surface field
CB	Conduction band
c-Si	Crystalline silicon
Cz	Czochralski
CVD	Chemical Vapor Deposition
HF	Hydrofluoric acid
IBC	Interdigitated back contact
ICP	Inductively Coupled Plasma
KOH	Potassium hydroxide
mc-Si	Multicrystalline silicon
PECVD	Plasma enhanced chemical vapor deposition
PV	Photovoltaic
RIE	Reactive ion etching
SEM	Scanning Electron Microscope
SiN_x	Silicon nitride
SiO_2	Silicon dioxide
TEM	Transmission Electron Microscopy

TCO	Transparent Conductive Oxide
TMAH	Tetramethylammonium hydroxide

LIST OF SYMBOLS

E	Energy
E_G	Energy band gap
FF	Fill factor
I_{SC}	Short circuit current
J	Current density
J_{mpp}	Current density at the maximum power point
J_0	Dark saturation current density
J_{SC}	Short circuit current density
N_D	Doping concentration
P_{mpp}	Power density at the maximum power point
R	Reflectance
R_S	Series resistance
R_{SH}	Shunt resistance
T	Transmittance
V	Voltage
VB	Valence band
V_{mpp}	Voltage at the maximum power point
V_{oc}	Open circuit voltage

CHAPTER 1

INTRODUCTION

1.1 Energy and Environment

> *“You cannot escape the responsibility of tomorrow by evading it today.”*
>
> Abraham Lincoln

Numerous scientists, politicians, governments, and organizations are taking and have been taken responsibility for tomorrow's needs by shaping today's global energy policies. The overall energy demand of the world significantly increases each year, whereas fossil fuels (oil, gas, and coil) are used as the primary energy resource to fulfill this demand. The historical trend of energy consumption by resource and level of carbon dioxide (CO_2) emissions can be found in Figure 1.1 [1]. Even though there are some fluctuations in the energy consumption where the responsible actor on the decrease is the global crisis, most of them were economic; the global energy demand is increasing day-by-day tremendously due to the expansion of population, factories, technologies, and daily needs. In 2020, 88% of all energy consumption worldwide was provided by fossil fuels, while only 12% of the consumption came from renewable resources [1].

The use of unsustainable fossil fuels poses a significant threat concerning CO_2 emissions, which has some inevitably dangerous results and problems for our the one and only world due to global warming, also known as the greenhouse effect. Global warming is presumed to be the most eminent problem of the 21st century [2], [3]. The restrictions and decisions to be established in the upcoming years may affect the market share and cost of fossil fuels.

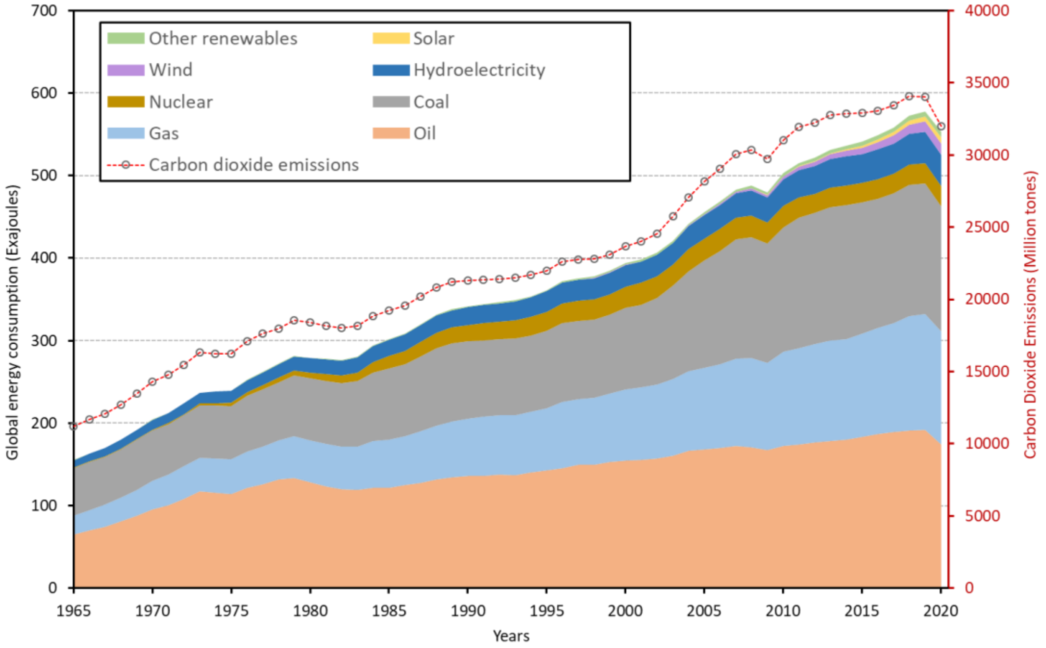

Figure 1. 1. Global energy consumption and carbon dioxide emission over the years [1].

Predictions on the resources and demand of energy have been varying, and there are controversial discussion topics between annual reports of different research groups. In the 2020 World Energy Outlook, the International Energy Agency estimated that the present fossil fuel reserves would not last through another century, and solar energy would become the top energy resource by the end of 2040. However, the World Coal Association reported that the current coal reserves are enough to last throughout the next century [4]. Regardless of which prediction comes to pass, there are two crucial realities: there is an enormous demand for energy, and the excessive amount of CO_2 emissions affect all life on Earth.

"The Stone Age didn't end for lack of stone, and the Oil Age will end long before the world runs out of oil."

Ahmed Zaki Yamani – Minister of oil for Saudi Arabia

The world, and we as its residents, are going through a period of transition regarding the use of renewable and sustainable energy sources. This transition is not a choice but an obligation to stop the use of fossil fuels for our energy needs. The global temperature has increased by almost 0.75°C during the last century due to the greenhouse effect. If the rate of temperature rise continues at this pace, the global temperature may increase up to 4°C by the end of this century [5]. Plants, animals, and ecosystems rapidly face long-term challenges as the global changes reduce genetic variation and increase extinction rates [6], [7]. Scientists, organizations, especially governments and politicians, take action and undertake the responsibility to build future energy resources to overcome impending environmental problems to save our world.

One way of fulfilling the energy demand is developing, using, and integrating renewable and sustainable energy sources instead of fossil fuels. Figure 1.2 [4], [8] shows the estimated capacity of finite reserves and renewable resources. As shown in representative comparisons, the available energy from renewables is much higher than today's global energy demand. The sun can provide more power in a single year than the sum of all finite energy resources.

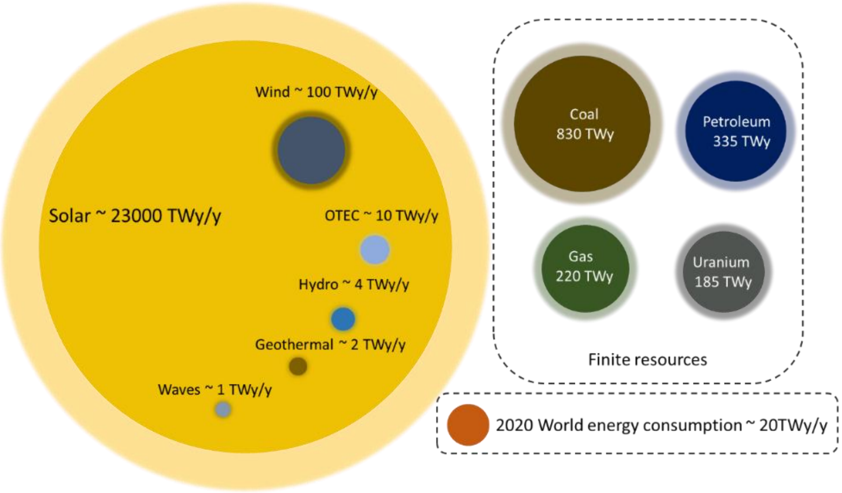

Figure 1. 2. Estimated capacity of renewable and conventional/finite resources and global energy consumption in 2020 [4], [8].

Renewable resources have become more attractive over the last decade, where the capacity of used renewables increased almost two times compared to capacities in

2010 and 2020 [9]. Moreover, in 2020 the total energy generation by wind and photovoltaics (PV) reached 744 GW and 505 GW, respectively. Among other renewable resources, the highest proportional increase in the last five years has been recorded in PV solar energy, while the annual growth of PV energy capacity is over 25% [9].

1.2 Photovoltaic Technologies

Solar energy can be converted to electricity directly through PV devices. The understanding of the working principle of PV devices bases on the discovery of the photovoltaic effect by Becquerel in 1839. Forty years after the photovoltaic effect was found, the first PV device was developed by W. Adams and R. Day based on understanding the interaction mechanism between selenium and solar irradiation [9]. Goldman and Brodsky further clarified the relationship between PV and metal/semiconductor interface in 1914, and the theory behind the metal/semiconductor interaction was explained by W. Schottky et al. in the 1930s [10].

Later, in the 1950s, PV properties were improved by established technology in silicon (Si) electronics devices. Chapin, Fuller, and Pearson reported the first Si solar cell with an efficiency of 6% in 1954, while the same year, a cadmium sulfide solar cell with 6% efficiency was also developed [11]. In the 1970s, one of the research trends was finding new materials for cheaper and more efficient production of PV devices together with different structures such as multiple band gap solar cell structures. In the second half of the 1990s, PV module production increased by more than 15% per year. The evolution of different solar cell technologies is shown in Figure 1.3. With today's technology, the best research solar cell efficiency could reach up to 47% using multijunction design. Even though higher efficiency is achieved by multijunction solar cells, due to the abundance of silicone on earth and low manufacturing costs, the PV market is dominated by Si-based technologies, with a share of more than 90%. Today Si-based solar cells with efficiencies higher than

26% and 25% efficiencies have been achieved in research laboratories and factories, respectively.

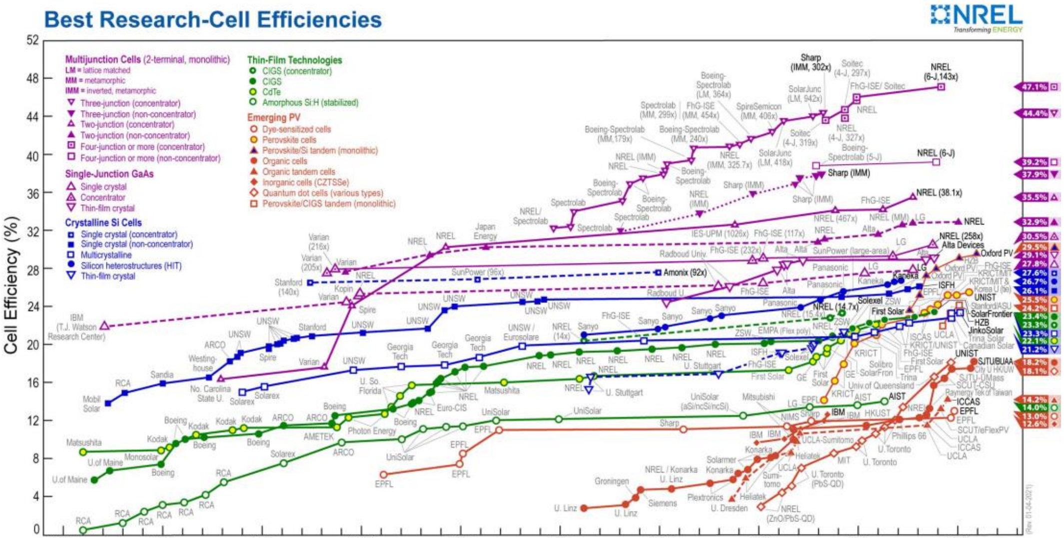

Figure 1. 3. Evolution of various solar cell technologies in terms of cell efficiencies [12].

In 2020, almost 95% of total PV production adopted Si solar cell technologies, where 80% of them used monocrystalline silicon (c-Si) substrate. For the last decade, Si PV has held more than 90% of the global market share (see Figure 1.4) [13].

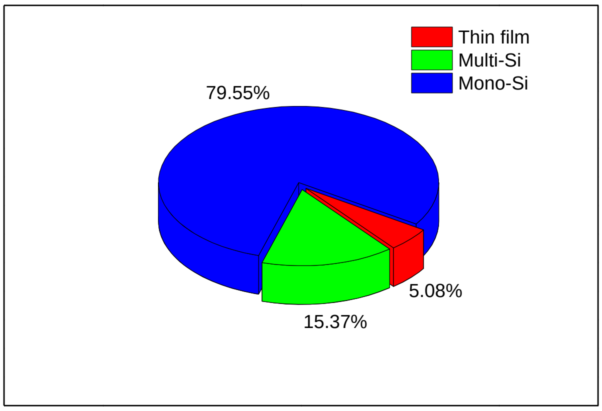

Figure 1. 4. The market share of PV production by different technologies in 2020 [13].

Today, the c-Si technology is dominated by passivated emitter solar cells. The most commonly used structure is Passivated Emitter Rear Cells (PERC). Moreover, passivated solar cell structures hold 80% of the c-Si solar cell market. However, the next generation of this technology is predicted to be Tunnel Oxide Passivated CONtact (TOPCon). The oldest c-Si solar cell technology, Aluminum Back Surface Field (Al-BSF), follows right after; and had a market share of more than 15% in 2020, although this percentage has been decreasing each year. The third and fourth leading technologies are Silicon Heterojunction (SHJ) and back contacted solar cells, each holding approximately 2% of the market in 2020. According to the International Technology Roadmap for Photovoltaic (see Figure 1.5), SHJ solar cell technology will keep more than 15% of the market share in the next ten years, having the most significant proportional increase compared to the other technologies [14].

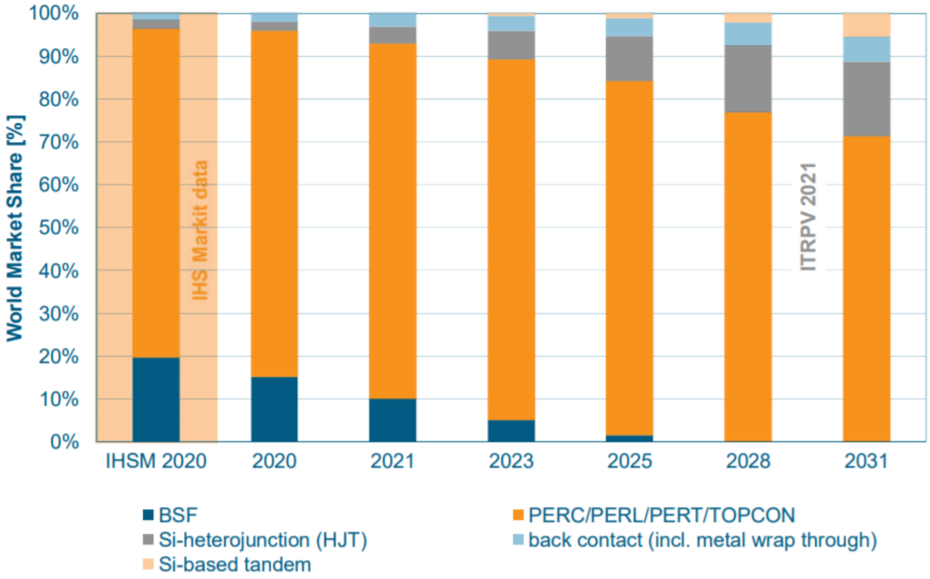

Figure 1. 5. Projected c-Si solar market share by different technologies [14].

1.2.1 The Learning Curves of Renewables

The learning curve of the module selling price (US$/$W_p$) as a function of cumulative shipments (MW) is represented in Figure 1.6. According to historical price data, the learning rate has been 23.8% from 1976 to 2020, implying that the average reduction in price for each cumulative shipment is 23.8%. Turning our focus on to the period between 2006 and 2020, we can observe that the learning rate has increased up to 40%, while the learning rate values are 1.4% for hydroelectricity [15], varying between 11-35% for wind [16]–[18] and 7-10% for biomass [19]. Among all other renewables, PV technologies have the highest learning rate.

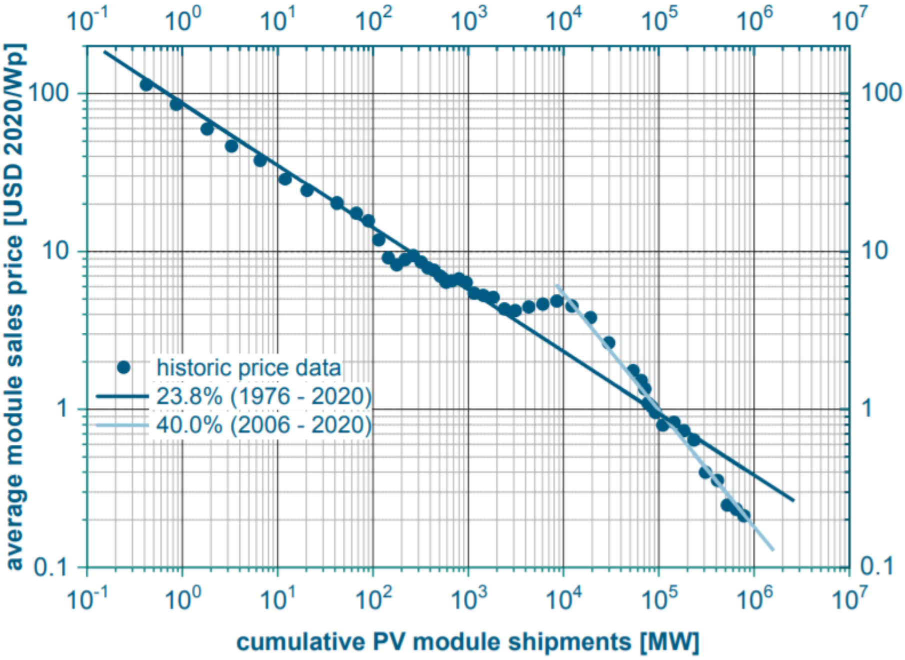

Figure 1. 6. The learning curve of module price as a function of cumulative shipments [14].

Decreasing the Levelized Cost of Energy (LCOE) is the deterministic parameter for technological trends in the PV market and especially for c-Si solar cell technologies. Between 2010 and 2019, the LCOE of c-Si technology was reduced from 0.38 to 0.04 US$/kWh, causing it to become one of the promising technologies of today and the future [19]. The general trends and projections in c-Si solar cell technology are as follows:

- Decreasing the c-Si wafer fabrication prices during the past five years has influenced the market preference, from mc-Si to c-Si. At present, the market is dominated by c-Si wafers.
- The size of the wafers has been increasing to over 210.0×210 mm^2.

- Production of bifacial solar cells is on the rise as opposed to mono facial solar cells.
- There are two different methods of metallization higher number of busbars more than 9 and busbarless metallization technique.
- The half-cell module configuration is leading the c-Si market resulting in modules with higher efficiency.
- Module sizes are also increasing from 1.7 m^2 to above 1.8 m^2.

The fabrication capacity of SHJ solar cells has been sharply increasing since 2018. Considering the announcement of expansion plans for SHJ solar cell factories, the total fabrication capacity is expected to increase by five times compared to the capacity at the beginning of 2021 [20]. The key to the widespread attention on SHJ solar cells is the reduced costs in the fabrication line. In 2019, the fabrication line prices for SHJ solar cells decreased by more than half [20]. Despite having a lower share in the PV market today, SHJ technologies have shown the highest efficiency rates in both laboratory and factory scales; and should be considered as a good candidate for the market.

1.3 Silicon Heterojunction Solar Cells

SHJ solar cells owe their success to a thin and high-quality passivation layer that is inserted between recombination-active contacts and c-Si surface with a relatively high band gap material. The intrinsic a-Si:H buffer layer, which has a slightly higher band gap (1.7eV) than c-Si, plays a crucial role in the passivation quality. The band diagram and sectional view of an SHJ solar cell can be seen in Figure 1.7. Two barriers occur in the carrier flow direction; however, tunneling does not necessarily occur in SHJ devices, and diffusive transport of carriers can be just as important [21].

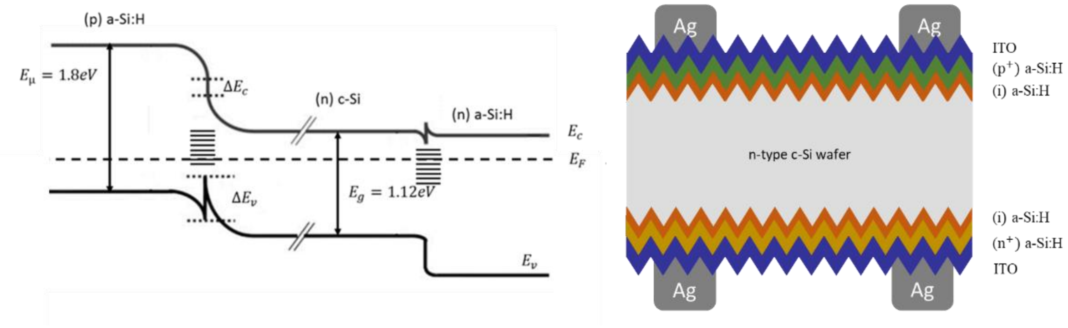

Figure 1. 7. The band gap diagram (left) and sectional view (right) of SHJ solar cell.

Plasma Enhanced Chemical Vapor Deposition (PECVD) technique is a commonly adopted method in fabricating SHJ solar cells. This deposition technique also simplifies the fabrication procedure of (i) a-Si:H and in situ doping of a-Si:H layers. The ability to dope and control the electrical conductivity of a-Si:H by using phosphine (PH_3) and diborane (B_2H_6) was discovered in 1975 [22]. Nevertheless, the doping efficiency of a-Si:H was relatively low compared to the doping efficiency of c-Si. The auto-compensation model explained the low doping efficiency, where maximum doping of a-S:H layers is limited due to its self-inhibiting nature [23].

The first solar cell to use a thin a-Si:H layer for passivation purposes was reported in 1983 by Hamakawa and coworkers; it was in the form of a-Si:H/poly-Si heterojunction solar cell in tandem design. They later referred to as the Honeymoon cell due to the advantages in material combination where the structure was a-Si/poly-Si and CdS/CdTe tandem solar cell [24], [25]. In 1992, Sanyo demonstrated the potential of a-Si:H technology and heterojunction solar cell structure. Sanyo was successful in serial production of heterojunction solar cells with an intrinsic thin layer technology that had a module efficiency value of 14.4%, and these solar cells were marketed under the brand name “HIT” [26], [27]. After the acquisition in 2012, Sanyo's solar modules started to be sold under "Panasonic." Panasonic has achieved a record conversion efficiency of 24.7% on the slightly thinner c-Si substrate (~100μm) [28]. Later, Panasonic reported another new record conversion efficiency of 25.6% by reducing recombination rate and optical gain, using the Interdigitated

Back Contact (IBC) design [29]. However, in 2017, Kaneka Corporation broke this record by attaining a conversion efficiency of 26.63%, which is the world record for cell efficiency value until now [30]. The evolution of SHJ solar cell conversion efficiencies over the years can be found in Figure 1.8.

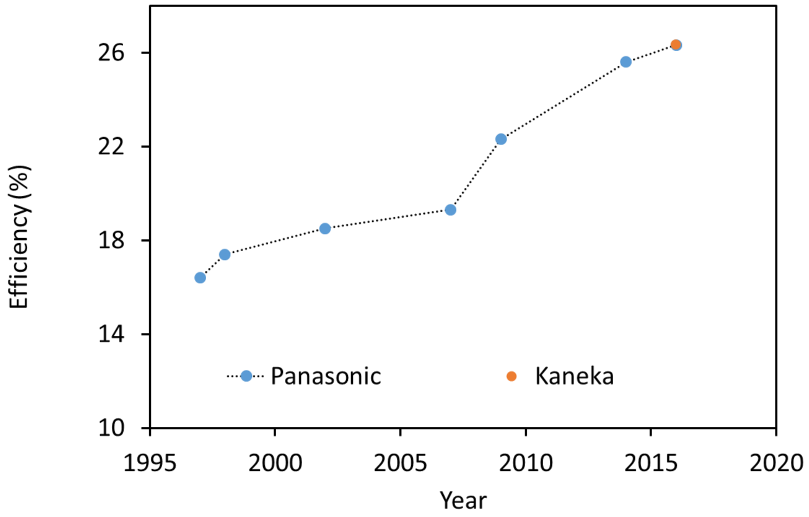

Figure 1. 8. Evolution of SHJ solar cell conversion efficiencies over the years.

Apart from Sanyo and Kaneka, several other groups and industrial companies reported a value above 24% PCE on SHJ solar cells. In addition to the successful application of SHJ solar cells on a laboratory scale, Meyer Burger AG announced more than 23% efficient SHJ solar cells from their pilot mass production line in 2017 [31], after which they also reported efficiency values of 24% and above [32]. Their fully automated pilot line is capable of a 200,000 cells/day throughput for 6 inch Si wafers [31]. Enel Green Power – the 3SUN factory has announced their SHJ solar cell efficiency as 24.63% and a production line with a capacity of 200 MWp/year [33]. Hanergy [34], ENEL [35], and Longi [36] have also announced more than 25% efficiency values for their commercial SHJ solar cell fabrication lines. The interest in SHJ solar cells and the market share are significantly increasing every year, and as a result, SHJ technology is one of the most studied research topics. The SHJ-IBC solar cells are getting great attention and seem to be one of the candidates for future high-efficiency PV. There are various methods to pattern rear side of solar cells:

using shadow mask deposition [37], [38], etching a-Si:H layers (wet [39], [40] and dry [41]–[43]), lift-off [44], [45], screen and ink-jet printing [46], [47] and laser ablation [48]. The efficiency values of various patterning techniques are given in Table 1.1. The record efficiency value was achieved by wet chemical etching of layers due to relatively sensitive patterning behavior on the rear side. However, this method includes photolithography to form the interdigitated pattern on the rear side; thus, the fabrication costs are higher. Moreover, the technique having the second-highest efficiency value, the shadow mask with tunnel junction, managed to reach 24.8% efficiency with a simplified process flow and low-cost capability. SHJ-IBC solar cell process flow is still in development for mass production. The major difficulty with this technology is the patterning procedure of the rear side. Still, the simplification of fabrication processes of IBC solar cells is a challenging topic when it comes to mass production.

Table 1. 1. SHJ-IBC solar cell results of different patterning techniques.

Institute	Technology	Patterning Method	Efficiency (%)
SHARP	SHJ-IBC	Wet etching	25.1
HZB	SHJ-IBC	Wet etching	22.0
imec	SHJ-IBC	Wet etching	22.6
imec	SHJ-IBC	Dry etching	22.9
imec	SHJ-IBC	Lift-off	23.3
EPFL-CSEM	SHJ-IBC	Shadow mask	22.9
EPFL-CSEM	SHJ-IBC	Shadow mask with tunnel junction	24.8
CEA-INES	SHJ-IBC	Laser ablation	19.0
imec	SHJ-IBC	Laser ablation and lift-off	22.5
CEA-INES	SHJ-IBC	Screen printing	15.7
AIST	SHJ-IBC	Inkjet printing	15.1

The SHJ solar cell technology has some key roles and advantages compared to others, as listed below:

- Relatively lower fabrication process temperature,

- High-quality interface properties resulting in low defect density ($<10^{10}$ cm^{-2}) [49] with perfect passivation properties,
- Low-temperature coefficient compared to homojunction silicon solar cells which means that SHJ solar cells have higher performance under high-temperature operations.

1.4 Thesis Outline

This thesis focuses on improving the electrical and optical properties of SHJ solar cells by using a novel light trapping technique, increasing a-Si:H passivation quality, and integration of wide band gap materials into the solar cell structure.

In Chapter 2, simulation results of different SHJ solar cell configurations are reported. The impact of bulk and interface quality on device performance was investigated. The relationship between the band gap of the emitter and solar cell parameters was clarified, and the optimum band gap was determined.

In Chapter 3, the etching mechanism of the copper-assisted etching technique was clarified, resulting in the novel surface structure of tetragonal-shaped inverted pyramids, allowing us to obtain extremely low surface reflectance.

In Chapter 4, firstly, the passivation properties of a-Si:H layer under various deposition conditions were analyzed and discussed, correlating with "H" contents and interface trap densities. Then, the impact of contaminants on the passivation quality was traced. Finally, Passivation properties of wide band gap amorphous silicon carbide were analyzed under various deposition conditions.

Chapter 5 deals with the properties of doped a-Si:H and a-SiC_x:H layers allowing wide band gap emitter, and properties of molybdenum oxide and lithium fluoride layer as an application of hole and an electron selective layer.

In Chapter 6, the best deposition conditions improved, and obtained previous chapters were implanted to fabricate SHJ solar cells. The impact of each layer on the solar cell parameters was discussed and analyzed, resulting in more than 21% efficient SHJ solar cells.

Chapter 7 concludes the main findings and their correlations between device performance and provides an outlook for future researches.

CHAPTER 2

SIMULATION OF SILICON HETEROJUNCTION SOLAR CELLS

“All laws are simulations of reality.”

John C. Lilly

In this chapter, Afors-HET v2.5 was used to model doping concentration, layer thickness, bulk quality of c-Si and interference properties to identify how these properties affect solar cell parameters.

2.1 Introduction

The Afors-HET simulation program is generally used for modeling multi-layer homo and heterojunction solar cells in one dimension. The AforsHet v2.5 is capable of applying various characterization techniques on solar cells, including the standard current-voltage (I-V) characterization, quantum efficiency, capacitance-voltage (C-V), and photoluminescence (PL). In this study, I-V and QE characterization techniques were used to analyze to observe how solar cell parameters are affected by the n and p doping concentration values, the thickness of each layer, the relationship between bulk lifetime of c-Si and V_{oc}, and the interface defects [50], [51].

2.1.1 Optical Modelling

The generation rate of electron and hole pairs due to the absorption of photons in the structure is described by the distinct generation through super-band gap and sub-band gap mechanisms. The optical modeling only considers the super-band gap generations, where the photon absorption takes place for $E_{photon} > E_g$ only. The optical generation rate is equal for electrons and holes, as given in the following equation [52]:

$$G(x,t) = G_N(x,t) = G_p(x,t). \qquad \text{(Eq.2.1)}$$

Two optical models are available through AforsHet v2.5: Lambert-Beer absorption and coherent/incoherent internal multiple reflections. A textured surface is used in the first model, and reflections in multiple internal boundaries are taken into account; however, it neglects the coherence effect. Throughout this work, the Lambert-Beer absorption model was used. Coherence effects are considered in the second model, but this can only be applied to planar surfaces. Reflectance and absorbance data are available in the library of the program. The incoming spectral photon flux ($\Phi_0(\lambda,t)$) is weighted with the contact reflection and absorption. The incidence angle of incidence δ of the incoming light is adjustable for both textured and flat surfaces, where the textured surface was used in the study. The angle γ by which the light travels through the layer stack depends on the wavelength of the incoming light and is calculated according to Snell's law [52]:

$$\gamma(\lambda) = \delta - \arcsin\,(\sin(\delta)\,.\frac{1}{n(\lambda)})\,, \qquad \text{(Eq.2.2)}$$

where $n(\lambda)$ is the wavelength-dependent refractive index of the first semiconductor layer in the illuminated side of the structure. Note that within this model, the variation in $\gamma(\lambda)$ is neglected when the light passes through a semiconductor/semiconductor layer interface with two different refractive indices. Therefore, it is assumed that all photons with a specified wavelength cross the layer stack under a distinct angle γ.

Photon absorption is then calculated from the spectral absorption coefficient $\alpha_x(\lambda) = 4\pi k(\lambda)/\lambda$ of the semiconductor layer corresponding to the position x within the structure, which is calculated from the provided extinction coefficient $k(\lambda)$ of the layer. The super band gap electron and hole generation rate for one single run through the stack layer (no multiple passes) is then given by [52]:

$$G(x,t) = \int_{\lambda_{min}}^{\lambda_{max}} d\lambda.\, \phi_0(\lambda,t).\, R(\lambda).\, A(\lambda).\, \alpha_X(\lambda)\, .\, e^{-\alpha_x(\lambda)/\cos(\gamma)} \quad \text{(Eq.2.3)}$$

Internal reflections and refractions within the solar cell layers are neglected.

2.1.2 Electrical Modeling

The Poisson and the continuity equations are solved for both electrons and holes for all semiconductor layers. Moreover, each semiconductor/semiconductor interface can be described by different physical models. The electron density n(x,t), the hole density p(x,t), and the electric potential ϕ(x,t) are the independent variables for which differential equations are solved. It can be solved for different calculation modes:

- EQ calculation mode, describing thermodynamic equilibrium at a given temperature,
- DC calculation mode, describing steady-state conditions under an external applied voltage or current and/or illumination,
- AC calculation mode, describing small additional sinusoidal modulations of the external applied voltage/illumination, and
- TR calculation mode, describing transient changes of the system due to general time-dependent changes of the external applied voltage or current and/or illumination.

In this study, the EQ calculation model was used to model the band alignment of different structures. DC calculation mode was chosen for I-V and QE characterization of the SHJ solar cells. Consequently, in EQ and DC calculation modes, all-time derivatives vanish, resulting in a simplified system of differential equations. The system of differential equations is then solved for time independence. The Poisson equation and the continuity equations are solved in one dimension within the bulk of each semiconductor layer. The steady-state of heterostructure is modeled by the following equations [50]–[52]:

$$\frac{\partial D}{\partial x} = +q(p - n + \rho + N_D - N_A) \quad \text{(Eq.2.4)}$$

$$\frac{\partial J_n}{dx} = -q(G - R_n) \quad \text{(Eq.2.5)}$$

$$\frac{\partial J_p}{\partial x} = +q(G - R_p) \quad \text{(Eq.2.6)}$$

Here, D is the displacement field; p and n are the hole and electron densities, respectively; ρ is the net charge of all traps located in the band gap; $N_{A/D}$ is the acceptor and donor concentration, in that order. J_n and J_p are the electron and hole current densities, G is the optical generation rate, R_n and R_p are the electron and hole recombination rates. The recombination is modeled by Auger, direct band to band, and Shockley-Read-Hall (SRH) recombination mechanisms using Boltzmann statistics for the calculation of electron as well as hole concentration.

2.1.3 Recombination Models

Recombination from the conduction band into the valence band may mainly occur in three ways: radiative band-to-band recombination, Auger recombination, and Shockley-Read-Hall recombination. Radiative recombination rate constant has to be specified to equate the radiative band to band recombination rates [52].

$$R_{n,p}^{BB}(x,t) = B\{n(x,t)p(x,t)\}\,, \quad \text{(Eq.2.7)}$$

where B is the integrated coefficient. In this study, the radiative recombination rate was defined and kept constant through all simulations. Auger recombination can be expressed as:

$$R_{n,p}^{A}(x,t) = [r_n^A n(x,t) + r_p^A p(x,t)]\{n(x,t)p(x,t) - N_C N_V e^{-E_g/kT}\}, \quad \text{(Eq.2.8)}$$

where r_n^A and r_p^A are the Auger coefficient for electrons and holes, respectively. However, while modeling SHJ solar cells, Auger recombination is accepted as zero. The SRH, also known as trap-assisted recombination, consists of two recombination processes; this theory was reported first by Shockley, Read, and Hall [53], [54]. The electrons in the conduction bands recombine through localized energy states within the forbidden band energy. Such localized energy states are called traps, which can be formed by defects in the crystal lattice. The types (donor or acceptor like), the capture cross-sections, and the distribution of the traps within the band gap are the parameters to be known. The energy levels of traps are localized/distributed in different forms as follows;

1. Located at a single energy level (point-like),
2. Constant distribution in the specific region of the band gap,
3. From valance or conductance band edge into band gap with exponential decay,
4. Gaussian distribution within the band gap.

This study reviews the SRH recombination to understand the effect of Si wafer bulk quality on SHJ solar cell performance and the relationship between interface defects and passivation quality [52].

2.2 Input Parameters

The input parameters used for the simulation of SHJ solar cells are listed in Table 2.1.

Table 2. 1. Simulation input parameters.

Parameters	*(p) a-Si:H*	*(i) a-Si:H*	*c-Si*	*(n) a-Si:H*
Dielectric constant	11.9	11.9	11.9	11.9
Electron affinity (eV)	3.9	3.9	4.05	3.9
E_g(eV)	1.5 to 2.3	1.74	1.12	1.74
N_c(cm^{-3})	1x10^{20}	1x10^{20}	2.8x10^{19}	1x10^{20}
N_v(cm^{-3})	1x10^{20}	1x10^{20}	1.04x10^{19}	1x10^{20}
μ_n (cm^2/Vs)	20	20	1400	20

μ_p (cm^2/Vs)	5	5	400	5
N_a (cm^{-3})	10^{15} to 10^{19}	0	0	0
N_d (cm^{-3})	0	0	$5.0\text{x}10^{15}$	10^{15} to 10^{19}
ρ (gcm^{-3})	2.328	2.328	2.328	2.328

The input parameters for SHJ solar cells are determined from the relevant simulation literature [55]–[57]. The doping density values of (p) a-Si:H and (n) a-Si:H varied between 10^{15} to 10^{19} cm^{-3} to interpret their impact on SHJ solar cell parameters. One of the main problems on SHJ solar cell structure is the parasitic absorption that occurs on the front side layer because of the relatively low band gap value of (p) a-Si:H. For that reason, the band gap of the emitter layer was changed between 1.5 to 2.3 eV to understand the relationship between solar cell parameters and the emitter band gap layer. The band gap value of the emitter could be increased by the integration of (p) aSiC$_X$:H. The impact of defects is analyzed both for the a-Si:H/c-Si interface and the bulk c-Si. The density of state values for a-Si:H and their distributions are given in Appendix A.

2.3 Results and Discussions

2.3.1 Simulation of Various Doping Concentrations

Some limitations given below are taken into account during the modeling of various doping concentrations both for p and n-type a-Si:H layers;

- Reflectance losses are included (ITO layer n and k files were used from the library of Afors-Het).
- The bulk lifetime value is assumed to be infinity.
- For the ohmic metal contacts, no series resistance contribution from TCO and metal is considered.

- The thicknesses of (n) a-Si:H, (i) a-Si:H, and (p) a-Si:H layers are fixed to values of 12nm, 7nm, 10nm, respectively.
- There are no defects on the interface, bulk, and a-Si:H layers.

Figure 2.1 shows the SHJ solar cell simulation results for different doping densities of (p) a-Si:H. There is a strong correlation between N_a and solar cell parameters, especially FF and η. For values below N_a= 5.0x10^{17} cm^{-3}, efficiency and FF values are drastically low. However, for values above N_a=5.0x10^{17} cm^{-3}, it is found that J_{SC} values started to decrease; and increasing N_a value also led to a decrease in V_{OC} values. The optimum N_a value was obtained as 5.0x10^{18} cm^{-3} for the maximum efficiency.

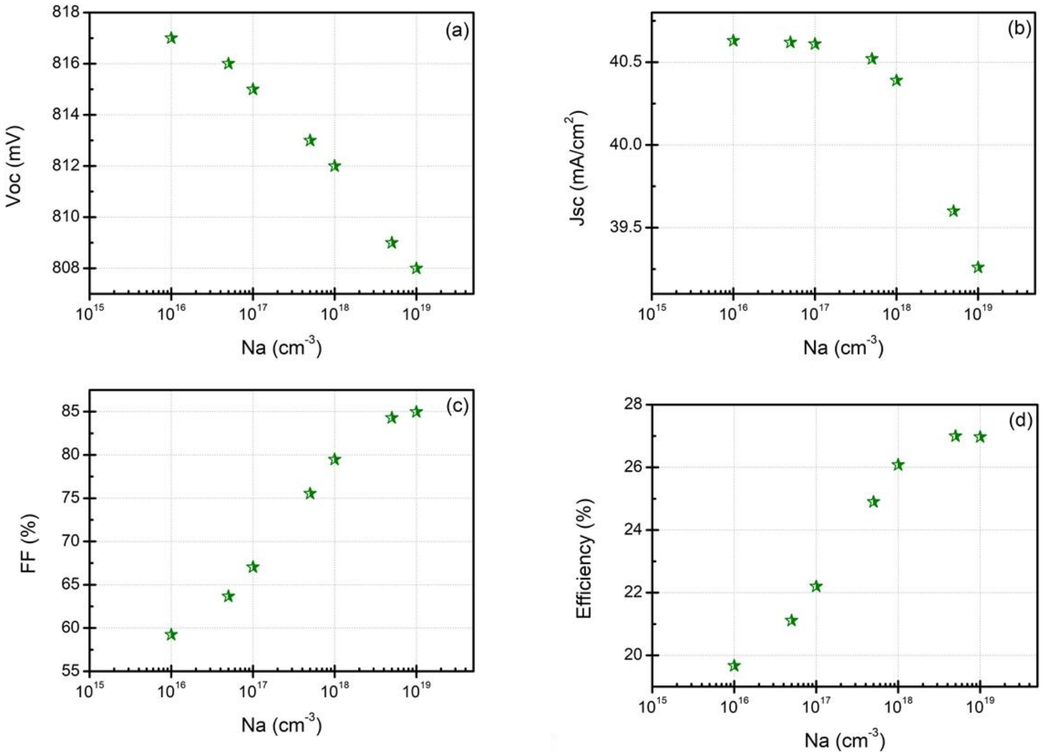

Figure 2. 1. SHJ solar cell simulation results of (a) V_{OC}, (b) J_{SC}, (c) FF, and (d) η for various N_a values.

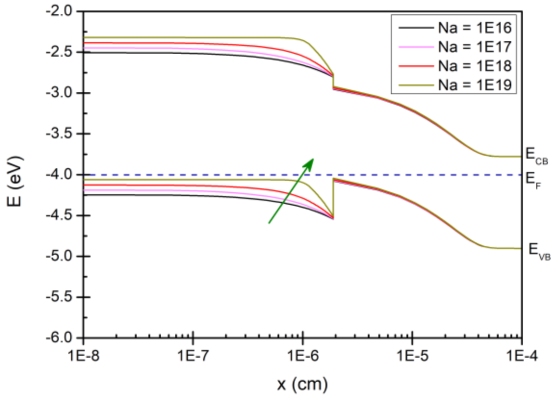

Figure 2. 2. Energy band diagram of (p) a-Si:H/(i) a-Si:H/c-Si structure for various N_a values.

The simulated band alignments of (p) a-Si:H/(i) a-Si:H/c-Si structure calculated by the AforsHet simulation program for different boron doping concentrations are given in Figure 2.2. The height of the barrier in the hole flow direction increases with increasing N_a value, from 46.13 meV (for N_a=1x10^{16} cm^{-3}) to 46.79 meV (for N_a=1x10^{19} cm^{-3}). However, the width of the barrier decreases with the increase in N_a, which confirms the variation of FF values with N_a for SHJ solar cells.

The impact of donor concentration, N_d, on the SHJ solar cell parameters was analyzed by illuminating the rear side of the cell. These results can be seen in Figure 2.3. Increasing the doping concentration of the (n) aSi:H layer led to a remarkable increase in J_{SC} value and a slight increase in the V_{OC} value of the solar cells. The FF values were almost the same for all doping concentrations. The highest J_{SC} and η values were obtained for the doping density of 5.0x10^{17} cm^{-3}. In Figure 2.4, the simulated band alignment of (n) a-Si:H/(i) a-Si:H/c-Si structure for various N_d values can be found. The barrier height for the flow of electrons is negligible, and it was determined as approximately 15 meV.

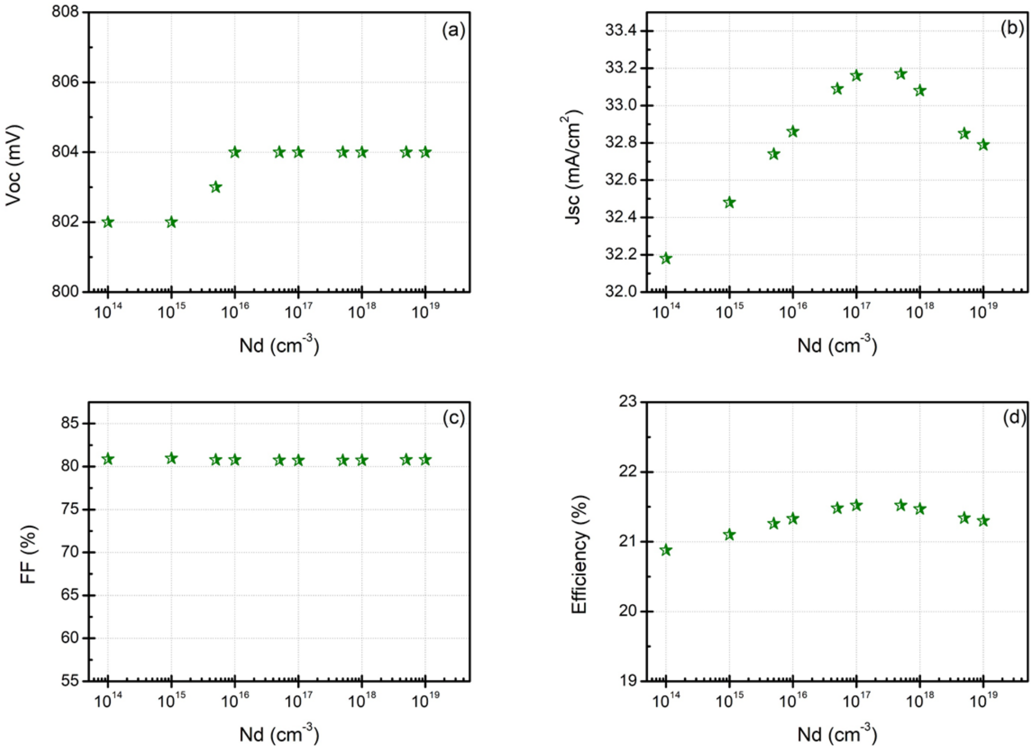

Figure 2. 3. SHJ solar cell simulation results of (a) V_{OC}, (b) J_{SC}, (c) FF and (d) η for various N_d values.

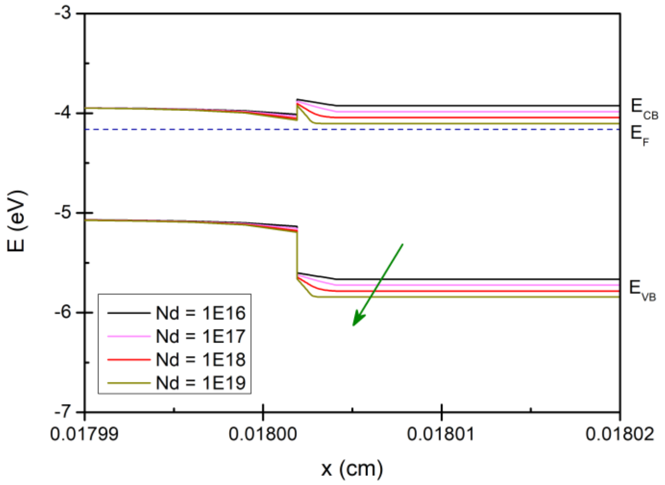

Figure 2. 4. Energy band diagram of (n) a-Si:H/(i) a-Si:H/c-Si structure for various N_d values.

For the maximum efficiency, the optimum values for N_d and N_a are obtained as 5.0×10^{17} and 5.0×10^{18} cm^{-3}, respectively. These values were taken as fixed for the subsequent simulation studies.

2.3.2 Simulation of Wide Band Gap Emitter

The parasitic absorption coming from (p) a-Si:H layer is one of the loss mechanisms for SHJ solar cells. It is possible to widen the emitter's band gap by incorporating carbon atoms into the structure resulting in (p) a-SiC_x:H layers. Up until now band gap of the (p) a-Si:H layer was taken as 1.74 eV. However, in real cases, band gap value of (p) a-Si:H layers can be as low as 1.65 eV. Moreover, practically the band gap of the (p) a-SiC_x:H layer can practically reach a value of 2.3 eV. Figure 2.5 shows results for SHJ solar cell parameters with different emitter band gap values. As seen in the figure, V_{OC} values slightly increased as the emitter band gap widened. However, J_{SC}, FF and η values increased up to the band gap value of 2.0 eV; after that point, a sharp decrease was observed for FF and η values. The findings show that, by increasing the band gap of the emitter, it is possible to enhance SHJ solar cell efficiency by nearly 1% compared band gap value of 1.74 eV due to the improvement of parasitic absorption losses. The restricting solar cell parameter is FF for band gap values higher than 2.0 eV, explained by the high barrier existing in the hole flow direction.

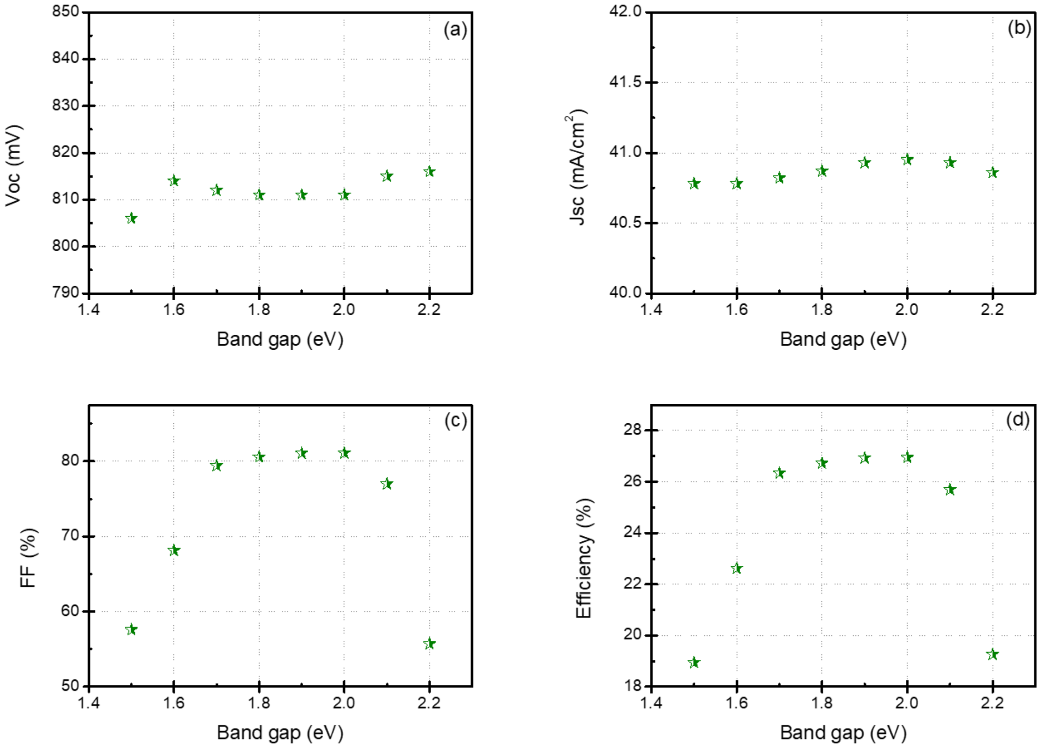

Figure 2. 5. (a) V_{OC}, (b) J_{SC}, (c) FF, and (d) η results of SHJ solar cells for different emitter band gap values.

For the study of (p) a-SiC_x:H as the emitter layer of SHJ solar cells, two different band gap values (1.9 and 2.0 eV) were selected since the highest efficiency values obtained by the simulation study.

2.3.3 Effect of Bulk Quality on SHJ Solar Cells

The bulk quality of c-Si wafers was identified by adding a single point defect into the mid-gap energy for various densities of states (DOS). The simulation program calculated representative lifetime values for both electrons and holes for each DOS in the mid-gap energy. Defect density was formed in mid-gap with the various DOS, and the simulation software directly calculated lifetime for electrons and holes, separately. The impact of bulk quality on V_{OC} and η are given in Figure 2.6 concerning DOS and bulk lifetime.

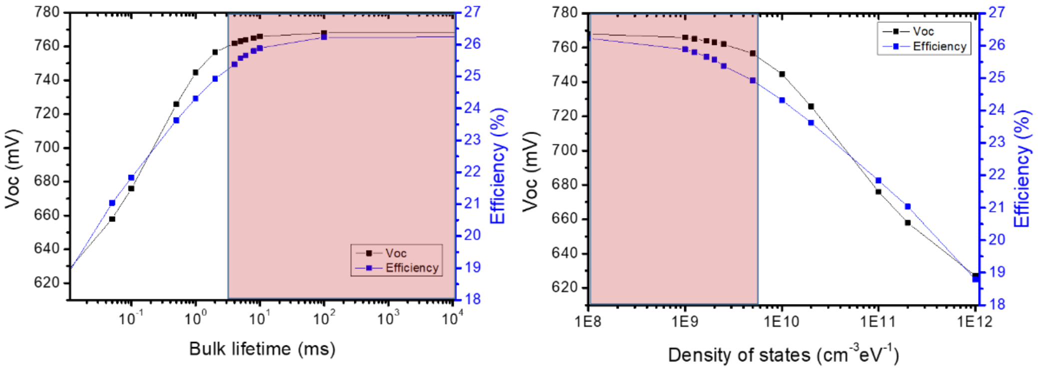

Figure 2. 6. The relationship between V_{OC} and efficiency for the bulk lifetime and DOS.

The bulk lifetime of c-Si, representing the bulk quality of the wafer, is one of the critical factors for the V_{OC} value of the solar cell. It is evident that any bulk lifetime V_{OC} value below 1ms is too low, resulting in relatively low efficiency values. Higher bulk lifetime means higher V_{OC} and efficiency. It was observed that a 2.5ms lifetime value for a c-Si wafer is crucial for high-efficiency SHJ solar cells.

2.3.4 Impact of Interface Trap Density on SHJ Solar Cell Parameters

The DOS was defined for all a-Si:H layers and the interface between c-Si and a-Si:H layer (See Figure A.1, A.2 and Table A.1). The DOS was constant for all a-Si:H layers during simulations. However, interface trap density (D_{it}) for c-Si and (i) a-Si:H interface was changed between 1.0x10^9 to 1.0x10^{11} cm^{-2}ev^{-1}. In high-quality a-Si:H passivation, the lowest D_{it} should be around 10^9 cm^{-2}eV^{-1} as discussed by other researchers [58], and passivation quality on the c-Si surface is directly related to D_{it}. Current-Voltage and External Quantum Efficiency (EQE) simulation results for different D_{it} values are shown in Figure 2.7 and Table 2.1. Results have shown that V_{OC} value strongly correlated with the quality of the interface. Lower interface defects led to higher surface passivation quality. There was a slight decrease in the J_{sc} and FF values when D_{it} was increased. The EQE results verify that there were very small decreases for J_{SC} values at almost all wavelengths for the higher amount of interface trap densities. There are possible ways to decrease surface interface densities, including the preliminary cleaning step. Additionally, deposition parameters also have an impact on interface quality, especially the deposition power density. This matter will be thoroughly covered in the passivation chapter below.

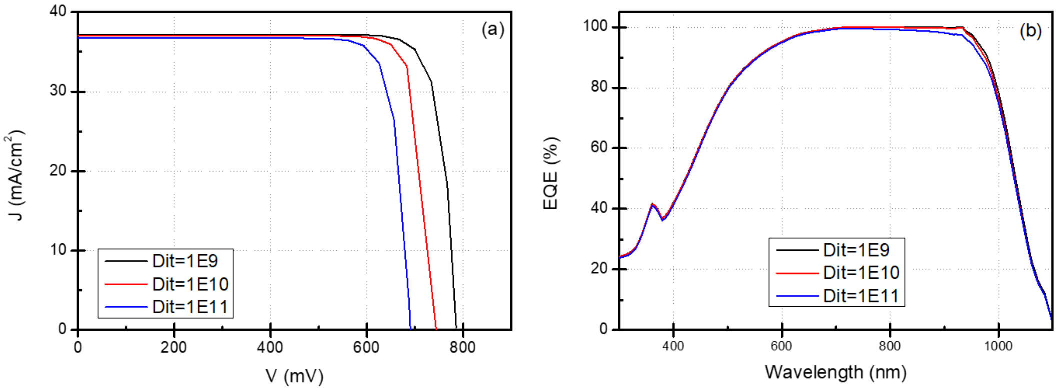

Figure 2. 7. (a) J-V and (b) EQE simulation results for different D_{it} values.

Table 2. 2. SHJ solar cell parameters for various D_{it} values.

D_{it} (cm^{-2}eV^{-1})	V_{OC} (mV)	J_{SC} (mA/cm^2)	FF (%)	η (%)
1.0x10^9	785.2	37.15	84.70	24.71
1.0x10^{10}	743.7	37.00	84.66	23.30
1.0x10^{11}	690.2	36.70	83.77	21.20

2.3.5 Effect of the Thickness of a-Si:H Layers

The effect of (p), (n), and (i) a-Si:H thicknesses were simulated using various combinations. While the thickness of (p) a-Si:H was kept constant at 10 nm, the thicknesses of (i) a-Si:H and (n) a-Si:H were changed between 3 to 9 nm and 10 to 26 nm, respectively; and additionally, the SHJ solar cell was illuminated from the rear during the simulations using various thickness values for (n) a-Si:H layer. While the thickness of (n) a-Si:H was kept constant at 10 nm, the thicknesses of (i) a-Si:H and (p) a-Si:H were changed between 3 to 9 nm and 10 to 20 nm, respectively. The impact of DOS and D_{it} on SHJ solar cell parameters was not included in this study.

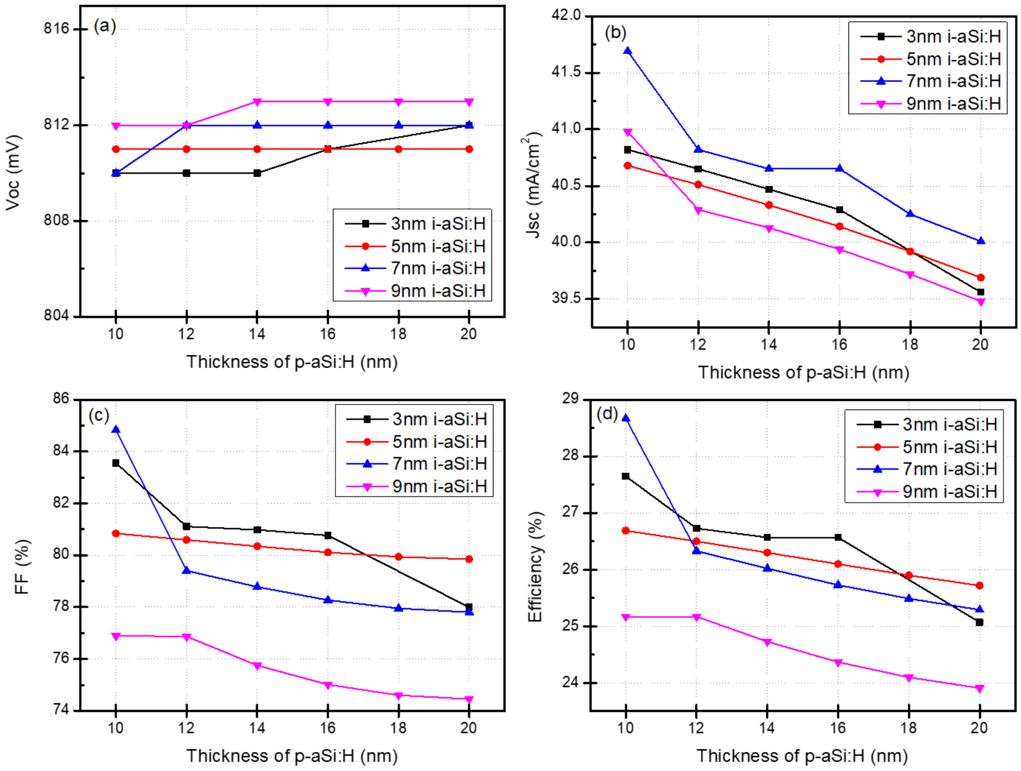

Figure 2. 8. The impact of (p) a-Si:H and (i) a-Si:H thickness on (a) V_{OC}, (b) J_{SC}, (c) FF and (d) η values.

Figure 2.8 represents the SHJ solar cell simulation results for different thickness values of (p) a-Si:H and (i) a-Si:H layers. The V_{OC} increased slightly for both thicker (i) and (p) layers; however, when the thickness of (p) a-Si:H was increased, η, FF, and J_{SC} values decreased significantly. Here, we can conclude that the thickness of both (i) a-Si:H and (p) a-Si:H should be reduced as much as possible to decrease parasitic absorption of a-Si:H layers and the series resistance caused by a-Si:H layers having relatively high resistivity.

The simulation results in Figure 2.9 are for different thicknesses of (n) a-Si:H and (i) a-Si:H layers, with fixed (p) a-Si:H thickness and illumination from the rear side.

The V_{OC} and FF values were almost the same for all thicknesses; however, when the thickness of (n) a-Si:H increased, η, and J_{SC} values decreased slightly. Here, a conclusion similar to the previous study is valid for various thicknesses a-Si:H layers on the rear side of the solar cell.

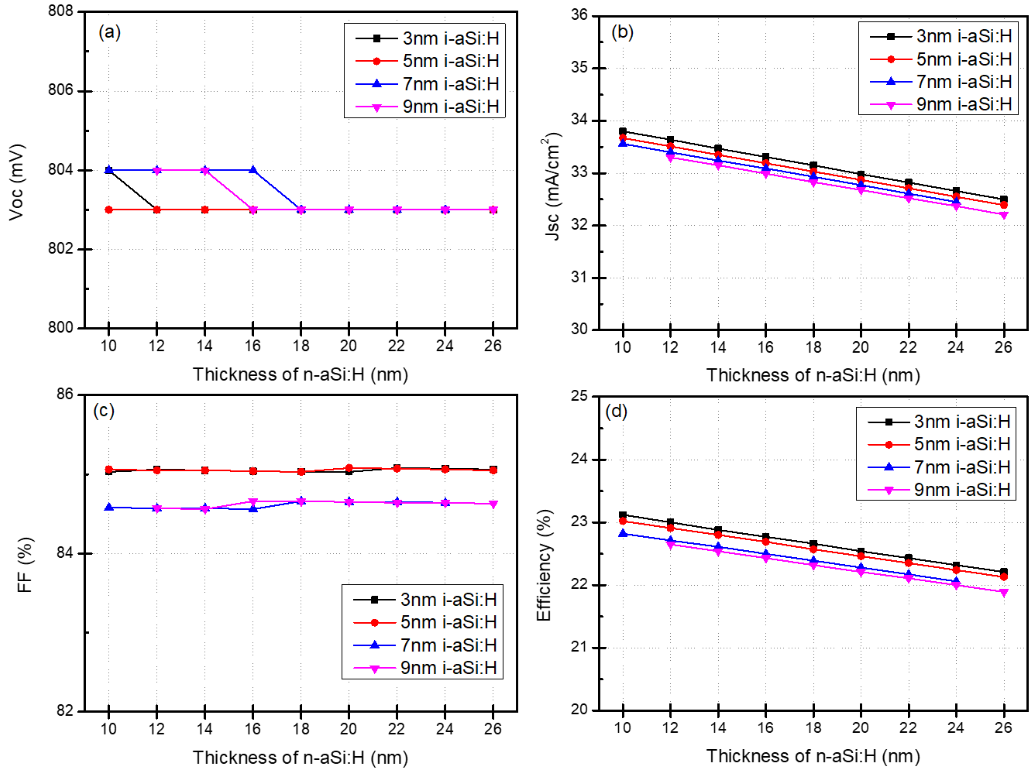

Figure 2. 9. The effect of (n) a-Si:H and (i) a-Si:H thickness on (a) V_{OC}, (b) J_{SC}, (c) FF and (d) η values.

2.4 Conclusions

SHJ solar cell structure simulations were run using the AforsHet simulation program with different configurations and parameters to analyze and identify the relationship between solar cell parameters and thickness, emitter band gap, wafer quality, and interface properties. It was observed that for the fabrication of efficient SHJ solar cells, the doping density of (p) a-Si:H and (n) a-Si:H should be $5.0x10^{18}$ and $5.0x10^{17}$

cm^{-3}, respectively. An increase in the barrier height and width on the hole flow direction between (p) a-Si:H and c-Si interface plays a detrimental role in device performance. Moreover, increasing the band gap of (p) a-Si:H, which is possible by the incorporation of C into the structure, enhances the device performance up to a certain point. The optimum band gap of the emitter layer was identified as between 1.9 to 2.0 eV for maximum efficiency. Above band gap of 2.0 eV, the FF values decreased significantly due to a rise in barrier height on hole flow direction.

Furthermore, it was noted that the bulk quality of the c-Si wafer is essential to get high passivation quality. The simulation results showed that the bulk lifetime should be at least 2.5 ms or higher. Besides bulk quality, the interface defect density plays a vital role in the excellent passivation of the a-Si:H layer. The relation between D_{it} and passivation was also clarified after finding that D_{it} values should be lower than $1x10^{10}$ $cm^{-2}eV^{-1}$ to achieve proper chemical passivation. Finally, the impact of a-Si:H thicknesses on the device performance was interpreted. The results showed that the thinner the a-Si:H (for all p, n, and i layers), the better the SHJ solar cell performance was due to reduced series resistance losses.

CHAPTER 3

LIGHT MANAGEMENT TECHNIQUES FOR HIGH EFFICIENCY SILICON SOLAR CELLS

One of the obvious requirements for high efficiency solar cells is to maximize the absorption of the light falling on them. This is usually achieved by texturing the surface in such a way that the light falling on the surface interacts with the surface more than once, resulting in more absorption. In this chapter, we present a new and alternative technique to the existing texturing technology producing an upward pyramid structure on the surface.

3.1 Introduction

Si wafers require surface texturing to reduce reflectance losses arising from the surface. The most commonly used method both in laboratories and factories is the formation of random pyramids on the (100)-oriented c-Si surface with a reflectance of about 10% by utilizing anisotropic wet chemical alkaline-based etching [59], [60]. In the case of multi-crystalline (mc) Si wafers, surface texturing is produced by using acid-based solutions [61]. The standard commercialized alkaline-based texturing method for c-Si solar cells has total reflectance losses around 2 mA/cm^2 in the short-circuit current density (J_{SC}) [62]. Recently, there have been promising studies on black silicon (b-Si), in which surface reflectance values went below 2% by using reactive ion etching (RIE) [63], [64], laser ablation [65], chemical etching [66], and metal-assisted chemical etching (MACE) techniques [67]. However, b-Si surfaces have some challenges of their own; due to enlargement in the Si surface area, high surface recombination rates occur, resulting in relatively low passivation qualities. [68]–[70].

Silver (Ag) [71] and gold (Au) [72] are the most widely used metals in the MACE technique. These noble metals are generally grown on the Si surface via various deposition methods like sputtering [73], thermal evaporation [74], and other approaches [75]. For Ag-assisted-etching, the single-step etching of Si is possible only on polished surfaces, which requires a more complex and expensive fabrication process flow on as-cut wafers [75]. The low reflectivity and surface recombination rates can be achieved with either (regular or complex) photolithography steps or random inverted pyramid (IP) [76], called Cu-assisted chemical etching (Cu-ACE) [77]. Random IP structures produced with Cu-ACE without any preliminary chemical steps proved to have efficient light management properties with a surface reflectivity lower than 4% [78]–[80]. With this low reflectivity value, Cu-ACE is offering an attractive alternative to the regular IP made by a complex and expensive lithography process. Among any other MACE technique, the etching mechanism of Cu-ACE is quite different, where nucleation and dissolution work simultaneously [80]. It is a single step without any masking, resulting in an anisotropic etching. The anisotropic behavior of the solution strongly depends on the doping concentration of the Si wafer, molarities, and solution temperature [81].

This chapter covers the etching mechanism and its dependency on molarities. Five different surface morphologies: polished, micro-porous, elliptical, IP, and tetragonal-star-shaped IPs were obtained by a deep understanding and controlling of the etching mechanism. A novel lithography-free, single-step metal-assisted chemical etching process with moderate solution temperature yielding micro-sized inverted pyramid structures with tetragonal-star-shaped with a shallow reflectivity value of around 2% was achieved on the (100)-oriented c-Si. Then, changing the oxidizing agent to nitric acid, we increased the control ability of the etching, resulting in a random IP surface. Furthermore, we developed a solution that enables texturing at room temperature with having reflectivity lower than 10%.

The c-Si surface with the novel star-shaped IPs structure was introduced to aluminum back surface field (Al-BSF) Si solar cell fabrication. We have achieved more than a 3% improvement in the J_{SC} value.

3.2 Experimental

The standard alkaline-based surface texturing is done by the Rena BatchTex tool using 2.6% potassium hydroxide (KOH), including the MonoTex F additive, which is the standard texturing method used in research studies carried out in ODTÜ-GÜNAM. This procedure is applicable for both n- and p-type (100)-oriented Si wafers. For the Cu-ACE part of the study, p-type (1-3 Ωcm), (100)-oriented 200 μm thick, p-type as-cut c-Si wafers were used. The wafers were preliminarily cleaned only by hydrofluoric acid (HF), hydrochloric acid (HCl), and deionized (DI) water solution prepared with a 1:1:20 volumetric ratio to remove the naturally grown oxide layer, and they were then rinsed in DI water. The novel etching solution was adjusted to be between 50°C and 55°C under various molarities of copper nitrate ($Cu(NO_{3})_{2}$), HF, hydrogen peroxide (H_2O_2) in DI water. Different etching times were analyzed for each solution to understand the etching mechanism of IPs. In order to understand the variation in dissociations of each chemical separately, we used a pH meter to clarify the impact of temperature on the dissociation mechanism of HF and H_2O_2. Mass loss calculation was applied to calculate the etch rate of etchant. Different etching conditions resulted in various surface topologies and morphologies. After the formation of IPs, the wafers were cleaned from Cu nanoparticles using a concentrated nitric acid solution (HNO_3:H_2O, 1:5) in an ultrasonic bath for 15 min. EDX and SIMS analyses were performed to observe the effect of nitric acid cleaning on Cu NP removal. Surface morphologies of prepared samples were specified by an SEM (ZEISS Evo HD 15) and reflectance measurements. From the reflectance measurements, average weighted reflectance values were calculated with the following:

$$R_{Weighted} = \frac{\int_{\lambda_1}^{\lambda_2} R(\lambda)\phi_{ph}(\lambda)d\lambda}{\int_{\lambda_1}^{\lambda_2} \phi_{ph}(\lambda)d\lambda} \quad , \qquad \text{(Eq.3.1)}$$

where λ is the wavelength, R(λ) is the reflectance value at a given wavelength and ϕ_{ph} is the photon flux AM 1.5G at that wavelength. The IPs distribution was analyzed using Fast Fourier Transform (FFT) with ImageJ software. The regular fabrication cycle optimized for Al-BSF solar cells was applied. Al-BSF solar cells were characterized by current-voltage (I-V) measurements with a solar simulator from Newport.

In the second part, the oxidizing agent of the solution was changed with nitric acid (HNO_3). Similar characterization techniques were used for $Cu(NO_3)_2$:HF:HNO_3:H_2O solution prepared at room temperature and 50°C, under various etching times and molarities.

3.3 Etching Mechanism of Cu-ACE Method

The etching mechanism of Cu-ACE has a similar theory to other MACE techniques except for the anisotropic behavior. Cu NPs are continuously formed on the c-Si surface and dissolved during the immersion of Si into the etchant. The half-cell reactions of the solution can be described as the following reactions:

Cathode reactions:

$$Cu^{2+} + 2e^- \rightarrow Cu^0(s) \qquad E_0 = +0.34\, V per\, SHE \qquad \text{(Eq.3.2)}$$

$$H_2O_2 + 2H^+ \rightarrow 2H_2O + 2h^+ \qquad E_0 = +1.77\, V per\, SHE \qquad \text{(Eq.3.3)}$$

Anode reaction:

$$Si + 6HF + nh^+ \rightarrow H_2SiF_6 + nH^+ + \frac{4-n}{2}H_2 \qquad E_0 = -1.20\, V per\, SHE \quad \text{(Eq.3.4)}$$

where SHE is the standard hydrogen electrode, n is the number of holes per dissolved Si atom. Cu^{+2} and H_2O_2 are reduced, and Cu^{+2} attracts electrons from Si [71], [75]. Once the nucleation of Cu NPs starts on the surface of Si, it continues to grow by attracting electrons from Cu instead of Si due to the electronegativity differences. The oxidation of Si atoms takes place underneath Cu NPs in the presence of H_2O_2; then, HF simultaneously dissolves the oxidized Si atoms. The charge transfer between the electrochemical reactions and Si is one of the deterministic parameters regarding the etching, formation, and growth of Cu NPs. The differences in redox potentials and Fermi level alignment between Si and Cu influence the charge transfer in the electrochemical solution. The Fermi level alignment of Si was explained in detail by Yan Wang et al. [78]. The Fermi energy level of p-type Si is lower than the work function of Cu, which leads to a Schottky barrier in the hole injection direction. The band alignment between Si and Cu was shown in Figure 3.1 before and at the equilibrium.

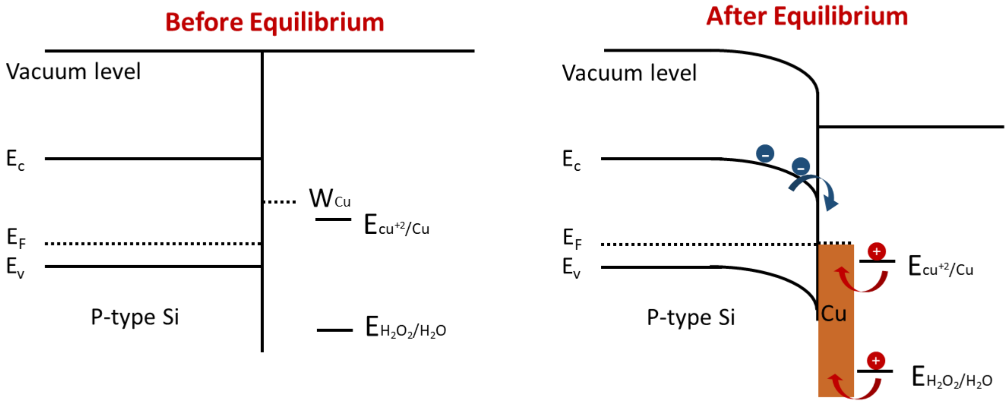

Figure 3. 1. The band alignment between Cu and Si before and at equilibrium.

The redox potential differences of electrochemical solution at the equilibrium can be calculated using Nernst equations [82], [83]; the cathode reactions are:

$$E_{Cu}(V\ per\ SHE) = 0.34 + \frac{RT}{2F}\ln[Cu^{2+}] \qquad \text{(Eq.3.5)}$$

$$E_{H_2O_2}(V\ per\ SHE) = 1.77 + \frac{RT}{F}ln[H^{+}] \qquad \text{(Eq3.6)}$$

$$E_{Si}(V\ per\ SHE) = -1.20 + \frac{RT}{F} ln[H^{+}] \qquad \text{(Eq.3.7)}$$

where E is the equilibrium potential, R is the ideal gas constant, F is the Faraday constant, T is the temperature of the electrochemical solution, and $[Cu^{2+}]$ and $[H^{+}]$ are the molarities of Cu^{2+} and H^{+} ions in the solution in equilibrium, respectively.

3.4 Results and Discussions

The standard alkaline-based random up-right pyramid texturing of Si wafers is a well-established methodology on Si solar cells resulting in approximately 10% reflectance without any anti-reflection coatings [84]. However, a significant amount of sunlight in the targeted spectrum is lost as a reflectance. First, the standard random pyramid texturing will be discussed below. Then, the fabrication of lithography-free IPs by the Cu-ACE technique with the help of self-assembled Cu NPs will be presented and discussed.

3.4.1 Alkaline-based Texturing

The surface morphology of standard texturing was investigated by SEM images, as given in Figure 3.2 (a). The SEM images showed some roughnesses and small pyramids. Between 400 to 1100 nm wavelength intervals, the weighted reflectance was 11.31% (see Figure 3.1 (b)).

The pyramid edge size distribution of standard texturing was calculated from SEM images using an image processing tool called ImageJ and given in Figure 3.3. The mean value was identified as 2.25 µm with a standard deviation of 1.31 µm. Moreover, maximum and minimum edge sizes were calculated as 0.29 and 8.16 µm, respectively.

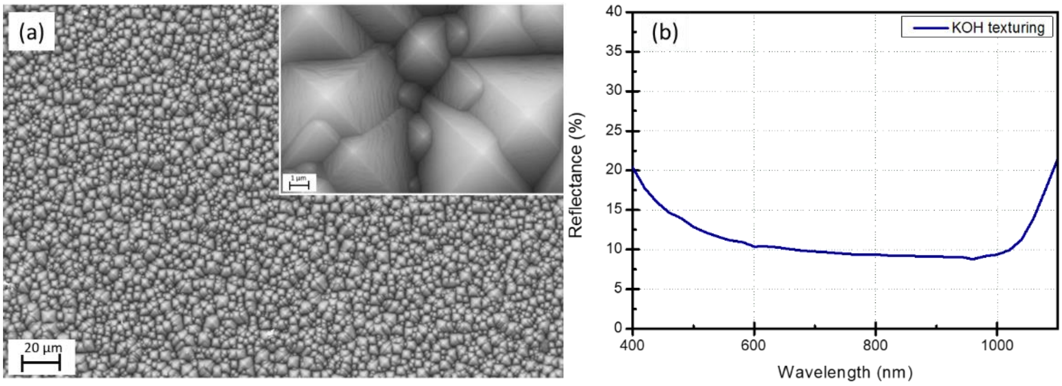

Figure 3. 2. (a) SEM images and (b) reflectance of standard KOH texturing.

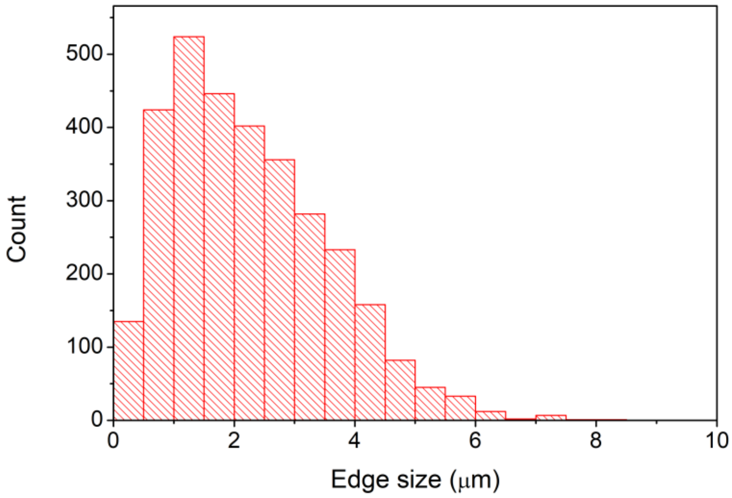

Figure 3. 3. Pyramid size distribution of standard texturing.

3.4.2 Copper-assisted Chemical Etching

3.4.2.1 Impact of $Cu(NO_3)_2$ Molarity on Surface Morphology

The molarity of $Cu(NO_3)_2$ varied between 6 to 8.5 mM under a constant temperature of 50°C, and fixed molarity values of 5.4 M and 0.7 M for HF and H_2O_2, respectively. The SEM images of resulting surface morphologies for various $Cu(NO_3)_2$ molarities are shown in Figure 3.4.

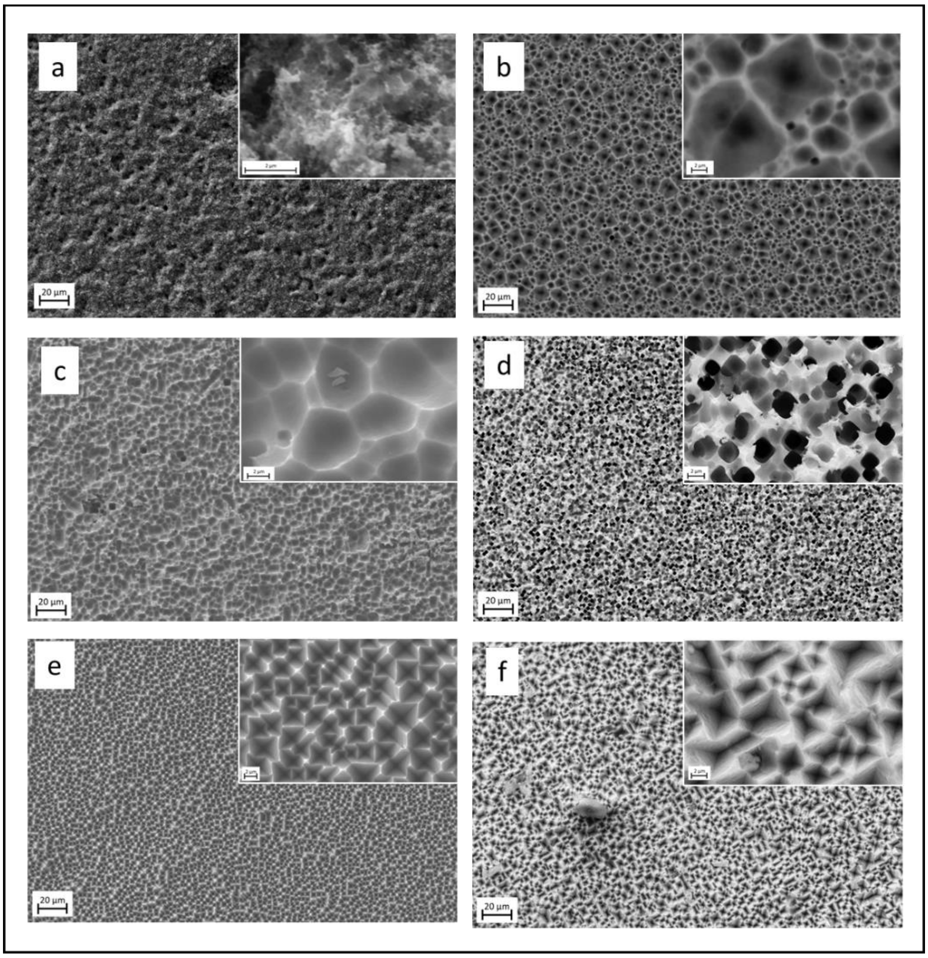

Figure 3. 4. SEM images of Si substrates after 15 min. etching with $Cu(NO_3)_2$ molarity values of (a) 6mM, (b) 6.5 mM, (c) 7.0 mM, (d) 7.5 mM, (e) 8.0 mM, (f) 8.5 mM.

To promote the anisotropic etching, a certain level of $Cu(NO_3)_2$ molarity is needed. Due to the lack of Cu atoms for molarity values below 6.5 mM $Cu(NO_3)_2$, Cu NPs cannot uniformly and densely nucleate through the Si surface, thus resulting in a rough surface without any specific structure shown in Figure 3.4 (a). The partially anisotropic etching started once the molarity increased to 6.5 mM $Cu(NO_3)_2$, in which elliptical and porous-like morphology occurred, as shown in Figure 3.4 (b). Another slight increment in molarity of $Cu(NO_3)_2$ led to a more uniform surface morphology with the micro-sized elliptical-shaped structure (see Figure 3.4 (c)). We observed a porous-like semi-square structure between the molarity values for which elliptical-shaped and IPs were formed, as shown in Figure 3.4 (d). For the molarity value of 8.0 mM, dissociation and nucleation mechanism reached dynamic equilibrium, resulting in well-defined IPs due to preferentially higher nucleation rate of Cu-NPs on the (100) planes with the electron capturing ability of Cu^{2+}. The average pyramid edge size was 2.8 µm (See Figure 3.5). However, when the molarity value of $Cu(NO_3)_2$ increased to 8.5 mM, which is called an "over-etching" regime, the average pyramid size decreased to less than 2.6 µm, and the etch rate of the solution increased from 1.4 µm/min to 2.0 µm/min. Furthermore, the IPs were formed in smaller sizes compared to the 8.0 mM etching. The comparison of pyramid edge size distributions can be found in Figure 3.5. Edge sizes were changed for the over-etching regime, for which the total number of small-sized IPs increased.

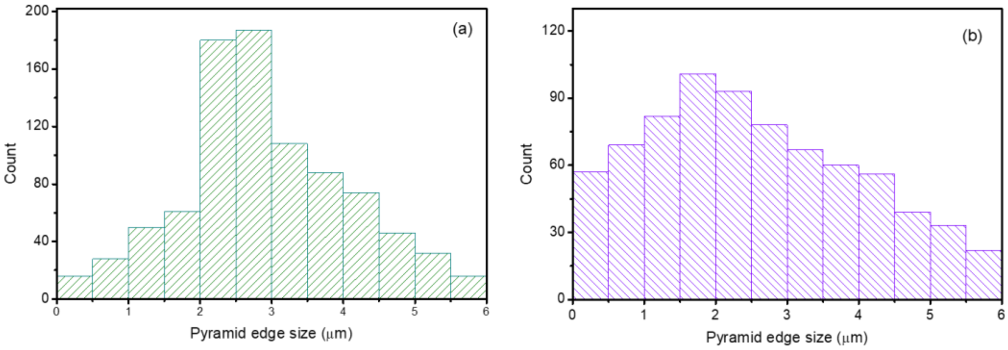

Figure 3. 5. Distribution of pyramid edge sizes for (a) well-defined IPs and (b) over-etching region.

The post etching reflectance spectra of Si for various $Cu(NO_3)_2$ molarity values can be seen in Fig. 3.6. The elliptical-shaped surface morphology resulted in the highest weighted reflectance. The average weighted reflectance ($R_{weighted}$) value was calculated for wavelength intervals between 400 to 1000 nm. $R_{weighted}$ values decreased from 10.75% (elliptical-shaped) to 3.74% (well-defined IPs), the lowest reflectance value in the literature [77] with the Cu-ACE technique. However, when we look at the over-etching regime, the $R_{weighted}$ value is increased slightly to 5.40% due to the shrink in the size and distribution of IPs.

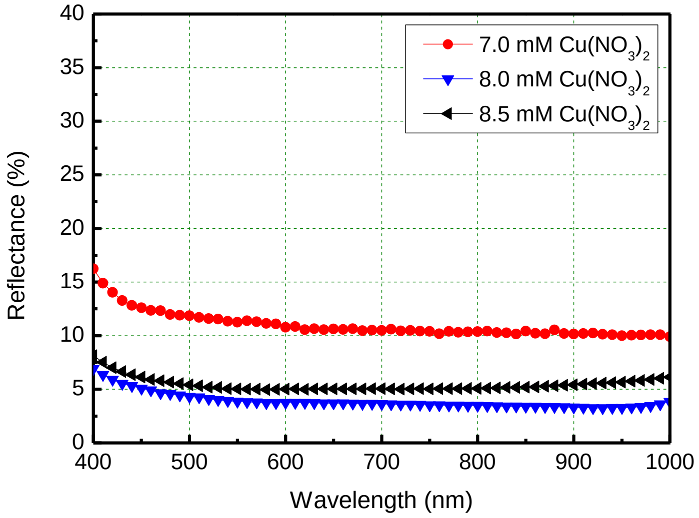

Figure 3. 6. The reflectance spectra of Si surface with IPs formed by various molarities of Cu(NO$_3$)$_2$.

3.4.2.2 Formation of Inverted Pyramids

The formation of IPs is analyzed for the optimum concentration of Cu(NO$_3$)$_2$ found in the previous study by time-dependent etching of the as-cut Si wafer. In the first minute of etching, the surface roughness resulting from saw damages could not be removed, as shown in Figure 3.7. However, after 2 minutes of etching, the anisotropic etching behavior of the solution becomes distinguishable by SEM investigation, resulting in less than 10% surface reflectivity for wavelengths longer than 600 nm (Figure 3.7 c and i). Surprisingly, the surface morphology of the etched Si was elliptical-shaped up to 5 minutes, and the IPs started to become defined after 5 minutes of etching, resulting in relatively lower reflectance values (Figure 3.7 d and i). The pyramidal structures had sharper after 10 minutes of etching, and well-defined surface morphology was achieved after 15 minutes, resulting in the record lowest reflectance value (Figure 3.7 e, f and Figure 3.8). However, after 15 minutes of etching, the size of the pyramids started to decrease, and surface reflectivity increased slightly for the IR region of the spectrum (Figure 3.7 g and Figure 3.8).

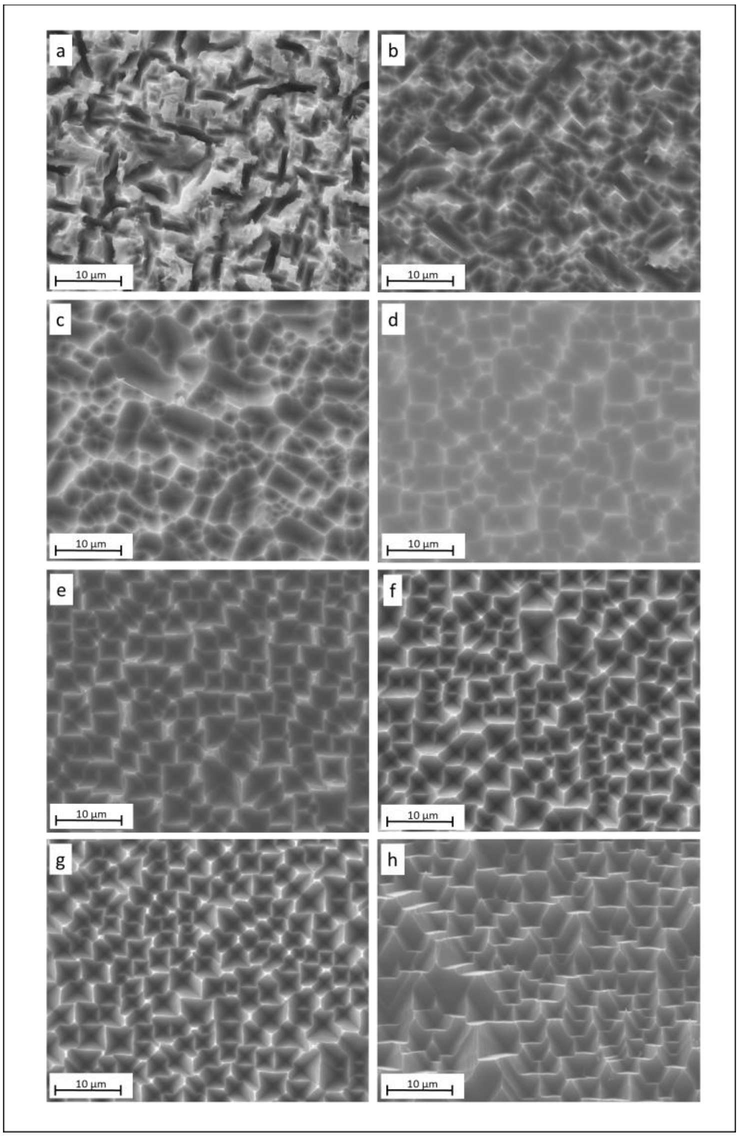

Figure 3. 7. SEM images of Si surface after (a) 30 s., (b) 1min., (c) 2min., (d) 5min., (e) 10min., (f) 15min., (g) 20min. and (h) 30° tilted SEM image of 15 minutes etched samples.

The average edge size of pyramids decreased from 2.87 µm to 2.68 µm as the etching duration increased from 15 to 20 minutes. The size distribution of pyramids is dispersed in a very narrow range for higher etching duration, as shown in Figure 3.8. At the optimum etching duration, which is 15 minutes, the walls and edges of pyramids were appropriately structured, as shown in Figure 3.7 (h). For longer etching durations, pyramid sizes were smaller, and there were fewer larger pyramids, as given in Figure 3.9.

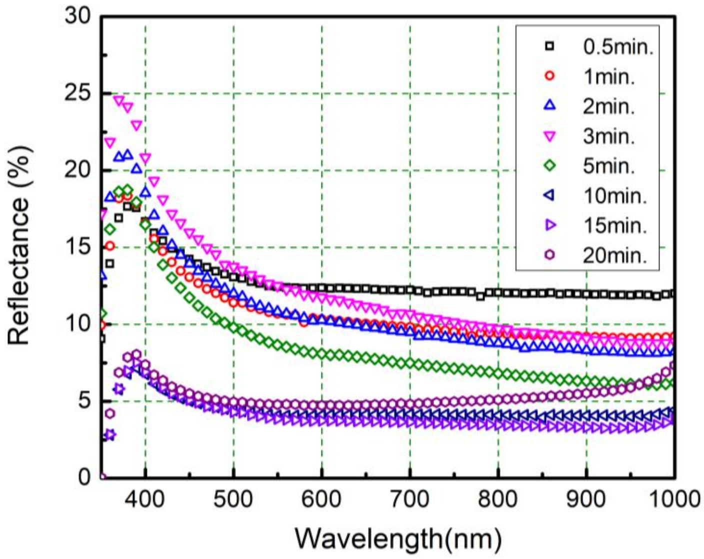

Figure 3. 8. The spectral reflectance for various etching durations.

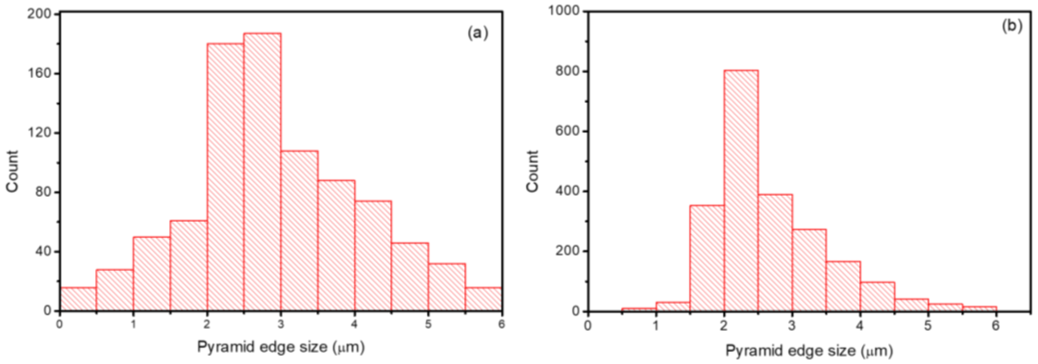

Figure 3. 9. Pyramid edge size distribution of (a) 15 and (b) 20 minutes of etching with optimum concentration.

3.4.2.3 Effect of H_2O_2 and HF Molarities on The Surface Morphology

The molarity of chemicals has a detrimental role on the final surface morphology. To analyze the effect of molarity of H_2O_2 and HF, the molarity of $Cu(NO_3)_2$ and solution temperature was fixed at 8mM, and 50°C, respectively. Firstly, the molarity of H_2O_2 was increased to 1 M while other concentrations were kept the same as optimum etching condition. The etching duration was varied as 8, 12, and 17 minutes to understand the time dependence of the etching mechanism. The rise in H_2O_2 molarity promoted oxidation reaction and decreased the nucleation of Cu NPs, resulting in a significantly low etch rate of 1.2 µm/minute. The weighted reflectance values increased up to 11.7% after 17 minutes of etching; however, the surface morphology was quite different from previous structures, and elongated holes were formed on the surface (see Figure 3.10 a and b). Even though the reflectance values were compatible with up-right random pyramids, the structured surface with elongated holes may not be suitable for solar cell applications due to the relatively rough and porous surface (See Fig 3.10 c). Secondly, the molarity of HF was raised to 6 M while the temperature and molarity of other chemicals were fixed. The nucleation of Cu NPs was promoted, and etch rate increased twice as much as the optimum etching condition, which resulted in Cu forming a continuous thin metal layer on the Si surface. The $R_{weighted}$ values increased up to 28.3% after 5 minutes of etching with the increased HF molarity, and the surface reflectivity was comparable with saw-damaged removed samples by KOH (see Figure 3.11). Depending on the concentration of HF, the solution behaved almost like an isotropic etchant, which resulted in increased surface roughness as observed by SEM images in Figure 3.10 (d).

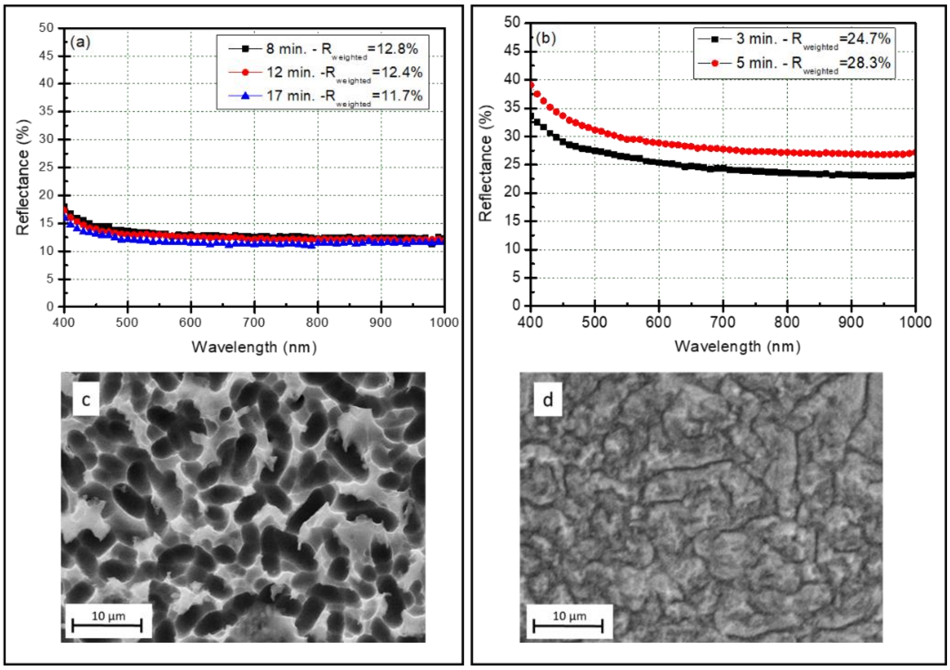

Figure 3. 10. (a) Surface reflectivity results of etching where the solution had 1 M of H_2O_2 but fixed concentrations of $Cu(NO_3)_2$, HF, and (b) 6 M of HF but fixed concentrations of $Cu(NO_3)_2$, H_2O_2 for various durations. SEM investigation after (c) 17 minutes of etching with increased concentration of H_2O_2 (1 M) and (d) 5 minutes of etching with increased concentration of HF (6 M).

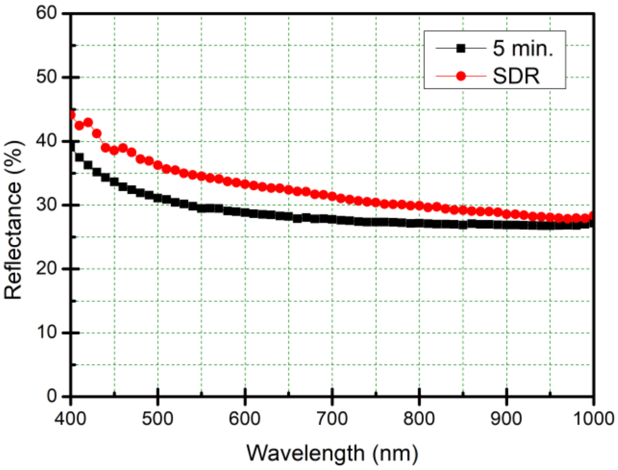

Figure 3. 11. Surface reflectivity comparison of SDR and 5 minutes of etched Si surface at 6 M HF.

3.4.2.4 Formation of Novel Tetragonal-star-shaped IPs

The most critical deciding parameter on surface morphology is the concentration of HF, which determines the direction of etching. However, dissociation of HF is also related to the solution temperature, which has an effect on the dissociation constant of HF and the solution's acidity [85]. Moreover, the temperature of the solution should be between 50°C to 55°C to form IPs [77]. Firstly, the variations in the pH of the solution were determined for various temperatures separately for H_2O_2 and HF. A significant acidity change was detected for HF when solution temperature increased from 50°C to 55°C, while the pH values for H_2O_2 were almost similar for both temperatures as given in Table 3.1. Then, the solution with optimum concentrations was prepared at 55°C, and p-type Si wafers were etched for 15 minutes in the solution. The IP-like structures formed with a deeper size (See Fig 3.12). The surface reflectivity was higher than 6%, and etch rate of the solution also increased to 3.8 μm/minute. Here, it was found that changes in the solution temperature also influenced the etching directionality and the etch rate resulting in different surface morphologies.

Table 3. 1. The pH variation of HF and H_2O_2 for different temperatures.

Chemical	Molarity (M)	pH @ 50°C	pH @ 55°C
H_2O_2	0.7	4.50	4.45
HF	5.4	1.65	1.25

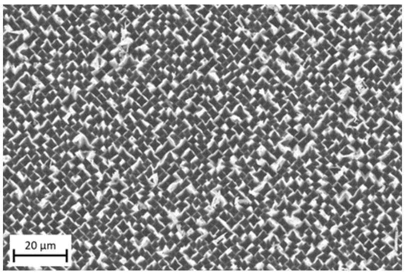

Figure 3. 12. The Si surface was etched for 15 minutes at 55°C with optimum concentrations.

Later, to investigate the impact of a gradual increase in the temperature for the formation of IPs, the prepared optimum concentration temperature was increased from 50°C to 55°C over 15 minutes during the etching of Si. The novel tetragonal-star-shaped IP structure was obtained with precise control and the gradual increase of temperature during etching. The promoted etching direction by increasing the temperature of the solution led the final structure to be formed as the tetragonal-star-shaped morphology with random distribution. In Figure 3.13, the tetragonal-star-shaped and standard IPs were studied using SEM images and compared with the FFT method to clarify the randomness and directional properties of the surfaces decorated with two various structures. It was confirmed that the formation of IPs in both structures is random within a specific range of size. However, distribution in the periodicity is quite different for the tetragonal-star-shaped and standard IP structure representing periodicity distribution on the tetragonal structured surface. The top SEM view of the single pyramid shows the variation on periodicity explicitly (see Fig 3.14). Figure 3.14 (a) includes the comparison of the spectral reflectance results of upright, inverted, and tetragonal-star-shaped inverted pyramids. The lowest surface reflectance values were achieved by the Cu-ACE method, where the corresponding $R_{weighted}$ was 2.65% with the help of the novel texturing approach resulting in tetragonal-star-shaped IPs on the Si surface. Moreover, both regular and star-shaped IP structures had superior optical properties compared to upright pyramids.

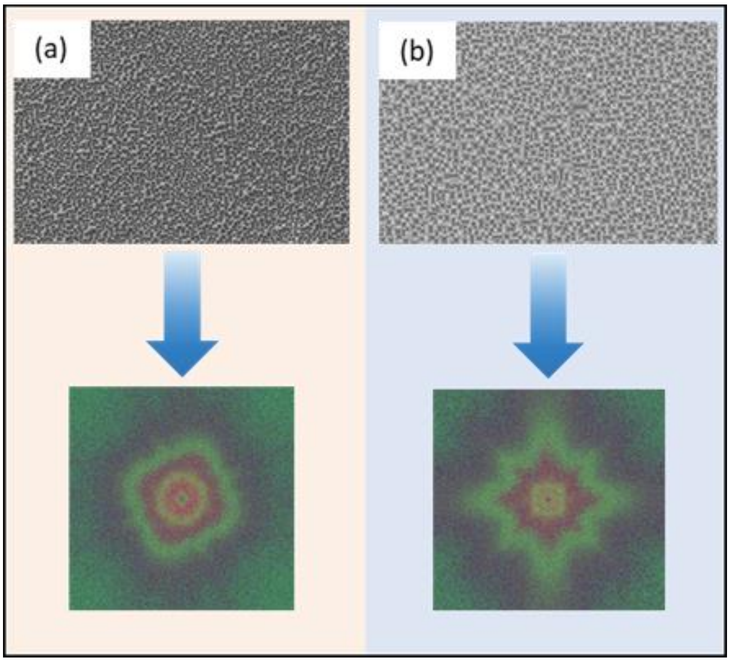

Figure 3. 13. Comparison of (a) standard and (b) tetragonal-star-shaped IPs by SEM observations and FFT analysis.

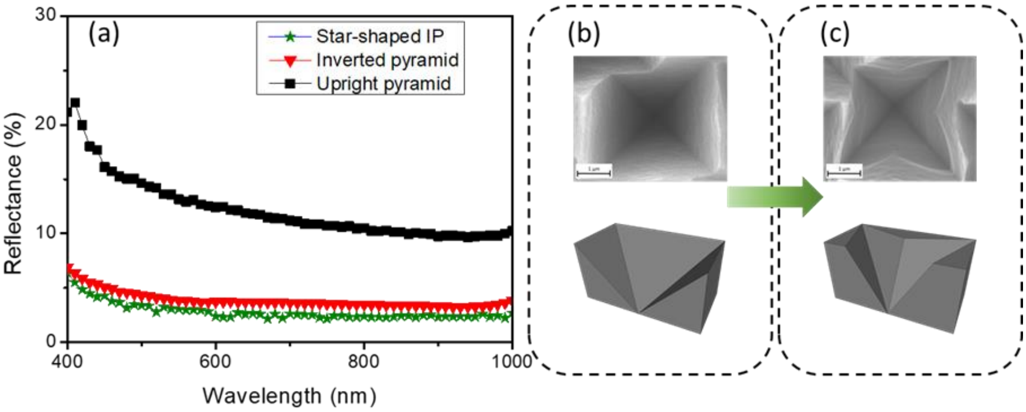

Figure 3. 14. (a) The comparison of spectral reflectance for random upright pyramid, IPs, and tetragonal-start-shaped IPs and (b) top SEM view and cross-sectional representative of standard and (c) tetragonal-star-shaped IPs.

3.4.2.5 Application of Tetragonal-star-shaped IPs to Al-BSF Solar Cell

Al-BSF Si solar cells were fabricated on the p-type Si wafers, both tetragonal-star-shaped IP structures, and standard upright pyramids as a reference. Figure 3.15 shows the solar cell parameters V_{OC}, J_{SC}, FF, and η, of IP structures normalized with respect to upright pyramid ones. The V_{OC} values for IP structures decreased relative to the structure with the upright pyramid, which could be improved by a conformal passivation layer like Al_2O_3. Here, we would like to highlight the improvement in J_{SC} values above 39 mA/cm^2 achieved by tetragonal-star-shaped IPs, while the highest J_{SC} value for an upright pyramid is 37.7 mA/cm^2. Thus, J_{SC} was improved by more than 3% compared to upright pyramids. Even though the FF values were lower than they are for upright pyramids, which indicates that the metallization step should be optimized, η was improved by around 1% with the help of tetragonal-star-shaped IPs.

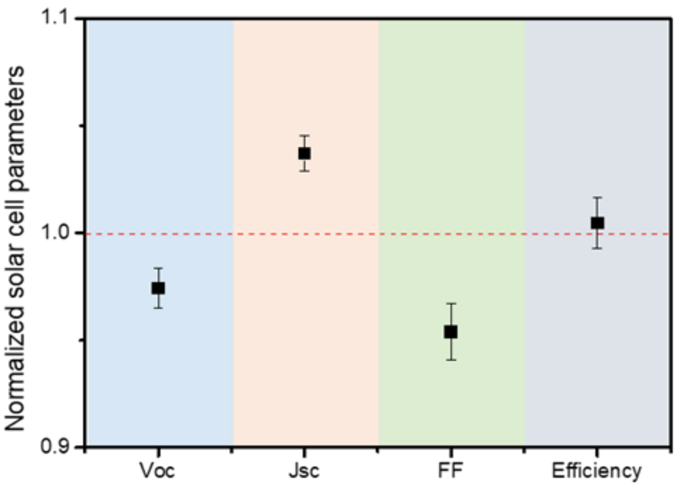

Figure 3. 15. Solar cell parameters fabricated on tetragonal-star-shaped IPs normalized for upright pyramids.

3.4.3 Formation of Inverted Pyramids with Nitric Acid Oxidizing Agent

The oxidizing agent H_2O_2 was switched to HNO_3 to decrease process temperature and increase the controllability of etchant. The molarities of HF, $Cu(NO_3)_2$, HNO_3 were fixed at 5.4 M, 8 mM, and 1.1 M, respectively. The process temperatures were room temperature, 40°C, and 50°C. Figure 3.16 shows the reflectance results for two different temperatures and various durations. The surface reflectivity was significantly high compared to the previous IP results, both results for the temperatures and durations. However, surprisingly, the $R_{weighted}$ values were comparable with random pyramid texturing after 1 minute of etching. For longer etching durations, the surface reflectance increased suddenly, and at 8 minutes of etching, it became significantly high for solar cell applications. On the contrary to the previous IP study, the solution was capable of texturing Si at lower temperatures, resulting in IPs on the surface.

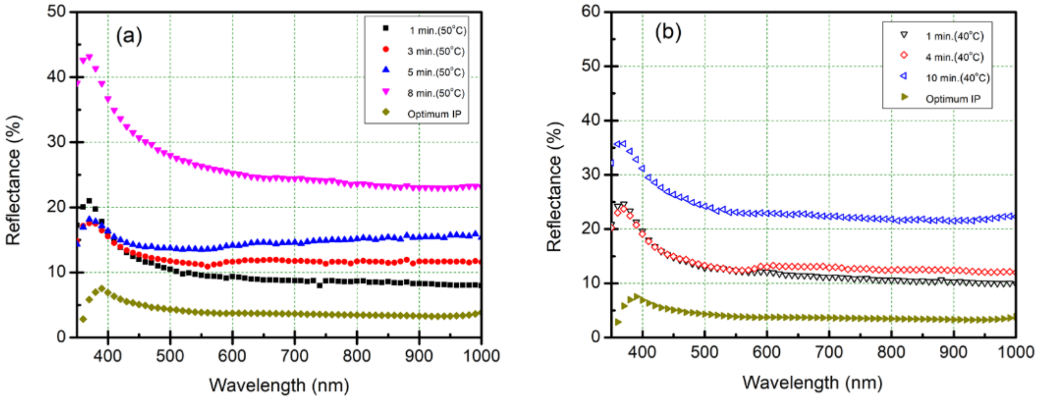

Figure 3. 16. Spectral reflectance results of Si surface after etching for various durations at (a) 50°C and (b) 40°C.

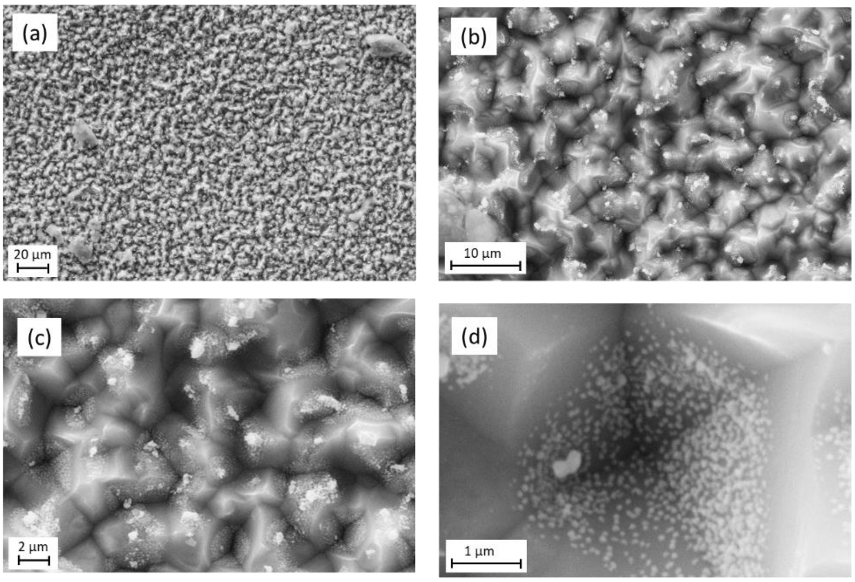

Figure 3. 17. SEM images of texturing for 1 minute of etching at 50°C.

The etching of Si at 40°C resulted in inverted pyramids on the surface after 1 minute of etching. However, at both 40°C and 50°C, the surface coverage of IPs was significantly low, and the size of Cu NPs was more prominent than in the previous study (see Figure 3.17). At the same time, the average diameter size increased from 30 to 100 nm.

Contrary to the solution's behavior with H_2O_2, the solution prepared with HNO_3 can etch and modify the surface at room temperature. After 10 minutes of etching, the surface reflectance decreased to 10%, which is almost the same with random pyramid texturing (see Figure 3.18 (a)). We found that the solution had anisotropic behavior resulting in pyramid-like structures as shown in Figure 3. 18 (b), and HNO_3 improved the solution's nucleation kinetics, resulting in larger Cu NPs on the Si surface. The solution enables the processing of five successive sets of wafers resulting in the same surface morphology and reflectivity.

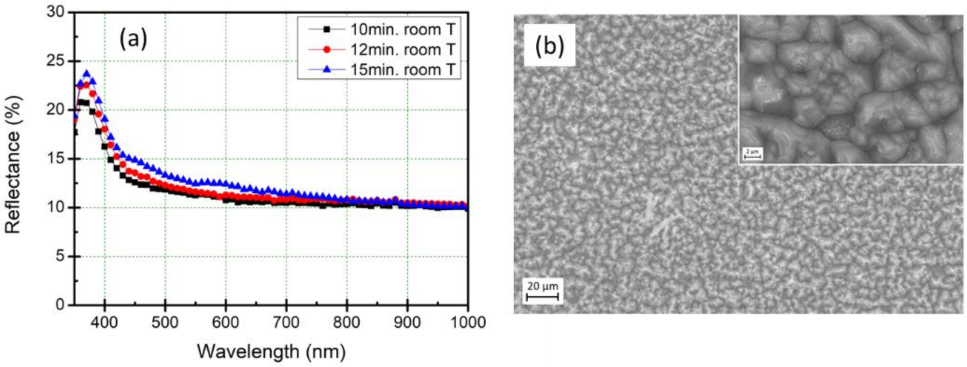

Figure 3. 18. (a) Reflectance results and (b) SEM images of room temperature texturing.

3.5 Conclusions

In this part of the study, we analyzed the relationship between the etchant molarity of $Cu(NO_3)_2$ and Si surface morphology. Four different surface morphologies were observed: porous-like, elliptical-shaped, IP, and star-shaped IP. The well-defined IPs are observed after 15 minutes of etching with 8 mM molarity of $Cu(NO_3)_2$, resulting in 3.74% weighted reflectance. The time-dependent etching of Si identifies the formation of IPs. The surface morphology becomes elliptical-shaped for the first 5 minutes, and IPs become defined after 10 minutes of etching. The impact of the molar concentration of the reductant and oxidant on the surface morphology, etching direction, and etch rate was also clarified. We found that depending on the molarity of HF, the etching behaves like an isotropic etchant. The process temperature was one of the deterministic parameters for the solution's etched surface morphology and pH. Next, by gradually increasing process temperature from 50°C to 55°C in 15 minutes, the tetragonal-star-shaped surface morphology was achieved, resulting in 2.65% $R_{weighted}$, the lowest spectral reflectance value obtained in the literature using this methodology. Moreover, Al-BSF solar cells were fabricated with the tetragonal-star-shaped IPs and upright pyramids. The J_{SC} and efficiency values of Al-BSF Si solar cell were improved significantly with the help of tetragonal-star-shaped IPs by almost 3% compared to upright pyramids.

Thereafter, the oxidizing agent was changed from H_2O_2 to HNO_3 to precisely control the etching. The molarities of HF, $Cu(NO_3)_2$, HNO_3 were kept fixed, and the impact of temperature was clarified under three different temperatures: room temperature, 40°C, and 50°C. The IPs formed with the solution containing HNO_3, resulting in a slightly higher surface reflectivity than the previous study. When using HNO_3, the IPs could form at 40°C, but it also enabled modification of the surface even at room temperature compatible surface reflectance with random pyramid texturing, resulting in around 10% reflectance. This was the first time room temperature texturing of Si with the Cu-ACE method was demonstrated.

CHAPTER 4

SURFACE PASSIVATION

4.1 Introduction

The passivation of the recombination centers on the c-Si surface is a crucial step for performance enhancements of SHJ solar cells [52], [86]. Although the bulk c-Si structure is almost defect-free, the surface of the c-Si wafer is suffering from dangling bonds and contaminations, which create defects on the surface and behave as a recombination center for the charge carriers [87]. Surface recombination of c-Si ia a challenging task in achieving high-efficiency values. Therefore, many recent studies have been carried out to develop the passivation process and passivation materials [88]–[90]. Using different candidates, such as a-Si:H, $SiN_{X,}$ and metal-oxides, as a passivation layer, are offering promising options [89]–[91].

The initial surface condition of Si wafers has a detrimental effect on the surface passivation quality. For this reason, chemical surface cleaning steps are necessary after texturing to obtain low interface defect density between c-Si and a-Si:H interface [92]. Accordingly, the Si surface must be cleaned from metallic and organic impurities using wet chemical processes [93]. The surface layer could be introduced to the contaminants found in the fabrication line or surroundings during the crystal growth of Si or the fabrication process of solar cells. The purity of chemicals and beakers, condition of process tools, fabrication environment, and possible cross-contamination sources has a detrimental effect on the surface passivation quality [94]. Therefore, it is crucial to find, trace and eliminate potential contamination sources in the fabrication lines and surroundings to improve fabrication stability and solar cell performance.

In SHJ solar cell structure, an intrinsic hydrogenated amorphous silicon ((i) a-Si:H) layer is deposited on top of the c-Si resulting in an excellent passivation quality; this structure is easy to manufacture and apply for high-efficiency solar cells [29]. The PECVD technique is commonly used for deposition of the (i) a-Si:H thin film [95], [96]. One of the main advantages of the PECVD is the low deposition temperature [97]. The passivation quality of the a-Si:H layer depends on the chemical passivation of dangling bonds. Both the "H" content and interface defect density (D_{it}) have a direct impact on the minority carrier lifetime [98]. Many research groups have introduced hydrogen plasma treatment to improve the passivation quality of the (i) a-Si:H layer. In addition to deposition conditions of the (i) a-Si:H layer, H-plasma treatment significantly improves minority carrier lifetime values, compared to reference samples where there is no H-plasma treatment [99], [100].

There are conflicting reports that have tried to explain the light and temperature-induced degradation profile of SHJ solar cells. Some reported a decrease in the performance of SHJ solar cells under illumination and temperature, mainly because of increased series resistance and decreased FF values [101]. Others reported improvement in efficiency since surface passivation properties are enhanced [102]. However, most research groups seem to agree on the role of hydrogen atoms in forming dangling bonds due to the exchange of H atoms under illumination and heat called the Staebler-Wronski effect [103], [104]. To overcome this problem, using carbon (C) alloyed in (i) a-Si:H matrix has shown relatively good temperature stability, which is one of its essential advantages along with the increase in the optical band gap [105][97]. The optical band gap of (i) a-Si:H is measured at around 1.74 eV [106], and with the a-SiC_x:H layer, it can be enlarged up to 3 eV [107]. The enlarged optical band gap decreases the parasitic absorption losses. Moreover, introducing carbon to a-Si:H matrix leads to higher temperature stability due to the stronger hydrogen-carbon bonds [108], [109]. However, C would cause the resistivity of the thin film to increase, which would, in turn, aggravate the resistive losses. Overall, applying a-SiC_x:H as a passivation layer is a valuable alternative to improving parasitic losses.

In this chapter, the impact of surface contaminants on passivation quality will be presented by detailed elemental analysis. The cross-contamination arising from the surroundings and successive chemical processes will be discussed. After that, the impact of (i) a-Si:H deposition parameters on the passivation quality will be discussed in terms of D_{it}, H content, and lifetime results. Finally, the wide band gap passivation layer (a-SiC_x:H) will be examined and discussed using ToF-SIMS, FTIR, and PCD methods.

4.2 Experimental

Two different substrates were used for the (i) a-Si:H passivation and cross-contamination studies in this study. The passivation study was conducted on DSP, FZ, 1-3 ohm.cm, n-type Si wafers with 275 µm thickness, and the cross-contamination study was carried out on DSP, CZ 1-3 ohm.cm, n-type Si wafers. The wafers were cleaned by standard RCA-2 and piranha solutions, followed by oxide removal using HF:HCl:H_2O (1:1:10) after each cleaning step. After the oxide removal step, wafers were rinsed with deionized water (DIW). Cleaned wafers were then loaded to the GünEr PECVD cluster system for deposition of a-Si:H layers, where capacitively coupled plasma (CCP) was used at 13.56 MHz. Process flow for the preparation of the passivation sample and its cross-sectional view can be seen in Figure 4.1.

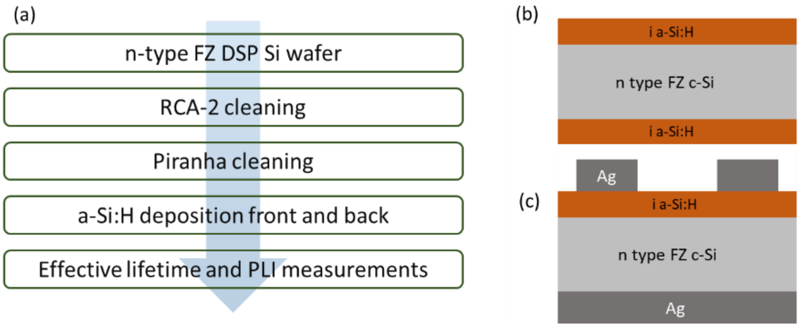

Figure 4. 1. (a) Fabrication process flow and (b) the cross-sectional view for passivation sample and (c) for C-V measurement sample.

To identify the relationship between deposition parameters and passivation quality, ‘H’ dilution ratio, deposition power, the thickness of (i) a-Si:H layer, deposition pressure, reliability and reproducibility of processes, total gas flow, and hydrogen (H) plasma treatment were studied. After deposition of (i) a-Si:H layer on both sides of c-Si wafer, samples were characterized by lifetime tester (Sinton) and PLI-1001 (Semilab) for 1x10^{15} cm^{-3} minority carrier density for both tools. Moreover, the infrared absorption spectrum was measured by a Fourier transform infrared (FTIR) spectrometer (Bruker Vertex 80 V) within the wavelength range of 400 to 3000 cm^{-1} using absorbance mode and 4 cm^{-1} resolution to determine ‘H’ content of (i) a-Si:H and (i) a-SiC$_x$:H layers. The D$_{it}$ and fixed charge density (Q$_{fix}$) were evaluated by capacitance-voltage (C-V) and conductance-voltage (G-V) measurements at different frequencies (f) between 10 kHz and 1 MHz on the samples shown in Figure 4.1 (c). As illustrated in the figure, these samples were obtained by the thermal evaporation of silver (Ag) on both sides of n-type DSP Si wafer as front dot contact and back contact as full rear coverage of the surface. The thicknesses of Ag contacts was 300 nm, and the diameter of dot contact was 500 µm [110], [111]. The thickness of each a-Si:H layer was determined by spectroscopic ellipsometry measurements (Semilab) using the Tauc-Lorentz model [97]. The Tauc-plot extrapolation was used to calculate the optical band gap of (i) a-SiC$_x$:H layers by UV-Vis-NIR spectrometer (Bentham PVE 300). Moreover, the elemental analysis of (i) a-SiC$_x$:H / (i) a-Si:H layers and also interface/bulk properties were investigated using time-of-flight secondary ion mass spectroscopy (ToF-SIMS) technique (ION-TOF ToF-SIMS 5).

The contamination problem during experiments was identified and tracked through Tof-SIMS measurements and inductively coupled plasma mass spectroscopy (ICP-MS) analysis (Perkin Elmer DRC II). The correlation between cross-contaminants and passivation was performed using effective lifetime and PLI measurements.

4.3 Results and Discussions

4.3.1 Passivation Quality of a-Si:H Layer

The deposition parameters of (i) a-Si:H are crucial to obtain excellent passivation properties. This chapter explores the impact of hydrogen dilution, deposition pressure, power density, (i) a-Si:H layer thickness, and post-hydrogenation in detail.

4.3.1.1 The Impact of Hydrogen Dilution Ratio on Passivation Quality

Different H_2/SiH_4 dilution ratios called R_{H_2} were used during depositions under fixed substrate temperature (200°C), fixed deposition power density (64 mW/cm^2), and the same thickness of (i) a-Si:H. The deposition parameters are given in Table 4.1.

Table 4. 1. Deposition parameters for various R_{H_2}.

R_{H_2}	$T_{substrate}$ (°C)	SiH_4 flow (sccm)	H_2 flow (sccm)	Pressure (Torr)	Power density (mW/cm^2)
2	200	100	200	0.8	64
3	200	75	225	0.8	64
6	200	43	258	0.8	64
9	200	30	270	0.8	64

The thickness of each deposition was determined by spectroscopic ellipsometry measurements, and this value was fixed to 7 nm for all depositions. The effective lifetime and band gap results for various R_{H_2} are shown in Figure 4.2.

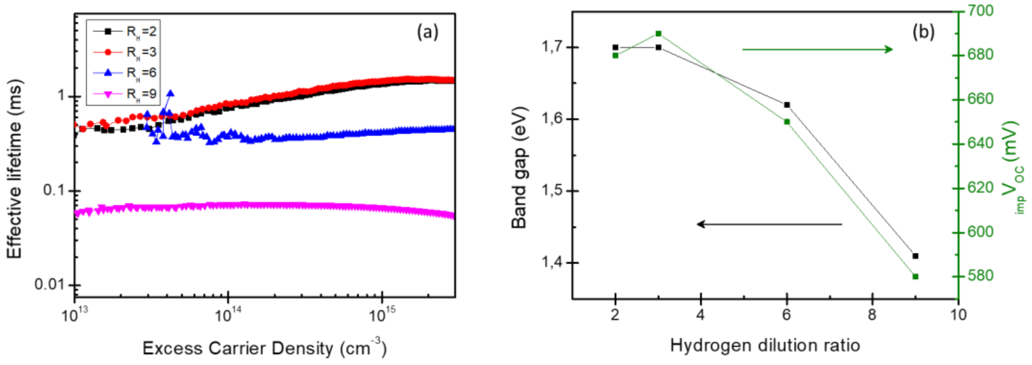

Figure 4. 2. (a) Effective lifetime vs. excess carrier density results and (b) band gap/$_{imp}V_{OC}$ results for various hydrogen dilution ratios.

The results showed that an increased dilution ratio of SiH_4 leads to a decrease in E_g, effective lifetime, and $_{imp}V_{OC}$ values. However, at lower dilution ratios of 2 and 3, the passivation quality of a-Si:H layers are high enough and almost the same for both ratios. For a higher dilution ratio of 9, other research groups reported epitaxial growth of a-Si:H [87]. It is well-known that when epitaxial growth occurs, a-Si:H's passivation quality decreases, which will be discussed thoroughly in a later chapter. For the next part of the experiment, R_{H_2} value was prefferred as 3.

4.3.1.2 The Relationship Between Deposition Power Density and Passivation Quality

Higher values of deposition power density cause physical damage to the interface, thus influencing the passivation quality of (i) a-Si:H. Hence, to lessen its impact, the deposition power density should be low enough. To clarify the relationship between deposition power density and passivation quality of a-Si:H layers, 7nm thick layers were studied under three different density values. Other deposition parameters were fixed to the same values as in the previous runs. The results are listed in Figure 4.3.

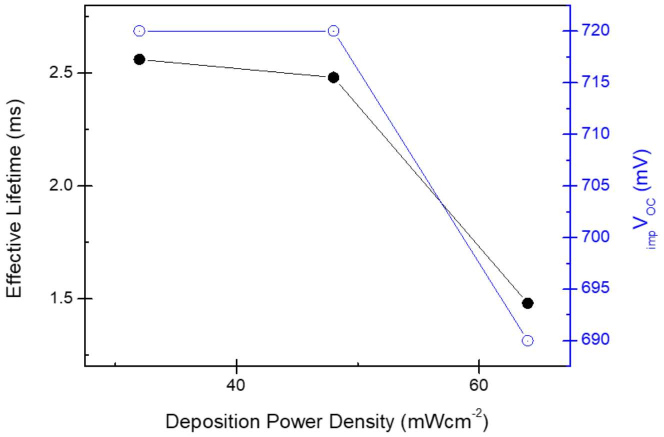

Figure 4. 3. Effective lifetime and $_{imp}V_{oc}$ results for various deposition power densities.

The results indicate that decreasing deposition power led to an increase in $_{imp}V_{OC}$ and effective lifetime. Moreover, from ellipsometry measurements, the band gap value of the layer was found to be around 1.74 eV for deposition power density values of 32 and 48 mW/cm^2 depositions was found to be around 1.74 eV, which is slightly higher than that obtained as 1.45 eV for 64 mW/cm^2 deposition power density. Deposition power density is one of the crucial parameters that affect passivation quality. Lower power density also means lower D_{it}. However, 48 mW/cm^2 was selected for future studies as the optimum deposition power density due to problems faced with the plasma during ignition.

4.3.1.3 The Effect of Deposition Pressure on the Passivation Quality

All variables were fixed, except for the deposition pressure. Due to the butterfly valve limitations of the fabrication tool, it was not possible to make depositions above 1.2 Torr. For this reason, we defined the highest deposition pressure as 1.2 Torr, and used the range below this value to prepare passivation samples with 7 nm (i) a-Si:H layers.

Table 4. 2. Effective lifetime and $_{imp}V_{OC}$ results for various deposition pressures.

Pressure (Torr)	$_{imp}V_{OC}$ (mV)	τ (ms)
1.2	710	2.60
1	700	2.30
0.8	690	1.40
0.6	620	0.24

The results showed that increasing deposition pressure improved (i) a-Si:H layer passivation quality. The highest $_{imp}V_{OC}$ value was observed under 1.2 Torr deposition pressure. Deposition pressure was optimized as 1.2 Torr for the subsequent studies.

4.3.1.4 The Relationship Between Thickness and Passivation of (i) a-Si:H Layer

The optimum deposition conditions, which were determined as $R_{H_2} = 2$, 48 mW/cm^2 power density and 1.2 Torr pressure were used to identify the impact of (i) a-Si:H thickness on the passivation quality. The effective lifetime results can be seen in Figure 4. 4. On the one hand, the passivation quality, effective lifetime and $_{imp}V_{OC}$ values, decreased drastically for less than 7 nm thick (i) a-Si:H layers, especially when the thickness of (i) a-Si:H was 3 nm. The passivation quality was relatively low for the 3nm thick (i) a-Si:H layer. On the other hand, for layers thicker than 7 nm, the passivation quality of (i) a-Si:H decreased slowly with increasing thickness. The highest $_{imp}V_{OC}$ was found as 720 mV, and the highest effective lifetime was 2.5 ms. Interpreting these results, the optimum thickness of (i) a-Si:H layer was determined as 7nm.

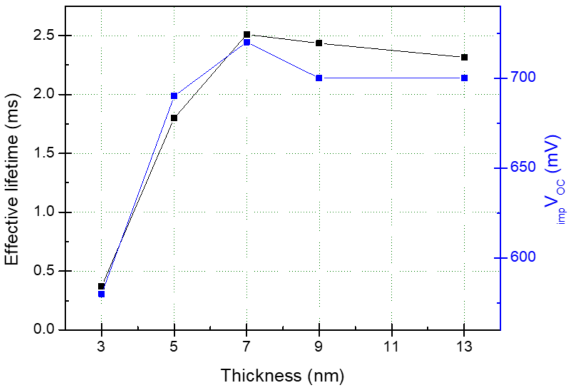

Figure 4. 4. Effective lifetime and $_{imp}V_{oc}$ results for various thicknesses of (i) a-Si:H layer.

4.3.1.5 Hydrogen Plasma Treatment

The hydrogen plasma treatment (HPT) is an efficient way of hydrogenation of thin films and interface, resulting in a decrease in dangling bonds [112], [113]. The HPT process was carried out right after (i) a-Si:H deposition, inside the same chamber and without breaking the vacuum. The following HPT process parameters were analyzed: process pressure, power density, and HPT duration. The results are listed in Figure 4.5 for HPT pressure values of (a) 1 and (b) 1.5 Torr. The filled square sign represents 20 s of HPT, and the empty star sign represents 30 s of HPT.

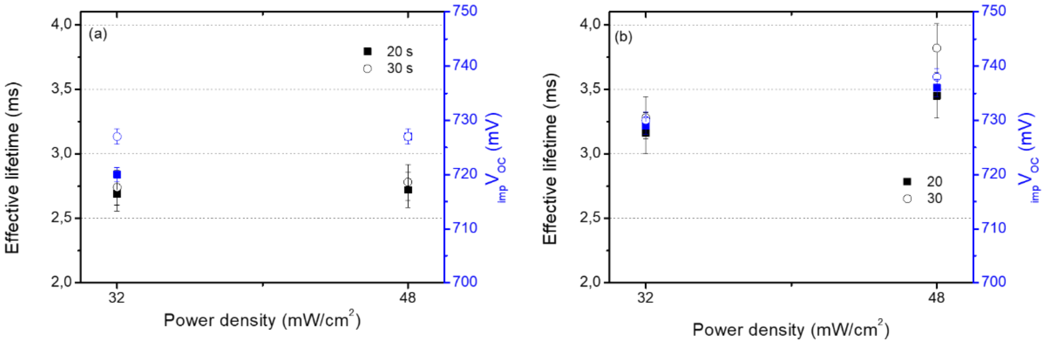

Figure 4. 5. Effective lifetime and $_{imp}V_{oc}$ results after HPT at (a) 1.0 Torr and (b) 1.5 Torr pressures.

Until this point, the highest passivation quality of (i) a-Si:H was obtained with an effective lifetime value of 2.5 ms and $_{imp}V_{OC}$ of 710 mV. When HPT pressure was 1 Torr, there was a slight enhancement on passivation concerning longer treatment time and higher plasma powers resulting in the highest effective lifetime value of almost 3 ms and $_{imp}V_{OC}$ value of 727 mV. Additionally, when HPT pressure increased to 1.5 Torr, the impact of HPT plasma power became more dominant on the passivation quality. Increasing plasma duration and power density improved passivation quality significantly, resulting in 3.8 ms of τ and 738 mV of $_{imp}V_{OC}$. The highest effective lifetime result was shown in Figure 4.6. The optimum deposition recipe was thus concluded as: successive (i) a-Si:H deposition and HPT with the optimum conditions, applied through the following studies.

After HPT, the τ value improved by almost 1.3 ms, and $_{imp}V_{OC}$ improved by 20 mV. Moreover, the c-Si wafer was passivated with the best passivation recipe, including HPT, which was used to clarify passivation properties and time-depending loss in passivation quality. The effective lifetime was measured, and the sample was kept in a cleanroom environment for a week. The lifetime was measured again after one week had passed, and the sample was loaded into the PECVD chamber for another hydrogen plasma treatment. After the second HPT, effective lifetime was measured again. The results of this process can be found in Table 4.3. Only (i) a-Si:H passivation without capping with any other layers, the passivation quality degraded with a decrease in $_{imp}V_{OC}$ value from 710 mV to 690 mV in a cleanroom environment in a week. The Si dangling bond density increases during the stay of passivated sample due to the interaction of light, which is called the Staebler-Wronski effect [114]. However, it is also possible to re-hydrogenate the sample with a second HPT process, resulting in an even higher $_{imp}V_{OC}$ value of 715 mV. It can be concluded that the degradation in passivation properties of (i) a-Si:H is a reversible process by performing the HPT process.

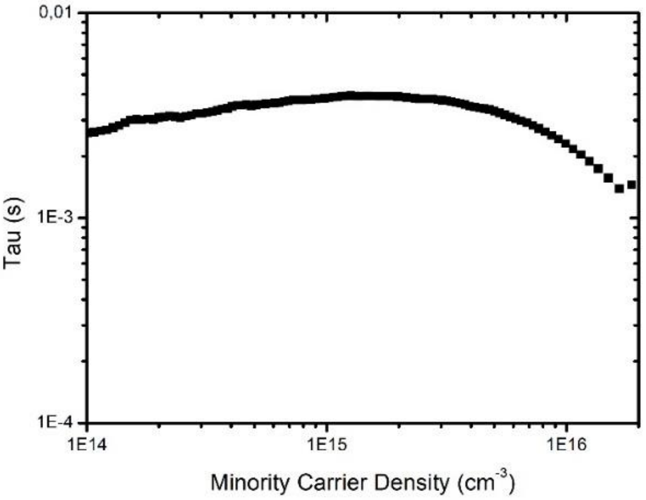

Figure 4. 6. The highest effective lifetime vs. excess carrier density result obtained by optimum deposition conditions.

Table 4. 3. The passivation results of the sample which was kept in a cleanroom for seven days and then re-hydrogenated by HPT.

Sample	$_{imp}V_{OC}$ (mV)	τ (ms)
As deposited	710	2.40
After 7 days	690	1.20
After 2nd HPT	715	2.70

4.3.1.6 Uniformity of (i) a-Si:H

The uniformity control of (i) a-Si:H deposition was performed using a 25 nm (i) a-Si:H deposition on top of the 25x25 cm^2 holder with DSP Si wafers at nine different points represented in Figure 4.7.

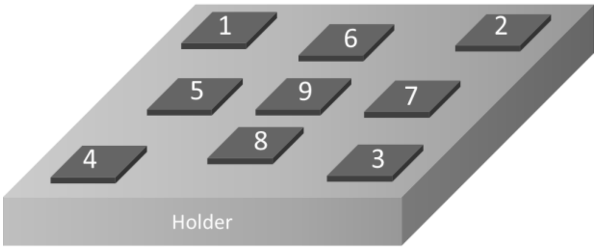

Figure 4. 7. Representative drawing of the holder and wafers for uniformity control.

The thicknesses of each (i) a-Si:H layer was calculated by spectroscopic ellipsometry measurements. The average thickness was 24.88 nm with a standard deviation of 1.16 nm. It can be concluded that uniformity across the whole holder was quite sufficiently good.

4.3.1.7 Interface and Layer Properties of (i) a-Si:H

The passivation properties of (i) a-Si:H layer strongly depend on interface properties between c-Si and (i) a-Si:H, in addition to the H content (C_H) of the layer due to the nature of chemical passivation. FTIR analysis and C-V / G-V measurements explain the impact of hydrogen dilution ratio and HPT process on the layer and interface properties. Table 4.4 lists the vibration modes of silicon peaks from the literature values.

Table 4. 4. Vibrational modes of (i) a-Si:H.

Wavenumber (cm^{-1})	Mode
640	Si-H wagging [115]
2000	Si-H stretching [116]
2010	$Si-H_2$ or $Si-H_3$ stretching [116]
1100	Si-O-Si asymmetric vibration [117]

The hydrogen content in the films was calculated by the following equation [118]:

$$C_H = \frac{A_W}{N_{Si}} \sum_{v_r/W} \frac{\alpha(v)}{v} \Delta v \cong \frac{6400}{d[nm]} \sum_{v_r/W} \frac{-\log(T)}{v} \qquad \text{(Eq.4.1)}$$

where α(ν) is the absorption coefficient, ν_r/w stands for the rocking-wagging bands around 640 cm^{-1}, A_w = 1.6x10^{19} cm^{-2} is the proportionality constant, and N_{Si} =5x10^{22} cm^{-3} is the atomic density of pure silicon. In this calculation, only the bending mode peak that is located around 640 cm^{-1} was considered. The Peak Fit program was used for the extraction, sectioning, and base-line addition. The transmittance results between 350 to 3550 cm^{-1} wavenumber are shown in Figure 4.8.

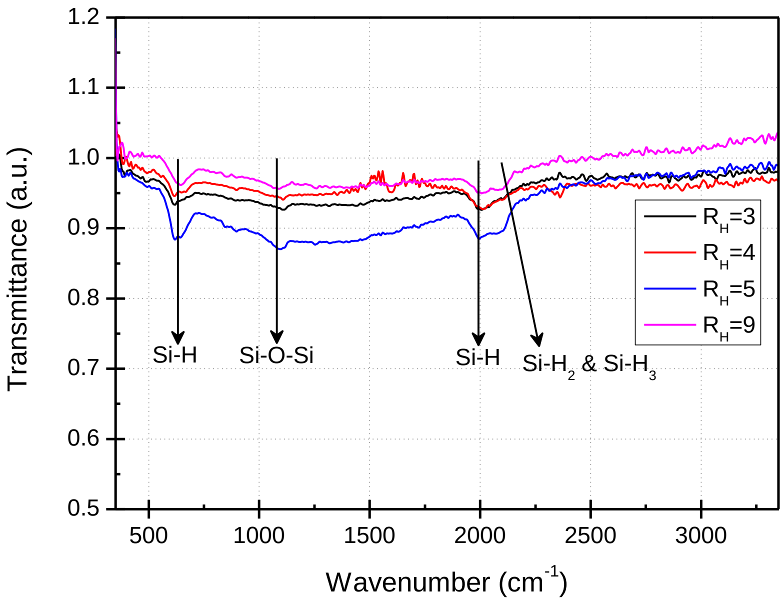

Figure 4. 8. FTIR spectrum for various (i) a-Si:H layers with different hydrogen dilution ratios.

Table 4. 5. C_H results of different (i) a-Si:H films.

R_{H_2}	C_H(%)
3	8.14
4	10.28
5	11.97
9	15.34

The calculated C_H values are listed in Table 4.5. The results showed that a decrease in dilution ratio led to decrease C_H values inside the a-Si:H films. The highest passivation quality was achieved when C_H had the lowest value, which was in the same range of the reported values in the literature [87]. It is worth mentioning that higher hydrogen content of (i) a-Si:H does not imply better surface passivation.

In order to identify the passivation mechanism of the (i) a-Si:H layer, C-V, and G-V measurements for all different samples fabricated by various hydrogen dilution ratios, were performed at different frequencies in the frequency range of 100 kHz to 5 MHz for the voltage range in between -3 V to +3 V changing by 0.2 V increments. The series resistance correction was applied to C-V, and G-V characteristics of the device structure described before with various (i) a-Si:H layers. The C-V and G-V characteristics of the (i) a-Si:H layer deposited at R_{H_2}=3 and power density of 48mWcm^{-2}, are shown in Figure 4.9. It should be noted that the measurement configuration of the impedance analyzer (HP 4192 LF) is parallel conductance and capacitance. The C-V curve has three regimes of accumulation, depletion, and inversion regions [119]. In the depletion and accumulation regions, increased frequency causes the capacitance value to decrease because charges on the interface cannot follow alternative current (AC) signals at high frequencies [120]. However, there is no observable frequency dependency in the inversion region.

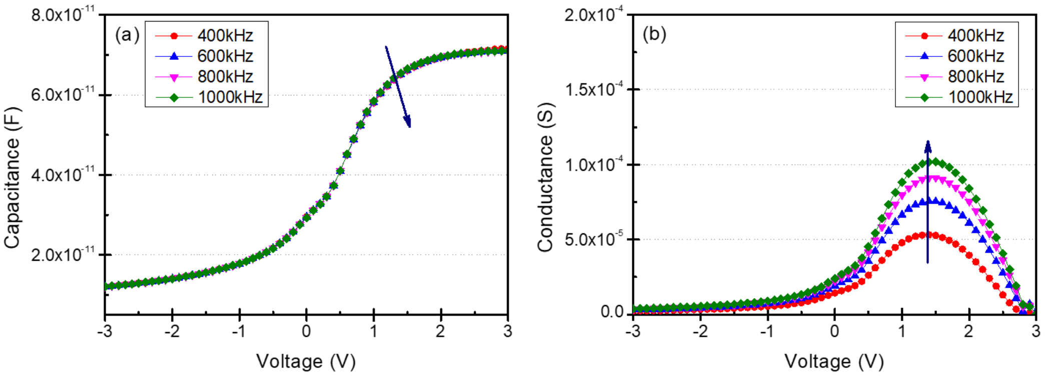

Figure 4. 9. (a) C-V and (b) G-V results between 400 to 1000 kHz frequencies of the device structure explained.

The conductance method [119] was used to calculate the interface defect density (D_{it}) of (i) a-Si:H layer with the following equation:

$$\frac{G_P}{\omega} = \frac{qAD_{it}}{2\omega\tau}\ln(1+\omega^2\tau^2), \qquad \text{(Eq.4.2)}$$

where Gp is the parallel conductance, A is the contact area, ω is the angular frequency, and τ is the relaxation time constant of interface trapped charges. The peak value of G_P/ω vs. ω plot is used to determine D_{it} values using the following expression [119]:

$$D_{it} = \left(\frac{G_P}{\omega}\right)_{max}\frac{2.5}{Aq}. \qquad \text{(Eq. 4.3)}$$

Table 4.6 lists all calculated and measured parameters of C-V/G-V, FTIR, and effective lifetime measurements together.

Table 4. 6. Calculated/measured C, D_{it}, C_H, ${}_{imp}V_{OC}$, and effective lifetime values for the (i) a-Si:H layer grown with various dilution ratios.

R_{H_2}	$C_{i\text{-}aSi}$ (F)	D_{it} ($eV^{-1}cm^{-2}$)	C_H (%)	${}_{imp}V_{OC}$ (mV)	τ (µs)
3	$9.76\text{x}10^{-11}$	$1.89\text{x}10^{11}$	8.14	730	2500
4	$7.59\text{x}10^{-11}$	$2.85\text{x}10^{11}$	10.28	700	1600
5	$9.8\text{x}10^{-10}$	$4.11\text{x}10^{11}$	11.97	600	460
9	$6.83\text{x}10^{-9}$	$2.63\text{x}10^{12}$	15.34	550	50

The lowest D_{it} value observed is $1.83\text{x}10^{11}$ $eV^{-1}cm^{-2,}$ and increasing the hydrogen dilution ratio leads to a significant increase in D_{it} values, especially for higher percentages. At the same time, the C_H of (i) a-Si:H layers was increasing for the higher hydrogen dilution ratio. Surprisingly, the sample growth of the hydrogen dilution ratio of nine for both C_H and D_{it} values was much higher than in other conditions. It was found that there is a strong correlation between D_{it} values, effective lifetime results, and C_H values. The lower the D_{it} value is, the higher the passivation quality of (i) a-Si:H layer. Contrarily, a lower C_H value, primarily if lower than 10%, results in better passivation quality.

The effect of the HPT process on the interface and (i) a-Si:H layer was explored, and the comparison of the best (i) a-Si:H deposition condition in terms of passivation quality showed that the HPT improves both interface quality and dangling bonds by decreasing D_{it} and increasing C_H inside the film as given in Table 4.7. To sum up, the values for the film with highest passivation quality were: $D_{it} = 7.62\text{x}10^{10}\ \text{eV}^{-1}\text{cm}^{-2}$, $C_H = 9.45\%$, $_{imp}V_{OC} = 740$ mV and effective lifetime of 3.8ms.

Table 4. 7. The results for (i) a-Si:H with and without the HPT process.

Sample	**$C_{i\text{-}aSi}$ (F)**	**D_{it} ($eV^{-1}cm^{-2}$)**	**C_H (%)**	**$_{imp}V_{OC}$ (mV)**	**τ (µs)**
without HPT	$9.76\text{x}10^{-11}$	$1.89\text{x}10^{11}$	8.14	730	2500
with HPT	$1.23\text{x}10^{-12}$	$7.62\text{x}10^{10}$	9.45	740	3800

4.3.2 Contamination and Passivation Relation

The $_{imp}V_{OC}$ values after (i) a-Si:H deposition with the optimum recipe, including HPT step, were decreased below 700 mV in the following days. The abrupt degradation of (i) a-Si:H passivation quality led us to trace and identify possible contamination sources and relations. Thus, we first checked possible sources of contamination such as handling, holder of the tool, and cross-contamination from successive depositions. Then, we focused on the contamination sources exposed during the wet chemical process. A summary of these studies with discussions is given below.

4.3.2.1 PL Image Investigation on Passivated Samples

The PL imaging tool monitors effective lifetime results of the passivated sample across the whole wafer, using the microwave photoconductance decay method to detect and measure with PL images [121]. The tool makes it possible to detect local maximum or minimum passivation quality by imaging. The optimum deposition conditions of (i) a-Si:H layer, including the HPT process, were used throughout this study. We examined how plastic tweezers, Teflon holder used in the last oxide removal step, thermal tape used during deposition to fix the sample, PECVD holder, and showerhead affected the passivation quality. In our first design of the PECVD holder, we used a borosilicate glass carrier for Si wafers and thermal tapes to fix the sample during deposition. Figure 4.10 (a) shows the dead spaces of the passivated sample on the corrected and calibrated PL images with the intensity and lifetime scale, respectively. The intensity and lifetime scales are given at the bottom of the images. It was found that the thermal tape has degraded the passivation quality for almost a distance of 1 cm from the tape by releasing C during deposition and thus, resulting in less than 1 ms effective lifetime result as the highest quality. Moreover, cross-contamination resulting from the use of plastic tweezers was detected from PL image results, as the passivation quality looks dead for the areas touched by the tweezers. Later, the contamination from the V-shaped Teflon holder used during the wet chemical process was detected, which had degraded the passivation on the contact points, resulting in average effective lifetime values of less than 0.5 ms on the whole wafer as shown in Figure 4.10 (b). The main reason for this was related to the shared use of holders for different chemical processes. The next point is the showerhead design. A higher amount of deposition in the chamber led to blockage of the holes of the showerhead. With an overgrowth in the chamber, the passivation quality was totally killed for points just below the showerhead opening (see Figure

4.10 c). Furthermore, the overall passivation quality significantly decreased, resulting in less than 0.1 ms effective lifetime value. In the case of overgrowth, the only way to recover deposition quality is by cleaning the chamber.

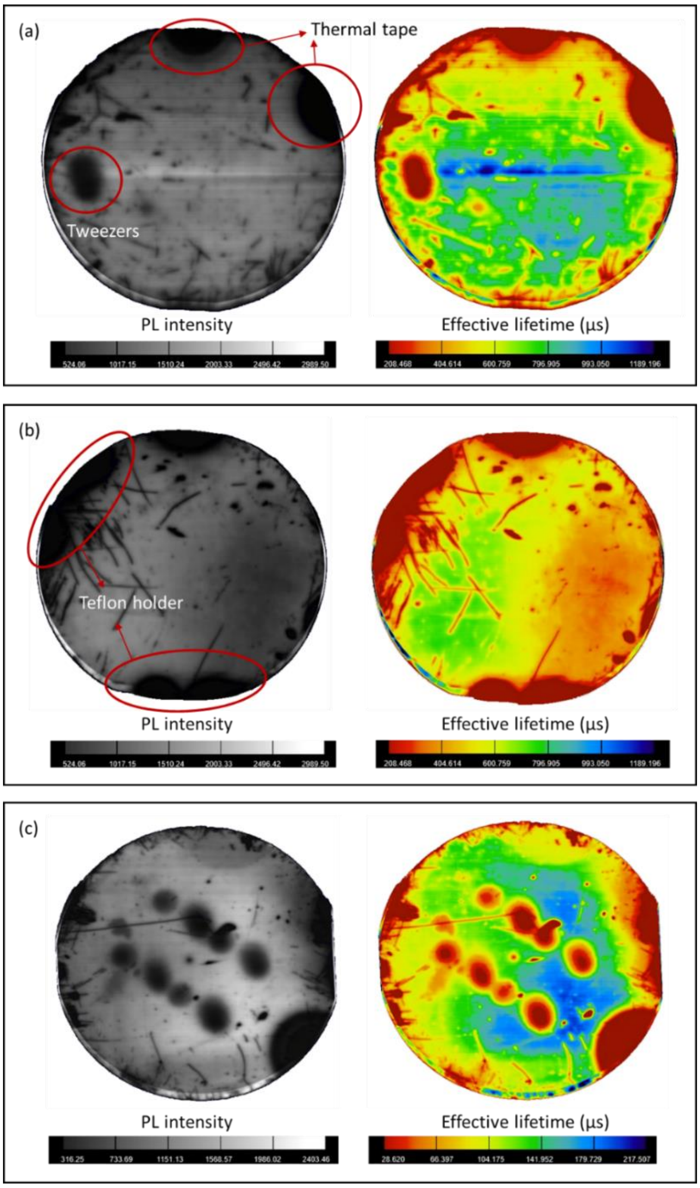

Figure 4. 10. Corrected (left) and calibrated (right) PL images of (i) a-Si:H passivated samples showing the influence of (a) tweezers/thermal tape, (b) Teflon holder, and (c) showerhead.

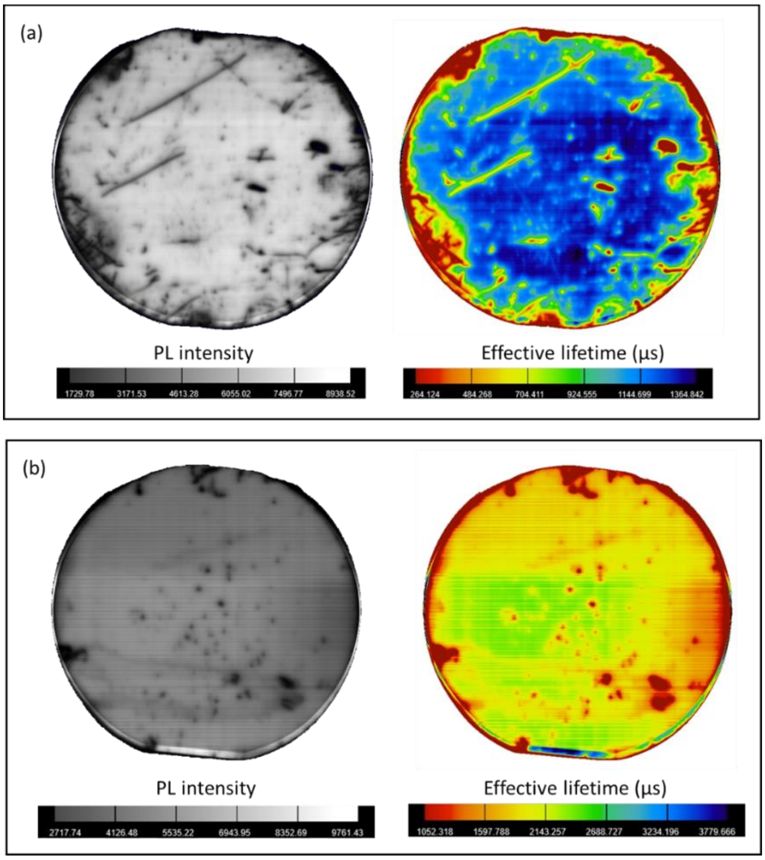

Figure 4. 11. Corrected (left) and calibrated (right) PL images of (i) a-Si:H passivated samples showing (a) scratches due to glass holder and (b) with new Al holder.

Figure 4.11 (a) shows the PL images of the passivated sample after cleaning the Teflon holder and changing the plastic tweezers to a new one, where depositions of (i) a-Si:H layer were carried out without using any thermal tape. The images clearly showed that the cross-contamination from the holder, tape, and tweezers were eliminated, resulting in an effective lifetime of 1.2 ms and ${}_{\mathrm{imp}}V_{OC}$ less than 700 mV. However, some scratches were visible on the PL images caused by the movement of the glass holder inside the system. Thus, we switched the glass holder to a fixed shape aluminum holder suitable for 4” Si wafers. The visible problems on the PL images after (i) a-Si:H passivation seemed to be fully solved after the integration of the aluminum holder, as shown in Figure 4. 11 (b). The average effective lifetime was 2.1 ms, resulting in an ${}_{\mathrm{imp}}V_{oc}$ value of around 700 mV. However, the passivation quality was still far from the previous studies'. Therefore, we moved on to analyzing the possible contamination sources from wet chemical processes.

4.3.2.2 Contamination from Wet Chemical Processes

While (i) a-Si:H layer was damaged from the lack of passivation, the quality of SiO_2 growth passivation also degraded at the same time period. Moreover, after SiO_2 passivation, PL imaging measurements detected dark spots that imply dead areas in terms of effective lifetime, as shown in Figure 4. 12.

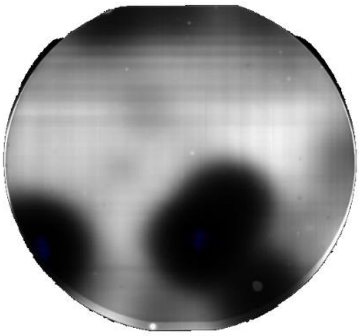

Figure 4. 12. PL images of the sample passivated with SiO_2.

The ToF-SIMS measurement was performed on the dark spots of the SiO_2 passivated sample. As can be seen from the results shown in Figure 4.13, the analyzed region of the sample contains significant Cu, Na, K, and Ca contaminations. A small amount of Fe was also detected at the surface. Then, the samples that were exposed to any wet chemical step in the same wet benches for various days/weeks/years were investigated using ToF-SIMS measurements. Figure 4. 14 lists the timeline versus detected contaminants for different sample preparation steps. For the samples prepared between 2018 and 2019, we noticed three common metallic contaminants: Al, Fe, and Cu. The only common processes among these applications were the wet chemical processes of RCA-1, RCA-2, and oxide removal, performed at the same wet bench. We detected metallic contaminations for all samples exposed to chemical processes in the wet bench area. Despite having separated the baths and quartz for different processes, the contaminants were the same for all.

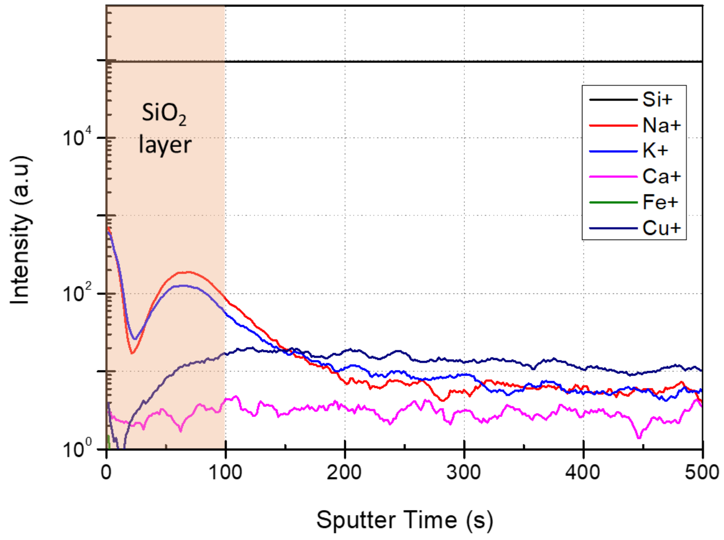

Figure 4. 13. ToF-SIMS result of the SiO_2 passivated sample.

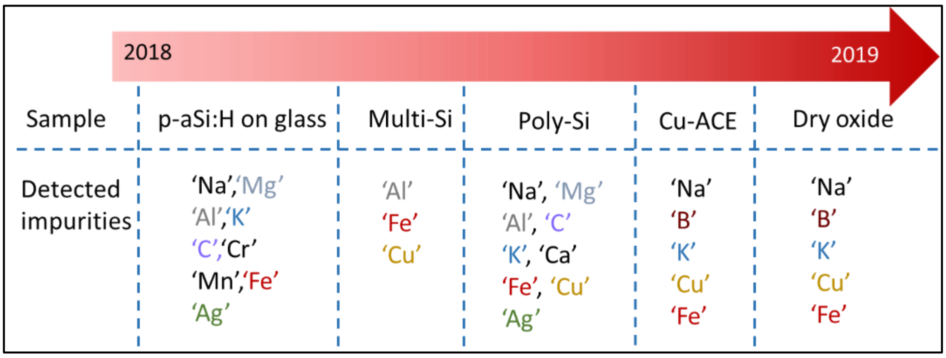

2018 → 2019

Sample	p-aSi:H on glass	Multi-Si	Poly-Si	Cu-ACE	Dry oxide
Detected impurities	'Na','Mg' 'Al','K' 'C','Cr' 'Mn','Fe' 'Ag'	'Al' 'Fe' 'Cu'	'Na', 'Mg' 'Al', 'C' 'K', 'Ca' 'Fe', 'Cu' 'Ag'	'Na' 'B' 'K' 'Cu' 'Fe'	'Na' 'B' 'K' 'Cu' 'Fe'

Figure 4. 14. Impurities detected by ToF-SIMS measurements for different applications and processes.

Detailed analyses were done about the types of equipment used in these chemical processes and found that wet bench components, baths, quartz beakers, and hotplates as a possible sources for contamination. The primary source of contamination we found was the rusted stainless steel parts of the wet bench, penetrating the quartz beakers. All metallic components were replaced with plastic ones. In addition, the quartz beakers were cleaned by RCA-2 and HF:HCl:H_2O to get rid of any exposed metallic contaminants from quartz beakers; the set of cleaning processes was carried out twice. After each cleaning phase, n-type Si wafers were rinsed in the standard wet chemical cleaning recipe in the same quartz beakers and used for (i) a-Si:H deposition as a passivation sample. Moreover, a wafer without standard cleaning (RCA-2 and Piranha) was used for (i) a-Si:H deposition right after a single oxide removal step. The results are given in Figure 4.15. Indisputably, the wafers exposed to the wet chemical process inside the cleaned quartz beakers had the lowest passivation quality due to the metallic impurity with an $_{imp}V_{OC}$ value of approximately 650 mV. However, the wafer that did not undergo any cleaning process other than the removal of native oxide and therefore did not get exposed to the quartz beakers achieved the highest passivation quality with an $_{imp}V_{OC}$ value of more than 680 mV. The results indicate that the standard cleaning procedures could not solve the contamination problem.

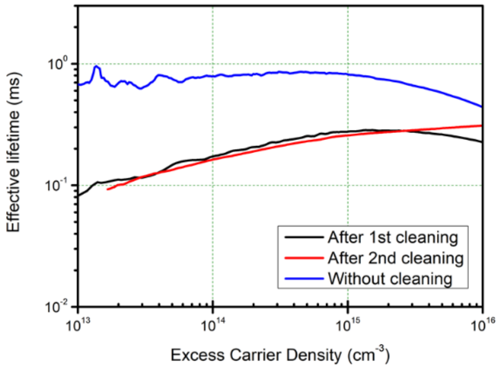

Sample	$_{imp}V_{OC}$ (mV)	Tau (ms) @10^{15} cm^{-3}
After 1st cleaning	655	0.285
After 2nd cleaning	652	0.273
Without cleaning	681	1.000

Figure 4. 15. Effective lifetime results of (i) a-Si:H passivated samples without chemical cleaning and after the first and second quartz cleaning steps.

For RCA cleanings, custom-designed PFA and PVDF beakers (see Figure 4. 16) were used instead of the quartz beakers. Figure 4.16 lists the (i) a-Si:H passivation results, where different beakers were used for the wet chemical cleaning process. B1 and B2 refer to standard cleaning in PFA and PVDF beakers, while B3 represents native oxide removal by dipping into HF:HCl:H_2O filled PP beakers.

Sample Code	Effective lifetime (ms)	${}_{imp}V_{oc}$ (mV)
B1 – i aSi:H (1)	0.872	657
B1 – i aSi:H (2)	0.252	641
B2 – i aSi:H (1)	0.588	644
B2 – i aSi:H (2)	1.030	658
B3 – i aSi:H (1)	0.490	636
B3 – i aSi:H (2)	0.647	645

Figure 4. 16. Effective lifetime results of samples after cleaning in the new PFA (B1) and PVDF (B2) beakers, and only native-oxide cleaning by dipping into $HF:HCl:H_2O$ solution inside the PP beaker (B3).

The results indicate that standard cleaning done in either PVDF or PFA gave better results than non-cleaned samples. Afterward, ToF-SIMS measurements were conducted on the same samples; the detected impurity results can be found in Figure 4.17. The Al^+ and Mg^+ ions were seen only on sample B3, which did not undergo standard cleaning. However, K^+ ions were detected in almost all samples, while the sample cleaned in PVDF beakers contained the highest amount. The primary source of K was the alkaline texturing of Si wafers using KOH solution. Due to the inefficient exhaust venting of wet benches, K contaminants were detected in all types of equipment located at the wet bench areas. After this event, the usage of KOH inside the cleanroom was prohibited. The last contaminant we detected was Ca^+ ions found in the samples that had been exposed to chemicals inside PVDF and PFA beakers. We concluded that neither PVDF nor PFA beakers are suitable for RCA cleanings.

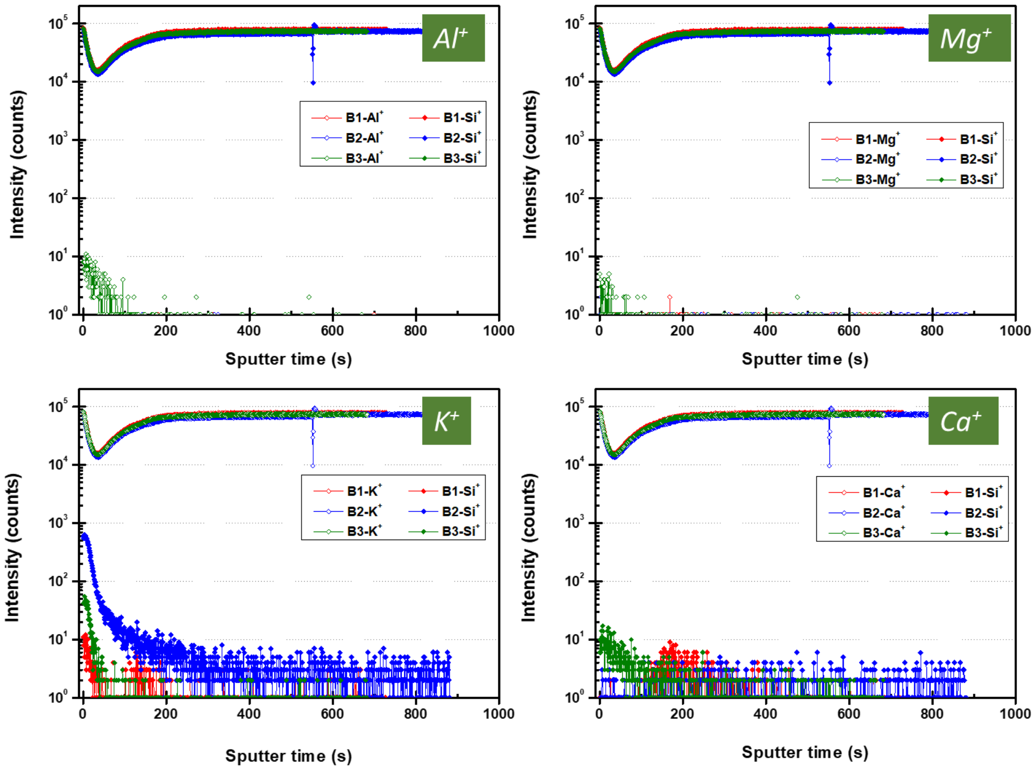

Figure 4. 17. ToF-SIMS results of passivated c-Si samples preliminary cleaned in different beakers, using (i) a-Si:H.

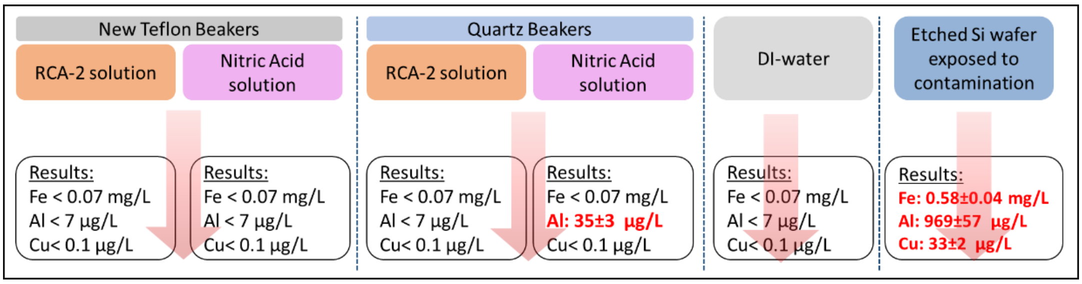
New Teflon Beakers

RCA-2 solution
Results:
Fe < 0.07 mg/L
Al < 7 µg/L
Cu< 0.1 µg/L

Nitric Acid solution
Results:
Fe < 0.07 mg/L
Al < 7 µg/L
Cu< 0.1 µg/L

Quartz Beakers

RCA-2 solution
Results:
Fe < 0.07 mg/L
Al < 7 µg/L
Cu< 0.1 µg/L

Nitric Acid solution
Results:
Fe < 0.07 mg/L
Al: 35±3 µg/L
Cu< 0.1 µg/L

DI-water
Results:
Fe < 0.07 mg/L
Al < 7 µg/L
Cu< 0.1 µg/L

Etched Si wafer exposed to contamination
Results:
Fe: 0.58±0.04 mg/L
Al: 969±57 µg/L
Cu: 33±2 µg/L

Figure 4. 18. ICP-MS results for various possibly contaminated samples.

ICP-MS measurements of the solution prepared in PVDF and contaminated quartz beakers were taken. Two kinds of solutions were prepared in these beakers: RCA-2 and HNO_3:H_2O solutions. In addition to these samples, a piece of silicon wafer exposed to RCA-2 cleaning in the contaminated quartz beaker was etched by HF:HNO_3, and the etched solution was then used for ICP-MS measurement.

Moreover, to be sure about the quality of DIW, the fresh DIW was also analyzed using ICP-MS. For these samples, only three different contaminants were checked: Al, Cu, and Fe. The results are given in Figure 4.18. It was found that the PVDF beakers did not have any metallic contaminants above the detection limit of the ICP-MS method [122]. The RCA-2 solution prepared in quartz beaker did not show any metallic contaminants; however, after the hot HNO_3 solution was prepared in the same beaker, the remaining solution showed Al contamination above the detection limits, for a value of 35±3 µg/L of Al. DIW results were metal-free. The etched Si wafer exposed to RCA clean in the contaminated quartz tank revealed significant metallic contamination. Fe, Al, and Cu concentration values measured 0.58±0.04 mg/L, 969±57 µg/L, and 33±2 µg/L, respectively. Due to the high dose of contamination in the quartz beakers, the new, clean, and high purity quartz beakers; were ordered and used in the standard wet chemical cleaning processes.

After switching to the new quartz beakers, Si wafers were cleaned and used for (i) a-Si:H passivation. Measurements of the passivated sample were taken using Sinton, PL imaging, and ToF-SIMS. ToF-SIMS results are given in Figure 4.19.

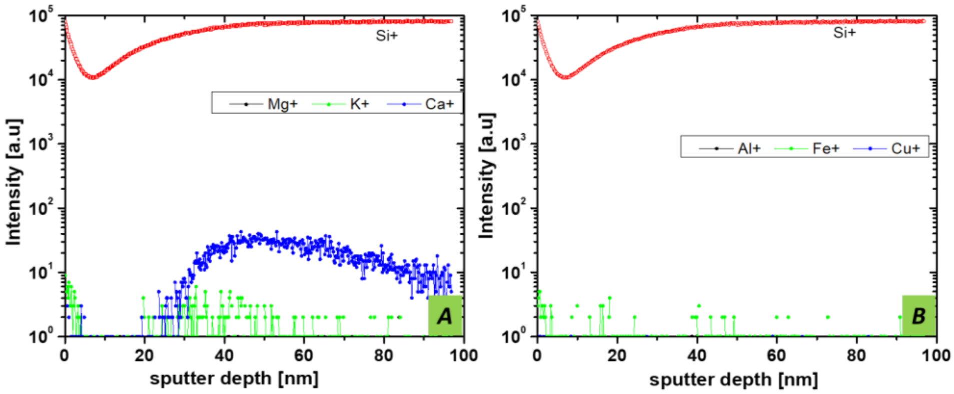

Figure 4. 19. ToF-SIMS measurement profiles for the samples cleaned in new quartz beakers and passivated with (i) a-Si:H layer.

It was concluded that the ToF-SIMS signal of metallic contaminants was significantly reduced, almost below the detection limit for all. The Ca^+ signal was detectable, but the remaining ions were below detection limits. Nevertheless, the detected Ca^+ was related to the composition of the new quartz tank used for cleaning. In Figure 4.20, the effective lifetime result of (i) a-Si:H is given. After switching to new and clean quartz beakers for RCA cleanings, the passivation quality of (i) a-Si:H improved to its previous values, resulting in $_{imp}V_{OC}$ levels higher than 715 mV and an effective lifetime of 2 ms.

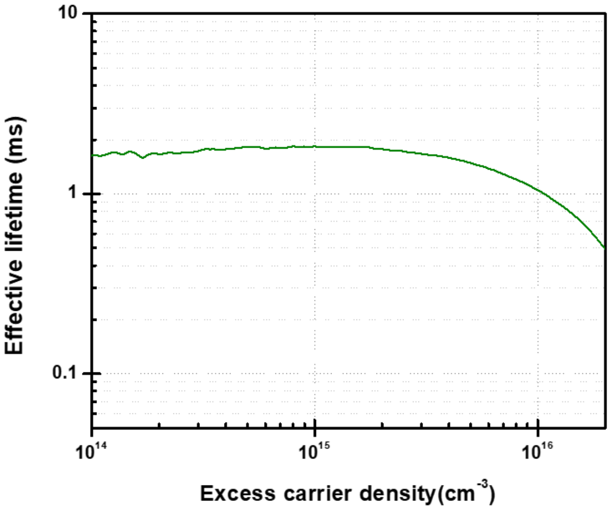

Figure 4. 20. Effective lifetime vs. excess carrier density result of (i) a-Si:H on c-Si wafer cleaned in the new quartz beakers.

It is safe to conclude that tracing each fabrication step to detect and prevent any possible contamination issues is crucial to achieving high device performance, especially for higher passivation qualities.

4.3.3 The Wide Band Gap Passivation layer

Properties of wide band gap material (i) a-SiC_x:H layer was explored to find a way to decrease the parasitic absorption in SHJ solar cells, which is caused by (i) a-Si:H layer. In this part, we studied how a-SiC_x:H deposition conditions affect the electrical and optical properties of the layer. The optical band gap of a-SiC_x:H was determined to be between 1.9 eV to 2.2 eV, depending on deposition conditions. Fixed charge density (Q_{fix}) and D_{it} were analyzed with the conductance method. Additionally, we formulated the correlation between D_{it}, C, and H contents after elemental and chemical analyses. Moreover, silicon to carbon ratio and hydrogen bonding to these two atoms changed depending on the deposition conditions. The passivation quality of a-SiC_x:H was verified by measuring the effective lifetime. An ultra-thin a-Si:H layer was inserted in the structure as a buffer to eliminate the “C” piling problem. The passivation quality of a-SiC_x:H was improved with the a-Si:H buffer layer.

4.3.3.1 Experimental

The properties of a-SiC_x:H layers deposited by radio frequency (RF=13.56 MHz) PECVD reactor (GünEr Cluster System), using various mixtures of silane (SiH_4), hydrogen (H_2) and, methane (CH_4) at 200°C and under 1.2 mTorr pressure were studied. The deposition power density shifted between 48 $mWcm^{-2}$ to 80 $mWcm^{-2}$ to see how the C corporation into the a-Si matrix. The hydrogen flow ratio (R_{H_2}), defined as H_2 mass flow rate divided by SiH_4 flow rate, varied from 2 to 4; and the methane flow ratio (R_{CH_4}), defined as CH_4 mass flow rate divided by SiH_4 flow rate varied from 0.5 to 2. N-type Czochralski (CZ) growth (100) oriented double side polished (DSP), and alkaline textured wafers were used as a substrate, with 5-10 Ω.cm and 1-3 Ω.cm resistivity, respectively. The wafers were cleaned using RCA-2 and RCA-1 following oxide removal by HF:HCl:H_2O (1:1:10) solution. After the last oxide removal step, wafers were dried and immediately introduced into the PECVD system to deposit (i) a-SiC_x:H layer. The thickness of (i) a-SiC_x:H layers were fixed to 7nm for the passivation samples. The Tauc-plot extrapolation was applied to determine the optical band gap of (i) a-SiC_x:H layers using the data measured by UV-Vis-NIR spectrometer (Bentham PVE 300). Furthermore, SemiLab GES 5E did the spectroscopic ellipsometry measurements, and the Tauc-Lorentz model was used to analyze the layers [123].

The infrared absorption spectrum was measured using an FTIR spectrometer (Bruker Vertex 80 V) within the range of 400 to 3000 cm^{-1}, in absorbance mode, and with 4 cm^{-1} resolution. The spectrum of fresh HF-treated bare Si substrate was differentially subtracted from the measured spectrum. The D_{it} and fixed charge density (Q_{fix}) were evaluated by C-V and G-V measurements on n-type DSP Si wafer with thermally evaporated Ag front dot contact and Ag back contact, which fully covers the backside of Si wafer, at different frequencies (f) from 10 kHz to 1 MHz. The thickness of Ag contacts was 300 nm, and the diameter of dot contact was 500 µm.

Elemental analysis of the (i) a-SiC_x:H layer was conducted using the ToF-SIMS technique. Due to the remarkable capability of ToF-SIMS at analytical resolution versus detection limit, it could enlighten many aspects of the structure. The passivation quality of (i) a-SiC_x:H layer was determined by the PCD method in the quasi-steady state and the transient mode depending on the lifetime properties. The passivation samples were prepared on the textured n-type Si wafer with symmetrical coating, whereas the thickness of the layer was fixed to 7 nm.

4.3.3.2 Optical Analysis

The optical band gap values of the a-SiC_x:H layers grown with different deposition parameters were determined by the Tauc plots [123] drown from the data of the absorbance spectra (Figure 4.21) which were obtained from the transmittance measurements performed in the wavelength range of 300 to 900 nm. Assuming a direct optical band gap, E_g values of a-SiC_x:H films were calculated from the Tauc plots shown in Figure 4.22.

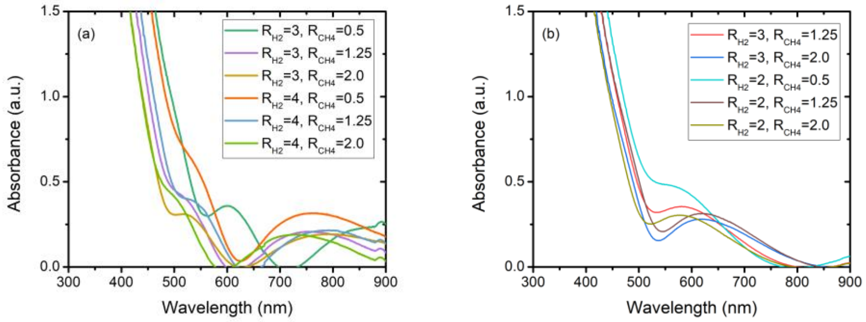

Figure 4. 21. Absorbance spectra of various a-SiC$_x$:H layers grown with different R$_{H2}$ and R$_{CH4}$ values and deposition power density of (a) 80 mWcm^{-2} and (b) 48 mWcm^{-2}.

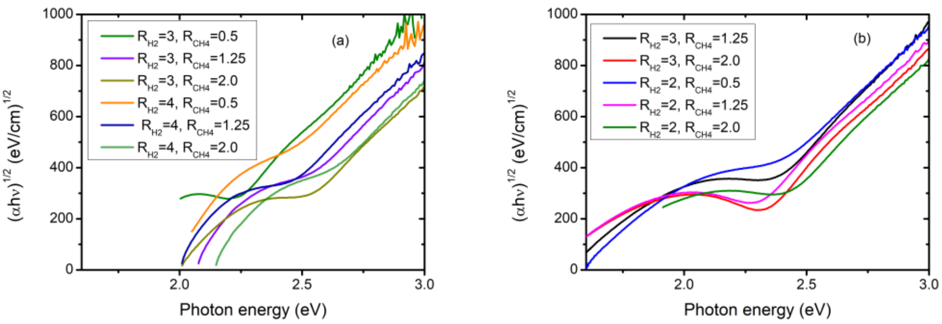

Figure 4. 22. Tauc plots of various a-SiC$_x$:H layers grown with different R$_{H2}$ and R$_{CH4}$ values and deposition power densities of (a) 80 mWcm^{-2} and (b) 48 mWcm^{-2}**.**

In the literature, E$_g$ value of (i) a-Si:H is found in the range of 1.7 eV and 1.8 eV [124]. Variation of band gap energy values with H_2 and CH_4 gas flow rate is shown in Figure 4.23 for (i) a-SiC$_x$:H layers. As given in the figure, the lowest and largest E$_g$ values noted were 1.96 eV and 2.24 eV, respectively. The incorporation of carbon is significantly poor compared to silicon radicals due to the lower sticking coefficient of carbon [125]. Moreover, the CH_4 molecule needs higher energy for decomposition [126]. Therefore, higher R_{CH_4} and power density are required for an efficient C incorporation to a-Si matrix, increasing E$_g$ as a result. As seen in Figure 4. 23 (a) and (b), raising power density from 48 mWcm^{-2} to 80 mWcm^{-2} enhances the decomposition to radicals and incorporation of more C atoms resulting in an increase in E_g. Furthermore; our observations showed that the variation on optical band gap values was quite low, and limited for a-SiC$_x$:H depositions at lower power density levels.

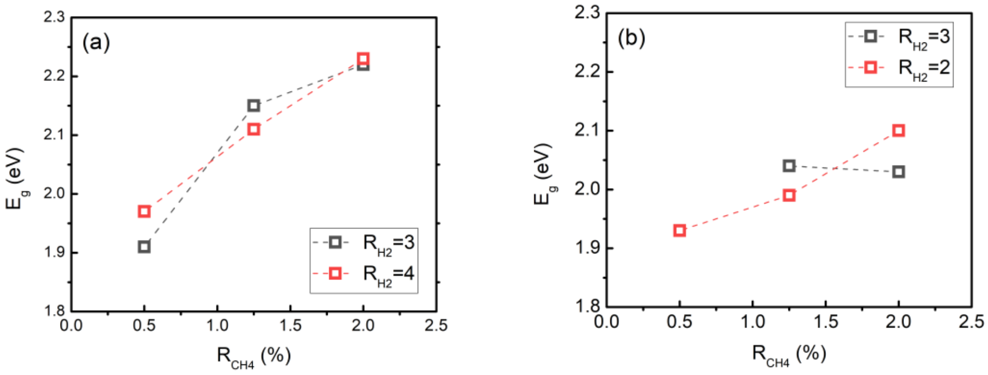

Figure 4. 23. Optical band gap vs gas flow results of a-SiC$_x$:H layers for (a) 80 mWcm^{-2} and (b) 48 mWcm^{-2} deposition power densities.

4.3.3.3 Chemical Analysis

The FTIR measurements were performed between 3000 to 400 cm^{-1} wavenumbers on thin a-SiC$_x$:H films deposited on DSP c-Si wafers with a resistivity of 100 Ω.cm. In order to identify each chemical bond, the FTIR spectra were normalized by the film thickness. The absorbance spectrums are given in Figure 4.24 for samples deposited at R_{H_2}=4 and 80 mWcm^{-2} power density under various methane flow ratios. Several absorption peaks centered at ~650 cm^{-1}, ~770 cm^{-1} [127], ~900 cm^{-1} [128], 1240 cm^{-1} [128], 1340 and 1400 cm^{-1} [129], 2000 and 2100 cm^{-1} are corresponding to Si-H$_n$ wagging or rocking (w/r), Si-C stretching (s), Si-H$_n$ stretching, Si-CH$_3$ wagging (w), (C-H)$_n$ bending (b), Si-H$_n$ stretching modes, respectively. The peaks centered at 2880 and 2950 cm^{-1} related to C-H$_3$ modes could not be detected due to the low C incorporation to the amorphous silicon matrix.

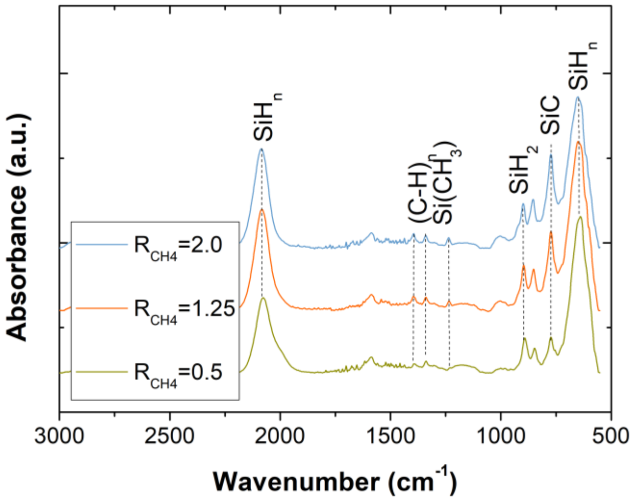

Figure 4. 24. FTIR spectra for the a-SiC_x:H layers deposited under R_{H_2}=4 and 80 $mWcm^{-2}$ power density.

The incorporation of C to the a-Si:H matrix was enhanced with the higher deposition power density and lower dilution of SiH_4 flow, as can be seen in Figure 4. 25. The impact of R_{H_2} was less prominent for relatively low deposition power density levels. However, the H dilution becomes crucial at higher deposition power densities. We observed that the FTIR peaks related to the Si-C (s) bond density decreased at higher dilutions. It should be noted that the positions of FTIR peak for Si-C (s), Si-H (s), and Si-CH_3 (w) chemical bonds were shifted to the lower wavenumbers for ratios higher than R_{H_2} and lower than R_{CH_4} (see also Figure 4. 26 a and b). The vibrational frequency changes due to the reduction of C content, which also led to C atoms being replaced with Si atoms inside the random network of the a-SiC_x:H layer. Due to the change in electro-negativity between these two atoms, the inter-atomic expanse of Si-C, Si-H, and Si-CH_3 bonds also shifted [130].

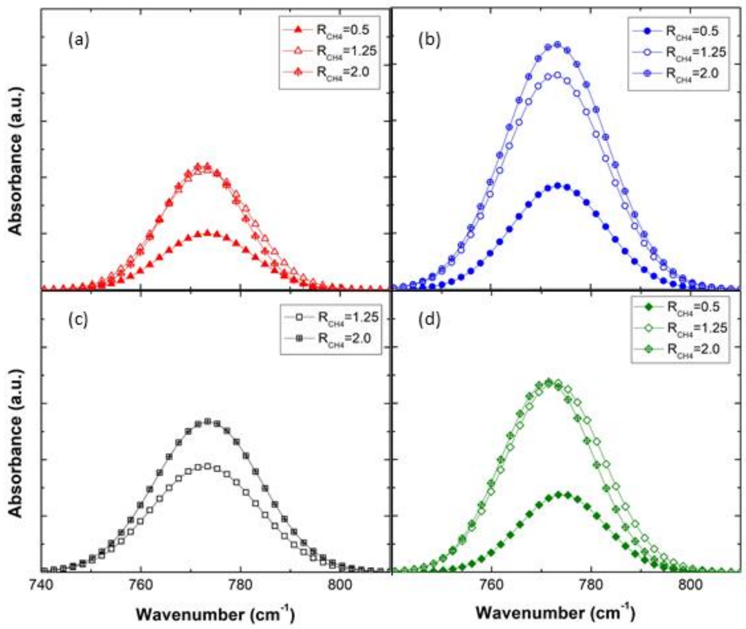

Figure 4. 25. FTIR spectrum for Si-C stretching mode centered at 770 cm^{-1} for the a-SiC_x:H deposited at (a) R_{H_2}=2, 48 $mWcm^{-2}$, (b) R_{H_2}=3, 80 $mWcm^{-2}$, (c) R_{H_2}=3, 48 $mWcm^{-2}$ and (d) R_{H_2}=4, 80 $mWcm^{-2}$.

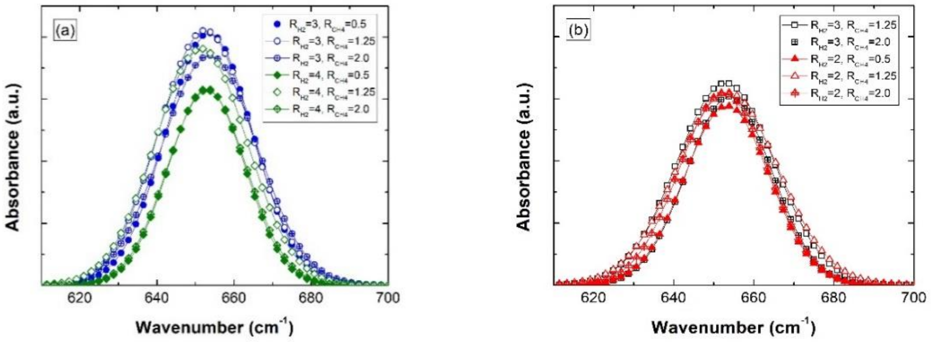

Figure 4. 26. FTIR spectrum for Si-H w/r mode centered at 650 cm^{-1} for the a-SiC_x:H deposited at (a) 80 $mWcm^{-2}$ and (b) 48 $mWcm^{-2}$.

The H (C_H) and C content (C_C) were calculated by numerical integration of the Si-H wagging/rocking [131] and Si-C stretching modes [132] centered at 640 cm^{-1} and 770 cm^{-1}, respectively. The C_H and C_C were determined using Eq. 4.1. In the equation, $\alpha(\nu)$ is the absorption coefficient of the film at wavenumber, $\nu_{r/w}$ stands for rocking/wagging bonds, A_w is the proportionality constant and N_{Si}=5x10^{22} cm^{-3} is the atomic density of pure silicon. A_w is assigned to 1.6x10^{19} cm^{-2} for hydrogen and 2.13x10^{19} cm^{-2} for carbon [131]. The C_H and C_C results are given in Fig. 4 for various deposition conditions.

Here, the lower deposition power leads to lower incorporation of C to the a-Si matrix instead of higher deposition powers. Also, the increase in R_{CH_4} and R_{H_2} caused a slight improvement in the C_C and C_H of the film for lower deposition power. However, when the deposition power was increased, C_C was enhanced significantly, with a minor variation in C_H. We detected an inverse relationship between C_H and C_C with the SiH_4 dilution ratio at the higher deposition power density based on the FTIR results. When the SiH_4 dilution increased, both C_H and C_C decreased remarkably in these comparisons. It should be noted that the highest C_H and C_C values are found as 4.2% and 1.6%, respectively. It is known that a higher amount of C_H in a-Si:H layers are needed to achieve high-quality passivation properties [133].

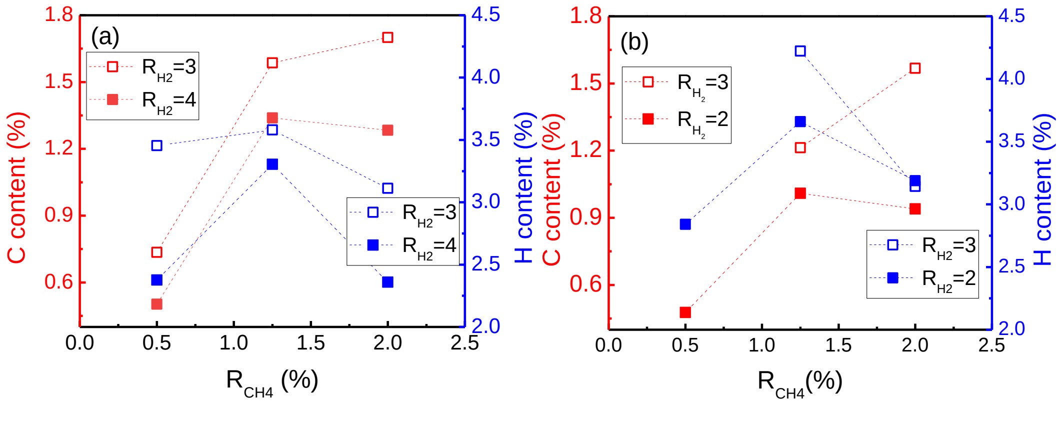

Figure 4. 27. Hydrogen and carbon content of a-SiC$_x$:H layers for (a) 80 mWcm^{-2} and (b) 48 mWcm^{-2} deposition power densities.

4.3.3.4 Analysis of the Interface Defects

In order to understand the passivation mechanism of a-SiC$_x$:H layer, C-V, and G-V measurements were taken at the frequency range of 100 kHz to 1 MHz using voltage between -1 V to +5 V in steps of 0.2 V for all samples. The series resistance corrected C-V and G-V characteristics of the a-SiC$_x$:H layer deposited R_{H_2}=3, R_{CH_4}=1.25 at the power density of 48mWcm^{-2} are given in Figure 4.28 (a) and (b), representing all the a-SiC$_x$:H layers. It should be noted that the measurement configuration of the impedance analyzer (HP 4192 LF) was set to parallel conductance and capacitance. Q_{fix} values were determined from the shift in the flat band voltage (V_{FB}), assuming that all the charges were located at the interface of c-Si. The effective Q_{fix} values were found to be negative and varying between 9.2×10^{10} and 7.8×10^{11} cm^{-2}, as listed in Table 4.8. The results pointed out that the fixed oxide charges in the a-SiC$_x$:H might not be sufficient, although the highest values we obtained were close to the generally accepted lower limit of 10^{12} cm^{-2} [134] necessary to create field-effect passivation. An increase in power density and methane flow might lead to an even higher amount of Q_{fix} in the a-SiC$_x$:H layers.

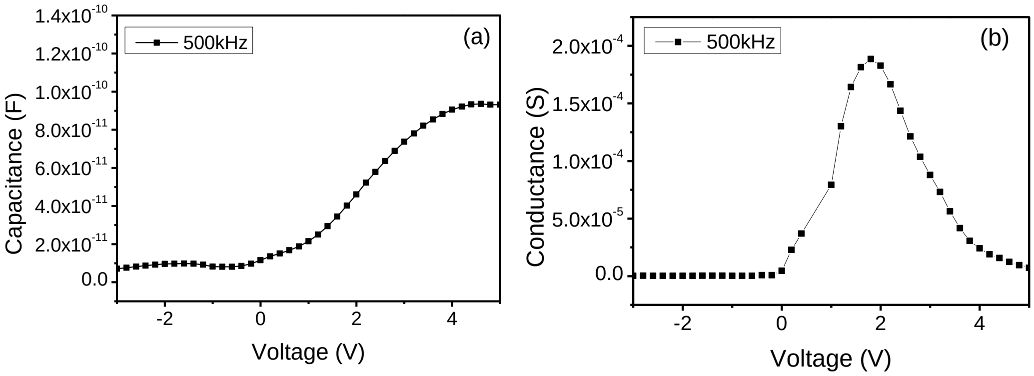

Figure 4. 28. C-V and G-V results of a-SiC$_x$:H layer deposited R_{H_2}=3, R_{CH_4}=1.25 at power density of 48 mWcm^{-2}.

The conductance method explained that the lowest and highest D_{it} values were 1.22×10^{12} and 5.61×10^{12} eV^{-1}cm^{-2}, respectively. The D_{it} values were slightly higher than the results reported by Choi et al. [135] and Rahman et al. [136]. The higher deposition power density led to an increase in D_{it} values. The general trend on higher power density was that an increase in the CH_4 flow rate results in an increment of D_{it} values. It should be noted that relatively low H content was found for the power density of 48 mW/cm^{-2} compared to 80 mW/cm^{-2}, increasing the number of dangling bonds. When the H_2 flow rate decreased, there was a slight rise in D_{it}. While the C_H of a-SiC_x:H increased, D_{it} values decreased, resulting in fewer dangling bonds at the interface consistent with our C_H values [135]. We have not observed any clear correlation between C_C and D_{it}. The lowest D_{it} was measured as 1.22×10^{12} eV^{-1}cm^{-2}, for minimum R_{CH_4} value and the higher deposition power.

Table 4. 8. Q_{fix} and D_{it} results of various a-SiC_x:H layers.

R_{H_2}	R_{CH_4}	**Power density (mWcm^{-2})**	**Q_{fix} (cm^{-2})**	**D_{it} (eV^{-1}cm^{-2})**
3	1.25	48	9.20×10^{10}	3.92×10^{12}
3	2.00	48	5.25×10^{11}	1.46×10^{12}
3	0.50	80	3.05×10^{11}	1.22×10^{12}
3	1.25	80	4.20×10^{11}	1.33×10^{12}
3	2.00	80	7.78×10^{11}	1.96×10^{12}
2	0.50	48	3.93×10^{11}	2.82×10^{12}
2	1.25	48	4.73×10^{11}	5.61×10^{12}
2	2.00	48	4.85×10^{11}	2.89×10^{12}
4	0.50	80	1.63×10^{11}	3.68×10^{12}
4	1.25	80	2.63×10^{11}	3.87×10^{12}
4	2.00	80	2.95×10^{11}	2.11×10^{12}

4.3.3.5 Elemental Analysis and Passivation Properties

The various deposition conditions form a different matrix of the atoms in the structure, becoming traceable by ToF-SIMS. In the following part, the correlation with the ratio of secondary ion intensity values of carbon to silicon (C^-/Si^- SI ratio) measured by ToF-SIMS and electrical and optical properties of a-SiC_x:H will be explained [126]. SI ratio in a ToF-SIMS measurement is defined as the ratio of the secondary ion intensity of the detected ion to one of the primary matrix elements or compositions in the ToF-SIMS spectrum:

$$SI\ Ratio = \frac{secondary\ ion\ intensity\ of\ spesific\ composition}{secondary\ ion\ intensity\ of\ main\ composition} \qquad \text{(Eq.4.4)}$$

The C^-/Si^- SI ratios were calculated using the ToF-SIMS depth profile measurements for different samples. The depth profile of the C^-/Si^- SI ratio versus sputter time is shown in Figure 4.29. The variation in total sputter time in different samples was due to the different thicknesses of the films. The mean value of each ratio was calculated from the value between 100 to 400 seconds of sputter time, where the composition was assumed to be homogenous.

The first striking feature seen in all depth profiles was the accumulation of the carbon atoms at the interface between a:SiC_x:H layers and c-Si substrates. The formation of this carbon-rich interface can be attributed to the formation of energy variations that depend on the C amount and surface energy. Comparing the results presented in Table 4.8 with the amount of C piled up at the interface, we found a strong correlation between the C concentration of the interface and D_{it} values calculated from the admittance measurements.

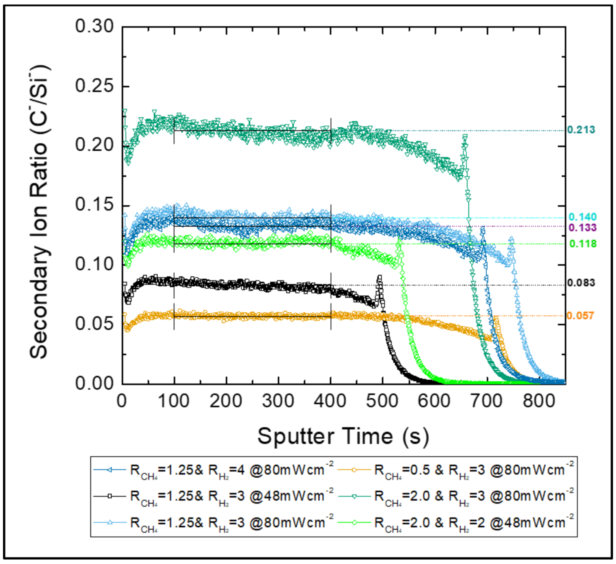

Figure 4. 29. The ratio of secondary ion intensity values of carbon to silicon represented for the samples with different fabrication parameters as ToF-SIMS depth profile data.

The variation of the band gap and corresponding resistivities with respect to the C-Si SI ratio are shown in Figure 4.30. As might be expected, the variation in resistivity of the SiC layer closely followed the variation of the optical band gap value. These results were in good agreement with values published by others [137].

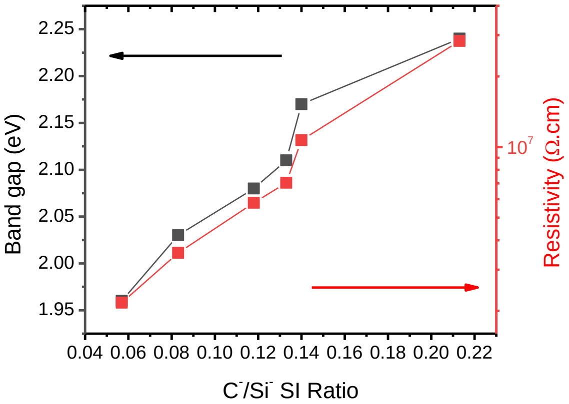

Figure 4. 30. Mean values of C^-/Si^- SI ratios calculated using ToF-SIMS depth profile data directly relate with the measured optical band gap and resistivity values.

ToF-SIMS technique is capable of identifying formations of different clusters such as SiC_2^-, SiC_3^-, and $Si_2C_2^-$. The intensity of the signal from these clusters can be normalized to the SiC^- intensity measured for the same layer. SiC^- ion originates from all the forms of clusters by various possible combinations of Si and C. Thus; the normalization allows us to compare the amount of these clusters in the layer. Figure 4.31 represents the comparison results for the SI ratio versus optical band gap values of different specific compositions. The graph showed a linear dependence of the optical band gap on various SI ratios [138] due to the higher amount of CH_4 molecules used during the deposition.

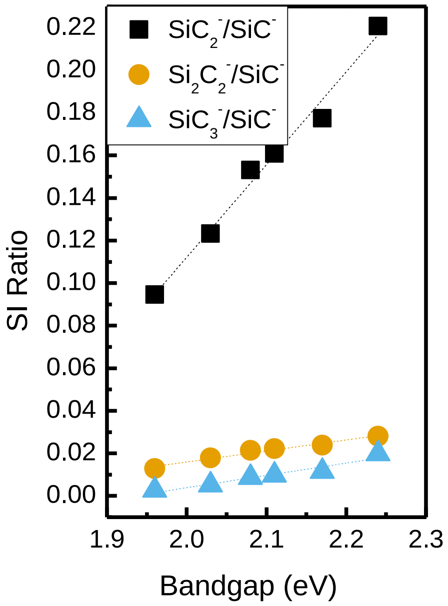

Figure 4. 31. Different corporations of C atoms with Si atoms in the matrix increase linearly with the optical band gap values as the mean SI ratio of the cluster combinations in a-SiC_x:H matrices.

The $SiCH^-/SiC^-$ SI ratio, shown in Figure 4.32 (a), indicates that the mean value of H bonding in the a-SiC_x:H structures are similar in almost all conditions. The sample deposited at $R_{H_2} = 3, \mathrm{R}_{\mathrm{CH}_4} = 0.5$ and 80 mWcm^{-2} power density presents the lowest CH_4 incorporation and thus the minimum amount of H in the layer [97]. As Boccard et al. discussed, the primary source of H is the CH_4 precursor in this structure [97].

In addition to the amount of H, the preferential behavior of H in the bonding structure changes, which plays a deterministic role in the electrical properties of the layer. Therefore, the CH-/SiH- ratio comparison explains the correlation between fixed charge density and chemical bonding preferences. The results indicate that increasing the intensity of the CH^-/SiH^- ratio also leads to an increase in Q_{fix}, which is related to the corporation of CH to a-Si matrix.

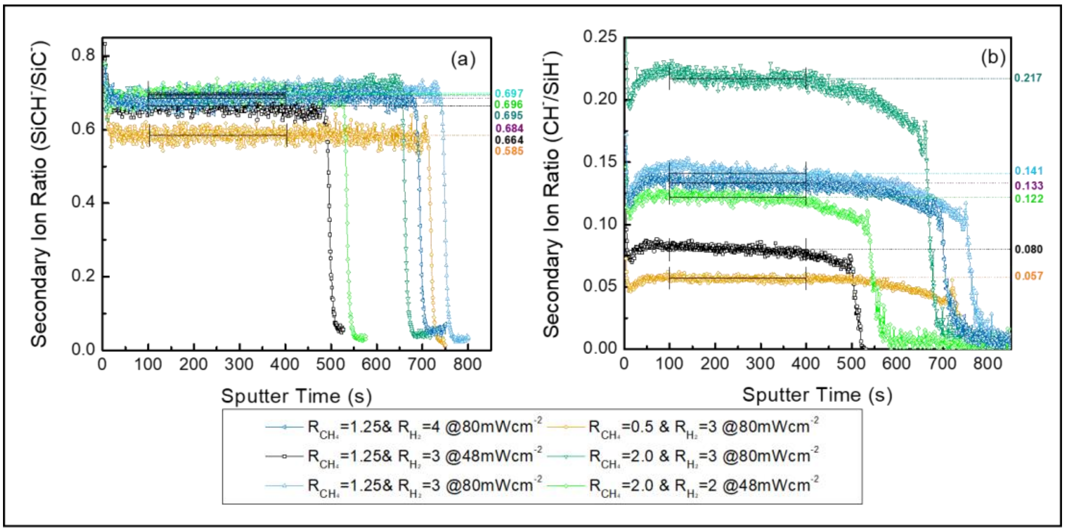

Figure 4. 32. The ratio of secondary ion intensities of (a) $SiCH^-/SiC^-$ and (b) CH^-/SiH^- represented for the samples with different fabrication parameters per ToF-SIMS depth profile data.

The importance of carbon atoms bonded to hydrogen atoms for the passivation property during hydrogen passivation should be discussed. The comparison of SI ratio between CH^- and SiH^- indicates the bonding preference of hydrogen ions to either Si or C atoms in the a-Si matrix under various deposition regimes (See Figure 4.32 (b)). Each Si or C atom could be placed in the structure with a higher amount of unattached defective bonds. Comparing samples deposited at 80 mWcm^{-2} power density and $R_{H_2} = 3$ under different values of R_{CH_4}, which was the primary source of hydrogen, shows an increase in the CH content and higher CH_4 flow. The comparison of power density reveals that the higher the power density of plasma dissociated, the higher amount of hydrogen attaching to the C atoms. Moreover, for the samples under fixed R_{CH_4} and plasma power density values, the rise in the R_{H_2} has not shown any significant change in the hydrogen bonding preference within the matrix.

The passivation quality of each layer was identified using the PCD method under symmetrically coated double-sided a-SiC_x:H, as given in Figure 4.33 (b). Here, the thickness of each a-SiC_x:H layer was 7 nm except stack layer passivation for a-Si:H and a-SiC_x:H. The deposition conditions were determined in accordance with our previous results, meaning relatively low D_{it} values and a low SI ratio of C^-/Si^-. The deposition power and R_{H_2} were fixed at 80 $mWcm^{-2}$ and 3, respectively. Additionally, the impact of $R_{\mathrm{CH_4}}$ on the passivation quality was clarified, and results are shown in Figure 4.32. Evaluations showed that the effective lifetime results decrease significantly due to the increase in the carbon content of the a-SiC_x:H layer and SI ratio of C^-/Si^-, resulting in higher mid-gap defect densities. The highest effective lifetime was measured as 45 µs at low carbon content films, and this value decreased with the increase in carbon content. Similar behavior of carbon-rich a-SiC_x:H layers were discussed concerning thicker layers by Boccard et al. [97]. Furthermore, an increase in the SI ratios of C^-/Si^-, $SiCH^-/SiC^-$ and CH^-/SiH^- correlated with the passivation quality of the a-SiC_x:H layer. Consequently, further improvement in the passivation quality of the a-SiC_x:H layer was achievable by improving interface defect densities and hydrogen content of the film.

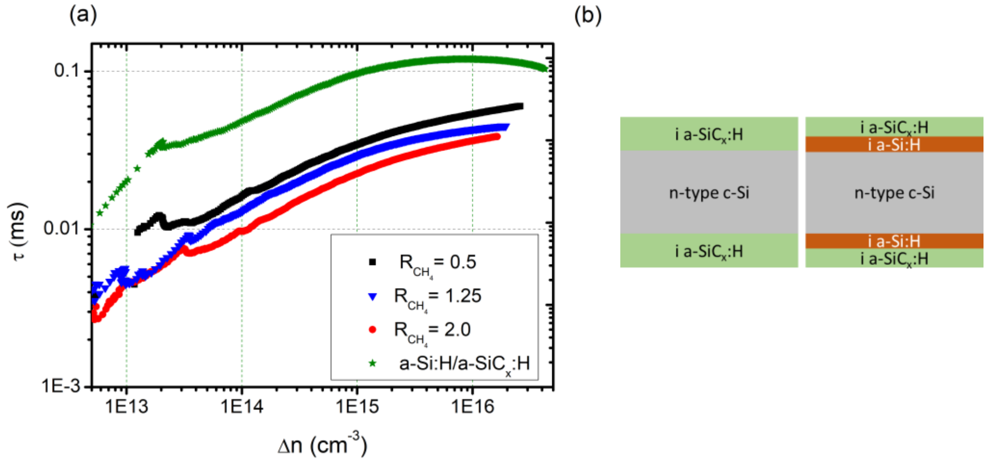

Figure 4. 33. (a) Effective lifetime results of a-SiC$_x$:H layers deposited at 80 mWcm^{-2} and R_{H_2} = 3 under various methane flow and stack layer passivation values, (b) cross-sectional view of the passivation structure.

Eventually, due to the higher amount of dangling bonds formation at the interface between a-SiC$_x$:H and c-Si, we introduced higher quality buffer layer of a-Si:H between a-SiC$_x$:H and c-Si to improve the interface quality. The thickness of a-Si:H and a-SiC$_x$:H layers are 3 nm and 4 nm, respectively. Due to eliminating a highly recombinative interface with an ultra-thin a-Si:H layer, the passivation quality was improved up to 100 µs, resulting in $_{imp}V_{oc}$ of 650 mV.

4.4 Conclusions

In conclusion, the relationship between passivation quality of a-Si:H layer and film properties in terms of "H" content and D_{it} were studied as a function of deposition conditions. Higher SiH_4/H_2 ratio led to the better quality of passivation with a-Si:H. Post-deposition HPT of the (i) a-Si:H layer further improved passivation quality by decreasing dangling bonds within the film and at the film-wafer interface. HPT allowed D_{it} to decreased up to 7.62x10^{10} eV^{-1}cm^{-2}. Moreover, the best quality passivation occurred at 9.45% "H" content, resulting in 740 mV $_{imp}$Voc. Subsequently, an unexpected decrease in the passivation quality of (i) a-Si:H led us to focus on possible sources of this decrease. Firstly, the effect of the deposition holder, tweezers, and the showerhead was investigated. In accordance with the results, the contaminants from tweezers were blocked, the scratch problem caused by the deposition holder was improved, and thermal tape usage was stopped. Secondly, possible contaminants from wet chemical processes were traced. It was observed that metallic contaminants coming from wet chemical processes have a significant impact on passivation. The contamination doses were traced by ToF-SIMS measurements. The corrosion in the stainless steel parts of the wet benches had influenced passivation with both SiO_2 and (i) a-Si:H layers. At this stage, different kinds of beakers, made of PVDF and PFA, were compared in terms of contamination during the RCA cleaning processes. Next, the contamination problem was solved by new and clean quartz beakers resulting in (i) a-Si:H passivation quality with ${}_{imp}V_{OC}$ values over 710 mV.

The optical band gap of a-SiC_x:H is improved up to 2.24 eV to decrease a-Si:H's parasitic absorption for SHJ solar applications. Due to the necessity of higher energy to decompose CH_4 molecules into radicals, the rise in power density increases E_g values. We found that R_{H_2} and power density plays a deciding role in the decomposition of CH_4 molecules. Observations showed that the H content of a-SiC_x:H layers were lower than 5%, and the C content varied between 0.5% to 2% depending on deposition conditions. C content could be tuned and increased with deposition power. The interface quality was analyzed by conductance method, and the D_{it} values were between $1.2x10^{12}$ and $5.6x10^{12}$ $eV^{-1}cm^{-2}$ for the interface of c-Si and a-SiC_x:H. Relatively high D_{it} values were measured with a-SiC_x:H layers under various deposition conditions. We identified the ratio between C and Si atoms encountered in the a-SiC_x:H formation as the tuning mechanism of the optical band gap and resistivity values. The preference between hydrogen bonding to the silicon or carbon atoms related to the deposition regime was noted, and the fixed charge density of the a-SiC_x:H layer correlated with the corporation of CH to the matrix. Moreover, SI ratios of C^-/Si^-, $SiCH^-/SiC^-$ and CH^-/SiH^- had a significant impact on the interface in terms of passivation quality where these ratios should be decreased to achieve higher passivation quality. We found that relatively low passivation qualities were achieved when the a-SiC_x:H layer was coated. Interface quality improved due to a buffer a-Si:H (3 nm) layer inserted between c-Si and a-SiC_x:H layers, and we managed to achieve an effective lifetime value of 100 μs which resulted in an ${}_{imp}V_{oc}$ value of 650 mV.

CHAPTER 5

PROPERTIES OF ELECTRON AND HOLE SELECTIVE CONTACTS

5.1 Introduction

Material properties of heterocontacts directly influence the device performance of SHJ solar cells. On the front side of an SHJ solar cell with an n-type Si substrate, the doping density of (p) a-Si:H emitter layer has a deterministic role in building a sufficient electric field at the junction [139]. Moreover, the contact properties between (p) a-Si:H and ITO layer is one of the sources of series resistance losses due to the relatively high contact resistivity [140]. Ideally, the emitter side material of the solar cell should have a wide band gap since this would improve the device response on shorter wavelength region. However, the band gap of (p) a-Si:H layer is less than 1.7 eV, which may cause some loss in the UV region [141]. One material option with a wide band gap is (p) a-SiC$_x$:H layer since its band gap could reach 2.4 eV [115]. For the rear side of SHJ solar cells, the doping density of (n) a-Si:H is crucial for decreasing contact and layer resistivities. However, due to the self-inhibiting nature of a-Si known as the autocompensation model [23], the maximum doping is limited for both n- and p-type doping, and increasing doping density over the limit would cause an increase in the defect density [142].

In recent years, most research groups have started to focus on the usage of metal oxides [143], [144], fluorides [145], [146], and other materials [147], [148] as a carrier-selective contact for SHJ solar cells instead of doped a-Si:H layers. The main advantages of the usage of carrier-selective materials are the low-temperature and straightforward processes and the materials' tailored optical characteristics. The asymmetric heterocontact concept referred to as dopant-free asymmetric heterocontact (DASH) was introduced by Bullock et al. They have shown promising efficiency values as high as 19.4% [145].

This chapter will analyze the optical and electrical properties of doped a-Si:H, wide band gap emitter layers (p-type a-SiC$_x$:H and MoO$_x$), and electron selective contact (LiF$_x$). Moreover, stack layer passivation properties of these layers with (i) a-Si:H will be discussed.

5.2 Experimental

In this study, two different substrates were used for emitter and BSF material depositions. The first was DSP, CZ, 1-3 ohm.cm, n-type Si wafers with 275 µm thickness, and the second was borosilicate glass substrates. The wafers were cleaned by using standard RCA-2 and piranha solutions, followed by oxide removal using HF:HCl:H$_2$O (1:1:10) after each of these cleaning steps. After the oxide removal step, wafers were rinsed with DIW, and cleaned wafers were later loaded to GünEr PECVD cluster system for deposition of doped a-Si:H layers. Process flow for the preparation of samples can be found in Figure 5.1. A similar process flow was applied on the same substrates for MoO$_x$ and LiF$_x$ via the thermal evaporation technique.

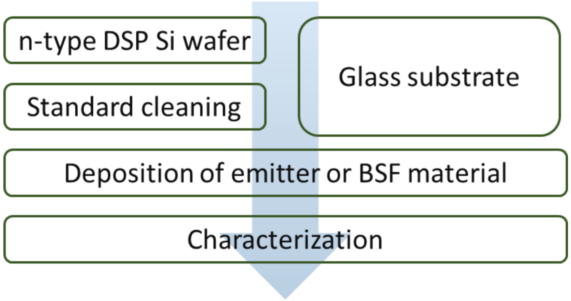

Figure 5. 1. Experimental flow chart for the preparation of doped a-Si:H layers.

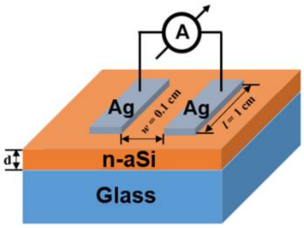

Figure 5. 2. Cross-sectional view of the sample prepared for I-V characterization.

The doped layers were grown under various hydrogen dilution and doping ratio values. The resistivities of the doped layer were characterized by I-V measurements on the sample structures revealed in Figure 5.2. The thickness of Ag contacts grown using the thermal evaporation technique was around 300 nm. The thickness of each layer was measured by spectroscopic ellipsometry (Semilab) using the Tauc-Lorentz model [97]. The Tauc-plot extrapolation was used to calculate the optical band gap of layers, obtained from the absorption spectra measurements performed by UV-Vis-NIR spectrometer (Bentham PVE 300). Moreover, the activation energy of doped a-Si:H was calculated via temperature-dependent I-V measurement. The doping concentration of a-Si:H layers grown on c-Si wafers was determined through the electrochemical C-V (ECV) technique [149]. Stack layer passivation properties of materials, with and without (i) a-Si:H, were identified by effective lifetime measurements (Sinton).

5.2.1 Results and Discussions

5.2.1.1 Properties of Phosphorus Doped a-Si:H Layer

Impact of hydrogen dilution ratio (R_{H_2}) and doping ratio of phosphorus (R_{PH_3}) on the properties of (n) a-Si:H layer were investigated. The doping ratio is the ratio between PH_3 to SiH_4 gasses flow during the deposition. The deposition duration was fixed to 10 minutes except for doping ratios of 0.04 and 0.02, and R_{H_2} value of 3, where the deposition duration was 5 minutes due to the high deposition rate. The optical band gap and thickness of the (n) a-Si:H layer are listed in Table 5.1. Due to the mass flow control unit and scrubber limits, the higher doping ratios could not be performed. The increase in the doping ratio led to a decrease in E_g and deposition rate. For higher R_{H_2} values, the deposition rate decreased significantly due to the ionization of a higher amount of hydrogen molecules during the plasma operation [105]. The largest E_g value was found as 1.84 eV, which is obtained with R_{PH_3} values equal to 0.008 and 0.010, which correlates well with the literature on this subject [150]. Moreover, the highest deposition rate was achieved at lower doping and hydrogen dilution ratios. Doping concentration determines not only the optical properties but also the conductivity of the a-Si film. The electrical properties of the film are crucial to form an effective electrical field at the rear side and make electrons get collected at the rear side of the structure which affects the collection efficiency for electrons. The conductivity results for both in the dark and under 1 Sun illumination are illustrated in Figure 5.3 for various doping and hydrogen dilution ratios. The active doping of a-Si:H layers decreased sinificantly for lower R_{H_2} values, causing a drop in conductivity for both in the dark and under illumination conditions. Except for hydrogen dilution value of 9, an increment in doping ratio led to a decrease in conductivity, which is inconsistent with the data in the literature [105]. However, for the samples prepared with a hydrogen dilution ratio of 9, an increase in the doping ratio led to an improvement in the conductivity values up to a specific ratio (0.04) before starting to decrease. In general, the conductivity difference observed between dark and under illumination was insufficient; there should have been an increase in conductivity for an order of magnitude under 1 Sun illumination [105]. The conductivity difference was less than one order of magnitude in our results except for only one deposition condition.

Table 5. 1. The optical band gap values and thickness of layers.

R_{H_2} R_{PH_3}	9		5		3	
	E_g (eV)	t (nm)	E_g (eV)	t (nm)	E_g (eV)	t (nm)
0.008	1.78	56	1.84	57	1.73	97
0.010	1.78	47	1.84	76	1.74	92
0.020	1.74	45	1.77	81	1.77	36
0.040	1.74	43	1.76	63	1.77	31
0.060	1.68	41	NA	NA	NA	NA

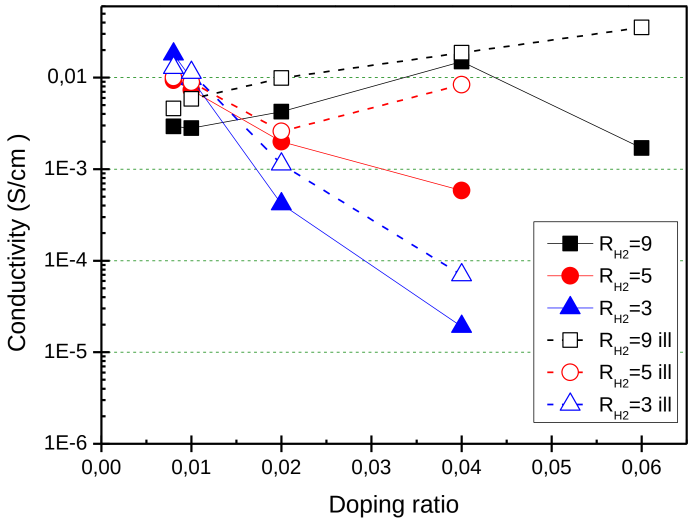

Figure 5. 3. Dark and illuminated conductivity vs. doping ratio plots for (n) a-Si:H thin-films deposited with different R_{H_2} values.

The conductivity results revealed that a hydrogen dilution value of 9 and a doping ratio of 0.04 provided the optimum deposition conditions. Next, active doping concentration was determined via ECV measurement, as shown in Figure 5.4. The peak doping concentration measured was 9.8×10^{19} cm^{-3}. Moreover, there was a variation on the doping profile related to changes in heat distribution for depositions longer than 5 minutes.

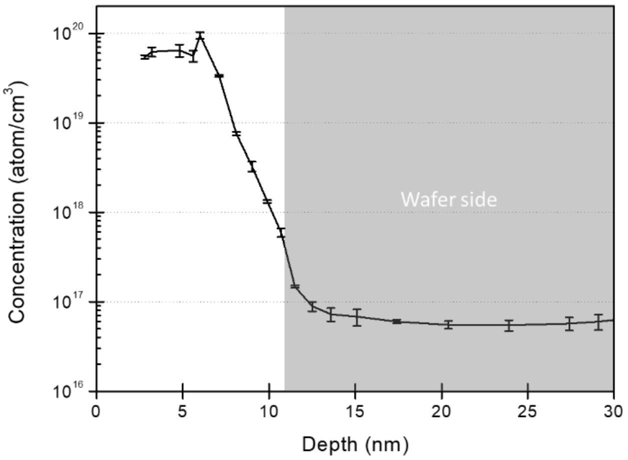

Figure 5. 4. Depth profile of doping concentration obtained from ECV measurements of (n) a-Si:H layer grown on the n-type c-Si wafer.

The optimum deposition conditions for (i) a-Si:H and (n) a-Si:H were applied during passivation of the samples with 7 and 12 nm thicknesses, respectively. The impact of (n) a-Si:H layer on the passivation quality was investigated via PCD and PL measurements, and $_{imp}V_{OC}$, effective lifetime are listed in Table 5.2. PL images showed some mechanically damaged areas due to the transfer period of (i) a-Si:H passivated sample in the PECVD cluster system, as discussed in the previous chapter. Even though some of the damaged and dead passivated sample parts decreased effective lifetime locally, there was almost no change in the average passivation properties after deposition of (n) a-Si:H layer.

Table 5. 2. The effective lifetime and $_{imp}V_{OC}$ results for (i) a-Si:H and (i/n) a-Si:H stack layer.

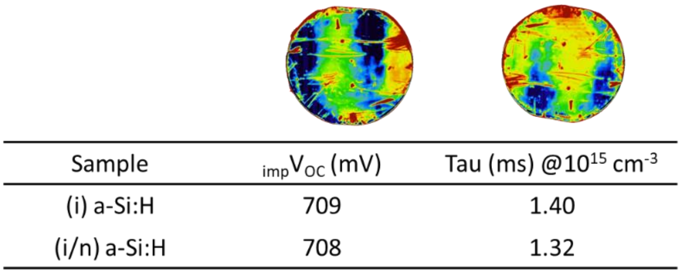

Sample	$_{imp}V_{OC}$ (mV)	Tau (ms) @10^{15} cm^{-3}
(i) a-Si:H	709	1.40
(i/n) a-Si:H	708	1.32

5.2.1.2 Properties of Boron Doped a-Si:H Layer

Impact of R_{H_2} and $R_{B_2H_6}$ values on the properties of (p) a-Si:H thin-film were investigated in terms of E_g and conductivity. The deposition duration was set to 7 minutes for all depositions. The optical band gap and thickness measurements of (p) a-Si:H layer were recorded in Table 5.3. Due to the relatively low conductivity values (less than $1x10^{-6}$ S/cm) of (p) a-Si:H layer deposited with the hydrogen dilution ratio of 3, the optical band gap and conductivity results were left out.

The increase in the doping ratio led to a decrease in E_g and an increase in the deposition rate of (p) a-Si:H layer. The largest E_g measured was 1.68 eV for $R_{B_2H_6}$ value of 0.008, a value similar to the ones reported in the literature [150]. Moreover, the highest deposition rate was observed at lower doping and hydrogen dilution ratios.

Table 5. 3. The optical band gap values and thicknesses of (p) a-Si:H layers.

R_{H_2} / $R_{B_2H_6}$	9		5	
	E_g (eV)	t (nm)	E_g (eV)	t (nm)
0.008	1.68	65	1.67	52
0.010	1.67	89	1.67	62
0.020	1.64	90	1.66	67
0.040	1.64	92	1.64	79
0.060	1.64	113	1.64	91

In addition to the optical properties of (p) a-Si:H layer, the electrical properties are crucial to form an electrical field on the front and collect holes on the front side. The conductivity results for both in the dark and under 1 Sun illumination are illustrated in Figure 5.5 for various doping and hydrogen dilution ratios. The conductivity of (p) a-Si:H layers increased for lower R_{H_2} values for both in the dark and under illumination conditions. The increase in the hydrogen dilution ratio improved the conductivity of layers. However, even the highest value of conductivity is low when compared to the reported values in the literature. The difference between the dark and 1 sun illuminated conductivity values is less than one order of magnitude [105]. The optimum deposition condition was noted as hydrogen dilution value of 9 and doping ratio of 0.01, resulting in conductivity of 2.17x10^{-4} S/cm.

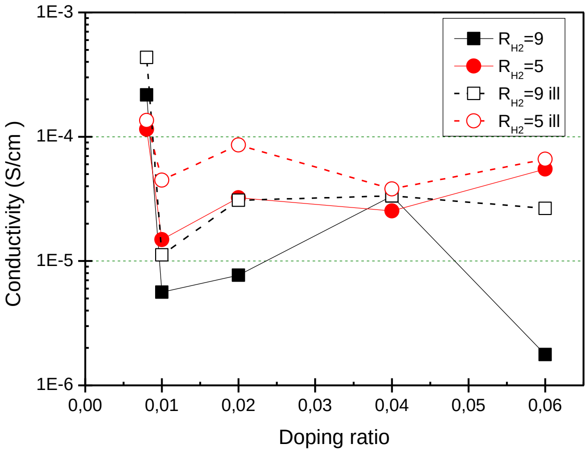

Figure 5. 5. Dark and illuminated conductivity vs. doping ratio plots for (p) a-Si:H thin-films deposited with different R_{H_2} values.

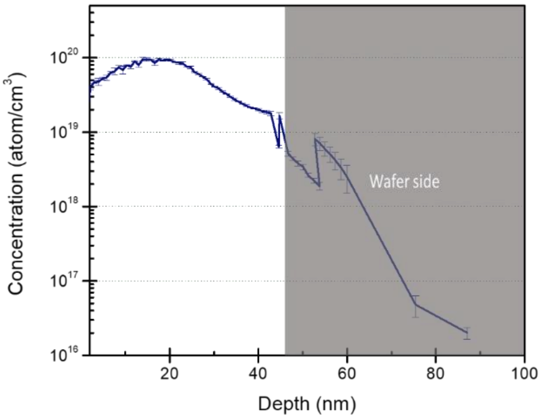

Figure 5. 6. Depth profile of doping concentration obtained from ECV measurements of (p) a-Si:H layer grown on top of an n-type c-Si wafer

Later, active doping concentration was determined by ECV measurement, as shown in Figure 5.6. The peak value of the doping concentration observed was 9.8x10^{20} cm^{-3}. Moreover, a slight variation on the doping profile was detected, related to a variation in heat distribution for longer depositions.

Table 5. 4. The effective lifetime and $_{imp}V_{OC}$ results for (i) a-Si:H and (i/p) a-Si:H stack layer.

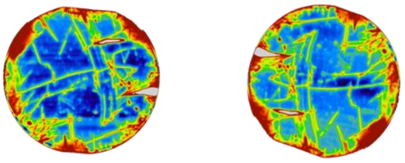

Sample	$_{imp}V_{OC}$ (mV)	Tau (ms) @10^{15} cm^{-3}
(i) a-Si:H	708	1.31
(i/p) a-Si:H	706	1.27

The optimum deposition conditions for (i) a-Si:H and (p) a-Si:H were applied during passivation samples with 7 and 12 nm thicknesses, respectively. The impact of (p) a-Si:H layer on the passivation quality was explored via PCD and PL measurements, and the effective lifetime and $_{imp}V_{OC}$ results are listed in Table 5.4. A slight decrease in the effective lifetime results could be explained by the measurement uncertainty. Therefore, it can be concluded that doped a-Si:H depositions do not have to influence passivation properties.

5.2.1.3 Wide Band Gap Emitters

Mainly two promising materials were characterized and integrated into SHJ solar cells: (p) a-SiC$_x$:H and MoO$_x$ layers. A relatively wide range of band gap values is achievable by increasing C incorporation into the a-Si:H matrix for (p) a-SiC$_x$:H layers. During the optimization of (p) a-SiC$_x$:H layers, methane flow rate, doping ratio, and RF power were examined in terms of optical and electrical properties via I-V, cryogenic I-V, ellipsometry, and transmission measurements [151]. The conductivity and E_g values for the (p) a-SiC$_x$:H layers obtained with hydrogen dilution ratio of 9, doping ratio of 0.035, and various deposition powers and methane flows (10, 20, and 30 sccm) are given in Figure 5.7. The narrowest and largest E_g values are determined as 1.6 eV and 2.0 eV, respectively, where the (p) a-Si:H had an E_g value of 1.6 eV as discussed previous part. As discussed in the previous chapter, for lower CH_4 flow and lower plasma power densities, the incorporation of carbon is significantly poor compared to silicon radicals. For that reason, higher CH_4 flow and power density are required for an efficient C incorporation in a-Si matrix. The resistivity values of (p) a-SiC_x:H layers were relatively higher than (p) a-Si:H layers. Moreover, an increase in power density led to a decrease in layer conductivity and a higher amount of C incorporation in the a-Si:H matrix [151]. The inverse relationship between E_g and conductivity was recorded; as the layer conductivity increased, E_g values decreased.

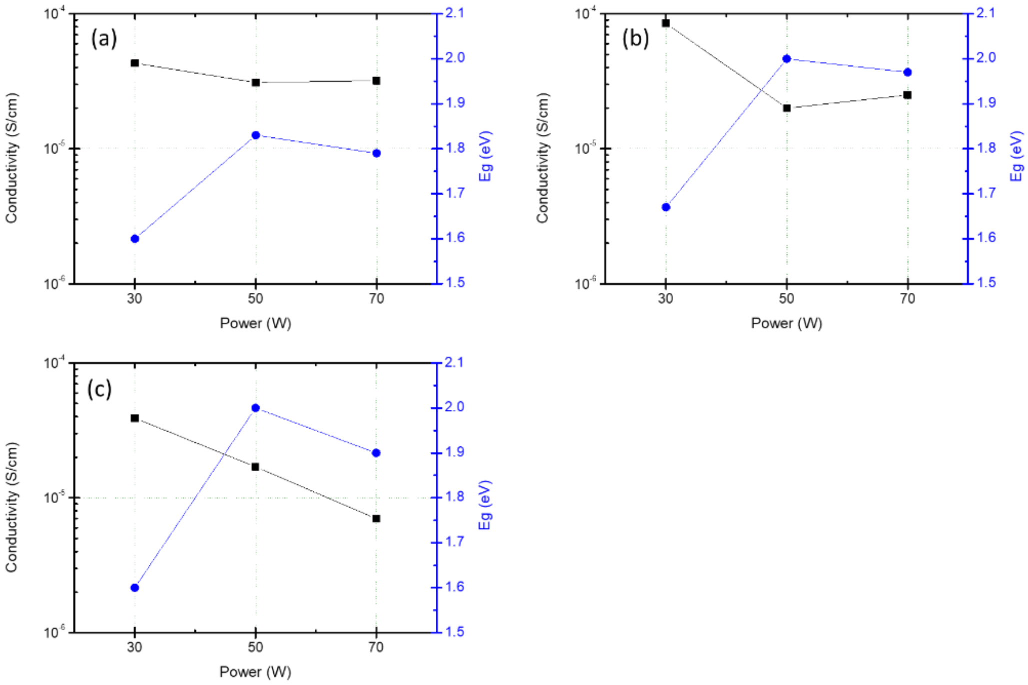

Figure 5. 7. The band gap and conductivity results of (p) a-SiC_x:H layers grown with methane flow of (a) 10, (b) 20, and (c) 30 sccm with various deposition powers.

The conductivity of the best performing layer in terms of electrical properties was recorded as $9x10^{-4}$ S/cm with the dopant activation energy of 0.33 eV. The selected best performing two (p) a-SiC_x:H layers with band gap energy values of 1.9 and 2.0

eV were integrated into SHJ solar cell fabrication. The deposition parameters were selected with respect to simulation results discussed in Chapter 2.

Another promising wide band gap material used as hole selective contact (HSC) is the MoO_x layer. The optical, interface and passivation properties of MoO_x were characterized by ellipsometry, C-V, and effective lifetime measurements. The MoO_x layer thermally grown on top of the n-type Si wafer was analyzed by C-V measurements on the dot metal contact structure previously explained, and interface trap density was calculated via the conductance method. The built-in voltage (Φ_{bi}) and D_{it} results were given in Table 5.5. It was found that D_{it} values were significantly high when we compared with (i) a-Si:H layer, which indicates that without the usage of any passivation layer such as (i) a-Si:H and SiO_2 layers between MoO_x and c-Si wafer, it is not possible to achieve high-quality chemical passivation only with MoO_x layer.

Table 5. 5. Calculated values of Φ_{bi} and D_{it} from C-V measurements.

Sample	Φ_{bi} (V)	D_{it} (x10^{12} $eV^{-1}cm^{-2}$)
MoO_x	0.24	8.35 - 12.33

The spectroscopic ellipsometry measurements were modeled by Cauchy with Urbach tail [152]. The band gap value was found as 3.32 eV for thermally grown 15.88 nm MoO_x layer as given in Figure 5.6. Furthermore, the refractive index and extinction coefficient at 632.8 nm were modeled as 1.83 and 0.0091, respectively. Due to the relatively high band gap and low extinction coefficient, MoO_x material has a promising choice as a window layer.

Table 5. 6. Modeled spectroscopic ellipsometry result of MoO_x.

Sample	d (nm)	E_g (eV)	n @632.8 nm	k @632.8 nm
MoO_x	15.88	3.32	1.83	0.0091

The textured CZ n-type Si wafers with a resistivity of 2 Ω.cm were used. Passivation properties of MoO_x with and without (i) a-Si:H layers were analyzed under the various thickness of (i) a-Si:H layers. The thickness of MoO_x was fixed to 12 nm through the passivation study. Three thicknesses of (i) a-Si:H layer (3 nm, 5 nm, and 7 nm) were prepared with MoO_x to identify stack layer passivation properties. In Figure 5.8, the effective lifetime results and cross-sectional view of passivation samples are given. Without any interfacial (i) a-Si:H layer, the effective lifetime of only MoO_x was below 300 μs. The sample with 3 nm (i) a-Si:H showed an effective lifetime of 100 μs which is not sufficient for SHJ applications. After MoO_x growth on top of 3nm (i) a-Si:H, the effective lifetime values changed slightly and the resulted ${}_{imp}V_{OC}$ of 620 mV. The passivation quality of (i) a-Si:H layer was improved with 5 nm thick layer compared to 3 nm resulting in τ of 0.6 ms and ${}_{imp}V_{OC}$ of 686 mV. After deposition of MoO_x, the passivation quality was improved slightly, resulting in τ of 0.8 ms and ${}_{imp}V_{OC}$ of 693 mV. The highest passivation quality was achieved by deposition of 7 nm (i) a-Si:H layer resulting in τ of 1.2 ms and ${}_{imp}V_{OC}$ of 711 mV. When the MoO_x layer was deposited on top of (i) a-Si:H layer, there was a slight decrease in passivation quality, which had τ of 1.1 ms and ${}_{imp}V_{OC}$ of 700 mV. The results indicated that the stack layer passivation of (i) a-Si:H/MoO_x is a promising combination for the usage of a wide band gap emitter in the SHJ solar cell structure.

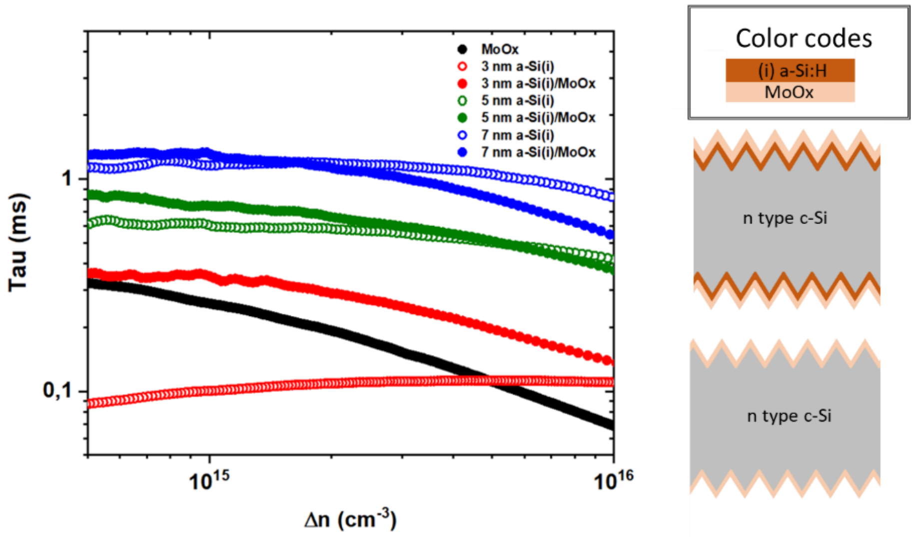

Figure 5. 8. Effective lifetime vs. excess carrier density results of MoO_x and (i) a-Si:H/MoO_x stack layers passivated with various thicknesses of (i) a-Si:H.

5.2.1.4 Electron Selective Contact

On the rear side of SHJ solar cells, LiF_x/Al stack layer was applied as an electron selective contact structure. LiF_x/Al stack layer was deposited by thermal evaporation technique without breaking the vacuum with thicknesses of 1 and 300 nm, respectively. The spectroscopic ellipsometry result was modeled using Tauc-Lorentz, and the results are presented in Table 5.7. The band gap of LiF_x was almost 13 eV for the thickness of 9 nm resulting in a refractive index of 1.38 at 632.8 nm wavelength. The sample was used for thickness calibration before resuming the passivation sample preparation, and the deposition rate was calculated as 0.1 Å/s.

Table 5. 7. Modeled spectroscopic ellipsometry result of LiF_x.

Sample	**d (nm)**	**E_g (eV)**	**n @ 632.8 nm**
LiF_x	8.98	12.99	1.38

The thickness of LiF$_x$ was fixed to 1 nm for the passivation study, and (i) a-Si:H layers with three different thicknesses (3 nm, 5 nm, and 7 nm) were prepared with and without LiF$_x$ stack layers. The effective lifetime results are provided in Figure 5.9. The LiF$_x$ layer with the thickness of 1 nm without any interfacial layer did not exhibit any passivation properties. After the growth of the LiF$_x$ layer, the passivation qualities decreased for all samples with different (i) a-Si:H thickness values. It was found that 7 nm (i) a-Si:H yielded effective lifetime and $_{imp}V_{OC}$ values as τ_{eff} =0.9 ms and $_{imp}V_{OC}$ = 710 mV. After LiF$_x$ coating on top of the 7 nm (i) a-Si:H, τ_{eff} dropped to 0.7 ms, and $_{imp}V_{OC}$ to 698 mV. The passivation quality of 5 nm (i) a-Si:H was noted as τ_{eff} of 0.7 ms and $_{imp}V_{OC}$ of 696 mV. After LiF$_x$ coating, τ_{eff} decreased to 0.5 ms, and $_{imp}V_{OC}$ to 686 mV. Similar behavior was observed during stack layer passivation of 3 nm thick (i) a-Si:H and LiF$_x$. It was concluded that LiF$_x$ itself does not present any passivation properties on c-Si wafers. The optimum (i) a-Si:H thickness for the application of electron selective contact was determined as 7 nm.

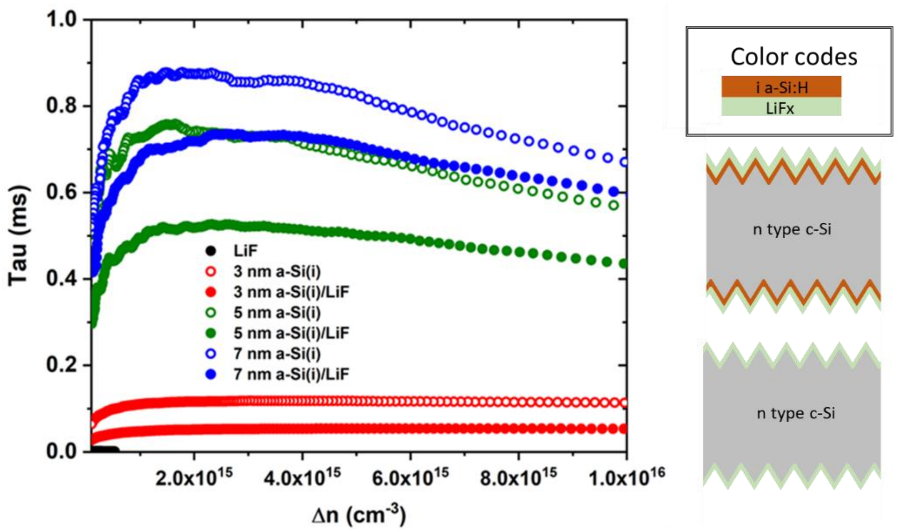

Figure 5. 9. Effective lifetime vs. excess carrier density results of LiF$_x$ and (i) a-Si:H/LiF$_x$ stack layer passivation for various (i) a-Si:H thicknesses.

5.3 Conclusions

This chapter investigated the impact of doping and hydrogen dilution ratios on the electrical and optical properties of doped a-Si:H layers. Results showed that the conductivity difference was less than one order of magnitude for both phosphorous and boron-doped a-Si:H layers. From the conductivity results of (n) a-Si:H, the optimum deposition conditions for hydrogen dilution and doping ratio were determined to be 9 and 0.04, respectively. The peak value of the doping concentration was found to be 9.8x10^{19} atoms/cm^3. For (p) a-Si:H layer, the increase in the doping ratio led to a decrease in E_g, where we noted the largest E_g as 1.68 eV obtained by $R_{B_2H_6}$ equal to 0.008. At the end of the analyses, observations found that the optimum hydrogen dilution and doping ratio was 9 and 0.01, respectively, resulting in conductivity of 2.17x10^{-4} S/cm. For both n and p-type doped a-Si:H layer, we found that the doped a-Si:H layer has no direct impact on the passivation quality.

The wide band gap materials, (p) a-SiC_x:H and MoO_x, were optimized and analyzed in terms of their optical and electrical properties. The band gap of the emitter layer expanded up to 2.3 eV by making use of C incorporation in the a-Si:H matrix resulting in relatively resistive (p) a-SiC_x:H layers. Furthermore, the interface properties of MoO_x with c-Si wafer were clarified, and stack layer passivation properties were examined. It was noted that the optimum thickness of (i) a-Si:H layer is 7 nm for the stack layer passivation with MoO_x. The properties of LiF_x as an ESC were investigated, having a band gap of 13 eV. The observations revealed that the LiF_x layer does not have passivation properties. It was possible to enhance passivation properties with the stack layer after inserting the (i) a-Si:H into the structure.

CHAPTER 6

FABRICATION AND PERFORMANCE OF SILICON HETEROJUNCTION SOLAR CELLS WITH AND WITHOUT WIDE BAND GAP EMITTER

6.1 Introduction

The conversion efficiency of c-Si solar cells has been continuously increasing owing to the improvements in optical and electrical properties of layers. Recently, several research groups and companies have announced solar cell efficiencies exceeding 25% in SHJ structure [153]–[155]. Huasun announced the new record efficiency for SHJ solar cells with a conversion efficiency of 25.26% [153]. The success of SHJ solar cells is mainly related to the superior passivation quality of the thin hydrogenated amorphous silicon (a-Si:H) layers [87].

The transparent conductive oxide (TCO) materials as contact layer plays a vital role in the solar cell's final electrical and optical performance [156]. Its optical and electrical properties need to be optimized for an efficient solar cell operation. Reducing parasitic absorption in the near-infrared region of the solar spectrum is crucial for decreasing current losses, mainly related to the TCO layer's higher free carrier density. The amount of free carrier density of the TCO layer should be minimized while reserving the high conductivity, which is necessary for an efficient carrier collection. Moreover, achieving low resistivity with high transparency and mobility is essential for a high-quality TCO layer. Fill Factor (FF) values over 80%, and J_{SC} values over 40 mA/cm^2 have been achieved with the SHJ cells, as the TCO layer had high mobility and low resistivity [157]. Unlike the diffused junction c-Si solar cells, the TCO layer is obligatory for heterojunction structures for enhancing the lateral carrier transport. This layer increases the lateral conductivity between metal fingers and serves as the anti-reflective coating on the solar cell's surface [158]. Many research groups use various kinds of transparent conducting oxides (TCOs) in

SHJ solar cell structures [159]. Due to its superior electrical and optical properties, ITO has been the most investigated material for SHJ solar cells among the other TCO layers. The most common technique for ITO deposition is sputtering, whose deposition conditions determine the film properties [160]. To improve SHJ solar cell conversion efficiency, minimizing the electrical and optical losses from the TCO layer is necessary. Reactive sputtering is one of the methods used for reducing TCO-related losses.

This chapter will compare AZO and ITO in terms of SHJ solar cell performance and discuss how the oxygen partial pressure affects the ITO layers and SHJ solar cell efficiency. Furthermore, the relation between thicknesses of doped a-Si:H layers and solar cell efficiency, application of wide band gap material to SHJ solar cells, and fabrication of selective-contact solar cells will be discussed.

6.2 Experimental

Bifacial and monofacial SHJ solar cells were fabricated onto textured n-type CZ (100) wafers with 1-3Ω.cm resistivity, and 180 μm thickness. Figure 6.1 illustrates the cross-sectional views of SHJ solar cells.

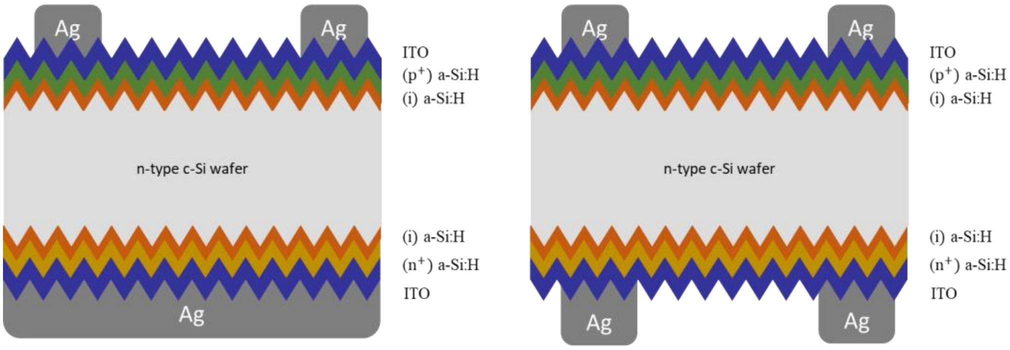

Figure 6. 1. Schematic configuration of monofacial and bifacial SHJ solar cell structure.

The wafers were textured in alkaline solution and then cleaned using RCA-2 and RCA-1 solutions. The grown oxide layer was removed with HF:HCl:H_2O (1:1:10) solution for 2 minutes. Depositions of a-Si:H and ITO layers were performed using the GünEr PECVD cluster system and Sputtering unit. The thickness of (i) a-Si:H was 7 nm on both the front and rear sides, while the thickness of the n and p doped a-Si:H layers varied between 10 to 12 nm. Furthermore, two different thickness and deposition parameters were used to form the wide band gap (p) a-SiC_x:H layers. Deposition parameters of a-Si:H layers are listed in Table 6.1. For the heterocontact solar cell design, the hole selective contact, MoO_x, and the electron selective contact, LiF_x/Al stack layers were formed by the thermal evaporation technique instead of doped a-Si:H layers. AZO and ITO layers were adopted as TCO layers for SHJ solar cells. The thickness of the TCO layer was fixed as 75 nm on the front and rear side. Moreover, specific contact resistivity between ITO and screen-printed Ag contacts was measured using the Transfer Length Method (TLM) [161]. The specific contact resistivity between c-Si/a-Si:H/ITO layers were identified via the spreading resistance modeling (4PP) method and TLM [162].

Table 6. 1. Deposition parameters of a-Si:H layers used in the SHJ solar cell fabrication.

	SiH_4(sccm)	**H_2(sccm)**	**PH_3(sccm)**	**B_2H_6(sccm)**	**T (°C)**
i a-Si:H	40	120	-	-	200
n a-Si:H	13	125	25	-	200
p a-Si:H	13	190	-	34	175

Industrial H-grid patterns with 5 busbars, 99 fingers with 35 μm finger opening were screen-printed on both sides of the cells using industrial low-temperature Ag-paste for the full-size solar cells (see Appendix B). Laboratory scale printing masks with a surface area of 1.8x1.8 cm^2 were used for small-sized printing studies (see Appendix B). An industrial conveyor belt furnace and a convection oven were used in different combinations for drying and post-curing steps of the TLM study and SHJ solar cell fabrication. The thermal evaporation technique was applied to form Ag on the rear side of small monofacial SHJ solar cells. The edge isolation of SHJ solar cells was accomplished using a nanosecond laser, and the current-voltage values were measured under AM1.5G global spectrum. Furthermore, external quantum efficiency (EQE) was measured by Bentham PVE 300. The PLI and Suns-Voc measurements were taken to identify passivation properties and contact quality. The width and height of metal fingers and busbars were measured using a profilometer.

6.3 Results and Discussions

6.3.1 Comparison of Different TCO Layers

Two different materials as TCO layer were used on the front side of SHJ solar cells. These materials were AZO [163] and ITO [164], optimized and presented by GÜNAM colleagues. The design of the experimental procedure for the fabrication of SHJ solar cells with various TCO layers can be found in Figure 6.2. The two different front TCO materials and different metallization techniques were compared. After each deposition of a-Si:H layers, effective lifetime was measured via the lifetime tester. For all samples, the rear side was covered with 75 nm thick AZO material. The front side TCO thickness was fixed to 75 nm. The screen-printing method was used with low-temperature Ag to form metal contacts. The thicknesses of (i) a-Si:H, (p) a-Si:H, and (n) a-Si:H layers were 7, 12, and 12 nm, respectively.

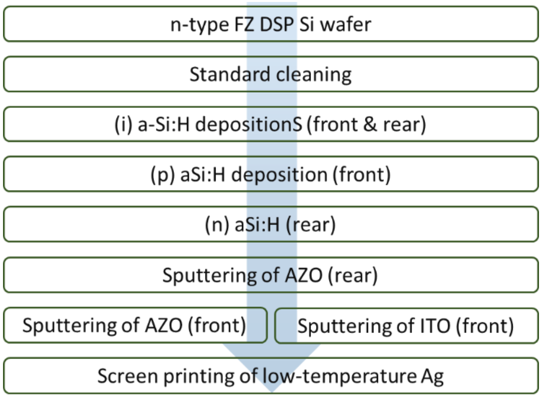

Figure 6. 2. Experimental flow chart for the fabrication of SHJ solar cells with different TCO layers.

PCD measurements traced the variation on the effective lifetime after deposition of each layer. These effective lifetime results are listed in Table 6.2. After double side deposition of (i) a-Si:H, the initial lifetime values were around 1 ms, and ${}_{imp}V_{OC}$ values were around 700 mV. The deposition of doped layers decreased passivation quality slightly except for samples with ID: IV. As discussed in the previous chapter, the nonuniform heating profile during the deposition of doped a-Si:H layers could explain this variation.

Table 6. 2. Effective lifetime measurements after (i) a-Si:H, doped a-Si:H, and TCO layers. In the below table, F and B mean the deposition side, which is front and rear, respectively.

Sample ID	After (i) a-Si:H		After (p & n) a-Si:H		After F & R AZO		After F-ITO R-AZO	
	τ (µs)	${}_{imp}V_{OC}$ (mV)	τ (µs)	${}_{imp}V_{OC}$ (mV)	τ (µs)	${}_{imp}V_{OC}$ (mV)	τ (µs)	${}_{imp}V_{OC}$ (mV)
I	1146	700	1088	691	465	675	-	
II	845	688	780	680	-		685	691
III	1090	693	1100	688	-		865	706
IV	1105	698	1255	698	560	683	-	

Sputter-induced ion bombardment decreases the passivation quality of a-Si:H by causing mechanical damages. Thermal treatment can recover this loss in passivation quality. However, there was no thermal treatment after deposition of TCO layers in these results, which indicates that after AZO sputtering, ${}_{imp}V_{OC}$ values decreased by almost 15 mV compared to the obtained passivation value after the deposition of doped a-Si:H layers. Surprisingly, after sputtering of the ITO layer, the effective lifetime values exceeded the initial passivation level.

The low-temperature Ag metal paste (Sol 580 – Heraeus) was applied to form metal contacts by screen-printing. The screen's design is revealed in Appendix B. SHJ solar cells were exposed to 30 minutes of thermal treatment at 200°C in the furnace with the air ambient. Table 6.3 lists the device parameters derived from J-V measurement of SHJ solar cells for the 4 cm^2 cell area. For each structure, five SHJ solar cells were fabricated in total, as given in Figure 6.2. When the ITO layer was used on the front side of the SHJ solar cell, FF values improved almost 4%, mainly due to the improvement of series resistance. The highest efficiency was measured as 16.4%, with front side deposition of ITO instead of AZO. Generally, V_{OC} values were lower than in the literature because of the poor initial passivation quality of (i) a-Si:H layer. The structure with a front ITO layer presented the highest FF values. The standard deviation in FF results was relatively higher for the SHJ solar cell with a front AZO layer.

Table 6. 3. Average and best SHJ solar cell parameters in terms of efficiency for front AZO and ITO structures.

Sample	V_{OC} (mV)	J_{SC} (mA/cm^2)	FF (%)	η (%)	R_S (Ω.cm^2)	R_{SH} (Ω.cm^2)
AZO - Best	680	37.92	58.13	14.98	2.51	636
AZO - Average	680±2	37.38±0.49	55.46±3.15	14.09±0.81	2.28±0.54	600±150
ITO - Best	691	38.05	62.67	16.47	0.86	136
ITO - Average	685±5	38.02±0.89	61.02±2.50	15.89±0.36	1.10±0.20	187±62

QE results of both ITO and AZO sputtered SHJ solar cells are given in Figure 6.3. There was a considerable improvement in EQE using ITO for the wavelength range of 300 to 600 nm, which is directly related to parasitic absorption caused by the band gap of TCO materials. The band gap of ITO was found as 3.68 eV and 3.26 eV for AZO [163], [164]. Moreover, AZO was superior to ITO in the IR region of the spectrum due to the AZO layer’s lower free carrier density.

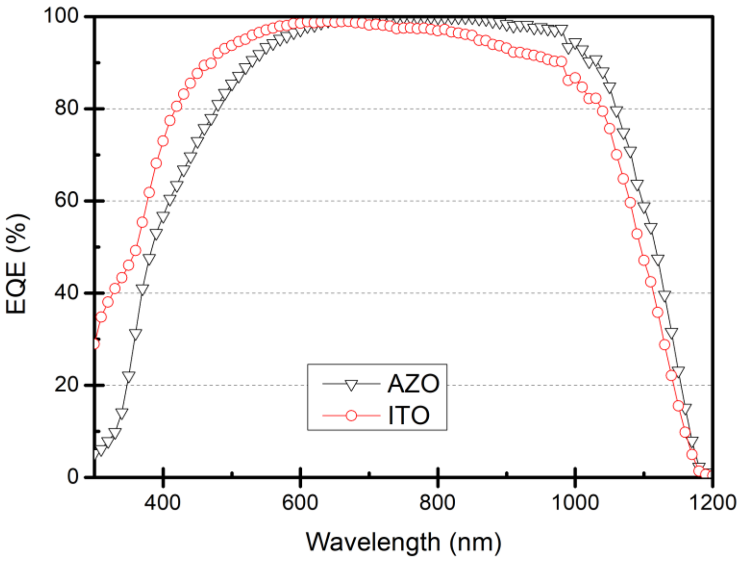

Figure 6. 3. Comparative EQE vs. wavelength variations for SHJ solar cell structures with ITO and AZO layers.

The electrical and optical properties of TCO layers can be tuned by reactive sputtering. Therefore, the free carrier absorption losses in the ITO layer could be improved by reactive sputtering, which will be discussed in the following section. Due to its superior optical and electrical properties, the ITO layer was used on the front and rear sides of SHJ solar cells in the subsequent experiments under various oxygen partial pressure values.

In the following set of experiments, doped layer thickness values were kept the same as the previous study to understand series resistance losses related to the TCO layer. ITO layers were grown on both the front and rear sides with a thickness of 75 nm. Metal contacts were formed by low-temperature Ag paste using the same screen-printing mask. Furthermore, the same thermal treatment procedure was performed after the formation of metal contacts, and eight SHJ solar cells were fabricated with an area of 4 cm^2.

Table 6. 4. Average and best SHJ solar cell parameters for the sample with double side ITO coating.

Sample	V_{OC} (mV)	J_{SC} (mA/cm^2)	FF (%)	η (%)	R_S (Ω.cm^2)	R_{SH} (Ω.cm^2)
Best	673	38.45	71.17	18.41	0.86	2000
Average	671±5	38.25±0.49	71.01±0.87	18.23 ±0.12	0.92±0.68	2800 ±1200

The FF values exceeded 70%, and the average series resistance was below 1 Ω.cm^2 when the rear side of the SHJ solar cell was coated with an ITO layer instead of AZO. The J_{SC} values slightly improved compared to the previous structure. Still, the resulting V_{OC} values were relatively low due to the lack of (i) a-Si:H passivation quality. The highest efficiency measured was 18.41%, with the integration of ITO on the rear side of the SHJ solar cell. It should be noted that after the formation of metal contacts, the solar cells went through thermal treatments with the fixed temperatures and duration of 200°C and 20 minutes, respectively.

After the formation of Ag metal contacts, SEM investigation of samples indicated a solvent leakage problem. The SEM image of the metal finger and Energy Dispersive X-ray (EDX) results of three different areas are revealed in Figure 6.4. A significant amount of carbon was detected on the dark area near the finger, related to leaked solvent from low-temperature paste. The measured C weighted percentage (Wt) was 5.24% on the dark section, and on top of the finger, we detected 98.08% Ag without any C content. The problem was related to printing parameters, compositions of paste, drying, and curing temperatures. This issue and its effect on solar cell parameters will be discussed later.

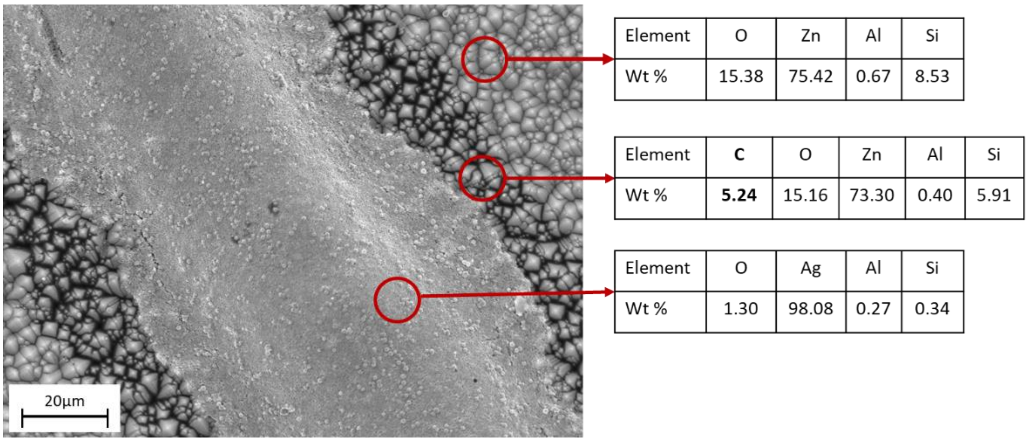

Element	O	Zn	Al	Si
Wt %	15.38	75.42	0.67	8.53

Element	**C**	O	Zn	Al	Si
Wt %	**5.24**	15.16	73.30	0.40	5.91

Element	O	Ag	Al	Si
Wt %	1.30	98.08	0.27	0.34

Figure 6. 4. SEM images of metal finger and EDX results of three different areas.

6.3.2 Properties of ITO and Optimization of ITO/Ag Contacts

For solar cell applications, a low charge carrier density is preferable to decrease parasitic absorption along with high mobility to improve the collection probability of carriers. However, there is always a trade-off between optical and electrical losses. Optimization was necessary to find the best combination of resistivity, mobility, and carrier density values of TCO for solar cell application. The experimental results are plotted in Figure 6.5.

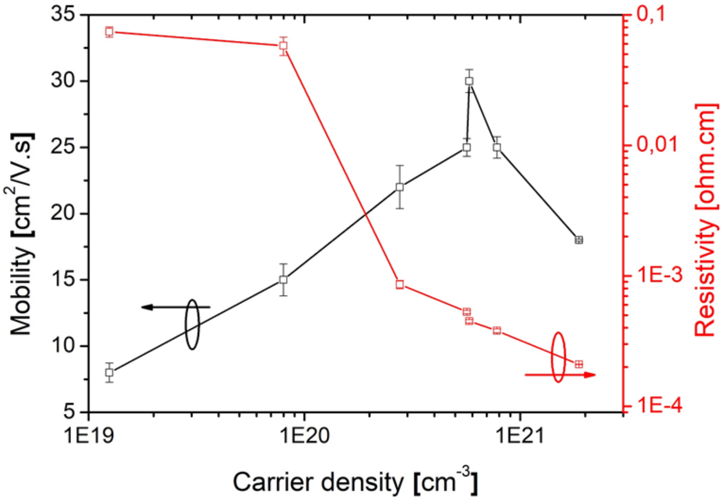

Figure 6. 5. Mobility / Resistivity vs. carrier density graph of various ITO layers.

The optical and electrical properties of the ITO layer could change by up to two orders of magnitude with the increasing oxygen partial pressure during the sputtering. The resistivity of the samples deposited with oxygen presence was higher than those deposited without oxygen. Depending on the oxygen partial pressure, mobility and charge density values changed in the range of 18 – 30 $cm^2/V.s$ and $1.25x10^{19} – 8.05x10^{21}$ cm^{-3} (see Table 6.5), respectively. The resistivity of the ITO layer decreased when the oxygen partial pressure increased. However, the mobility of ITO first rose to a certain point and then started to fall as the oxygen partial pressure increased. The mobility of the charge carriers was a function of various scattering processes from the defect sites like grain boundary, neutral and ionized impurities. In order to understand the variation in mobility, one should understand the contribution of these scattering centers. When the oxygen amount is low, the scattering of ionized and neutral impurities [165]; and charged and neutral vacancies [166] are expected to dominate the total scattering and thus the mobility. Introducing oxygen into the system first reduces the number of vacancies resulting in less scattering and higher mobility. When the oxygen reaches high levels, it starts to accumulate at the grain boundaries. The scattering from the grain boundaries with oxygen dominates the scattering in this regime and increases with oxygen accumulation, as reported by others [167].

Table 6. 5. Resistivity values of ITO films under various oxygen partial pressure values.

Oxygen partial pressure (%)	**Resistivity (Ω.cm)**
5	$(7.4\pm0.79)\text{x}10^{-2}$
3	$(5.8\pm0.74)\text{x}10^{-2}$
1	$(8.6\pm0.62)\text{x}10^{-4}$
0.8	$(5.3\pm0.17)\text{x}10^{-4}$
0.6	$(4.5\pm0.14)\text{x}10^{-4}$
0.4	$(3.8\pm0.13)\text{x}10^{-4}$
0	$(2.1\pm0.01)\text{x}10^{-4}$

From the optimization of the ITO layer, the optimum condition for oxygen partial pressure was determined as 0.6% to get the highest mobility [164].

6.3.2.1 Specific Contact Resistivity Between ITO and Ag

Specific contact resistivity (ρ_{con}) between ITO and metal contacts was studied using the TLM method to optimize the curing and drying temperatures. The metal contacts were formed via an industrial screen-printing method with low-temperature Ag paste using a standard H-grid design (see Appendix B) on top of the ITO layer. There was no oxygen partial pressure during the sputtering of the ITO layer. The experimental flow chart for the optimization of drying and curing temperatures is illustrated in Figure 6.6. The drying process, which didn’t apply until now, took place at 110°C for 12 and 15 minutes to avoid possible solvent leakage while the samples were waiting for the subsequent curing step. The curing step was performed in two different systems: a convection furnace called Nuve and a firing furnace. Contact resistance between ITO and Ag metal was characterized via TLM technique under various drying and annealing temperatures & conditions.

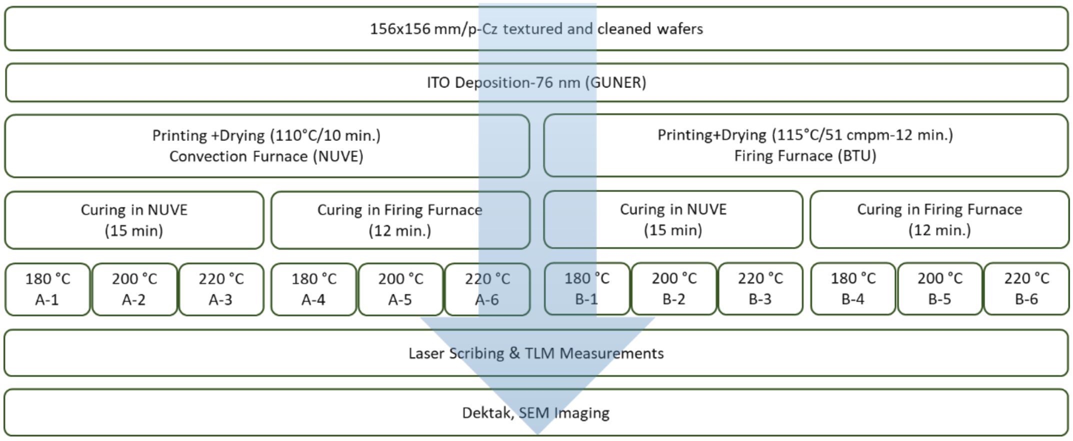

Figure 6. 6. Experimental flow chart for the optimization of drying and curing temperatures.

In Figure 6.7, TLM results are listed in terms of ρ_{con} values. The samples dried in the Nuve furnace had higher ρ_{con} values. The optimum annealing temperature was identified as 200°C for all different thermal treatment configurations. Above 200°C, ρ_{con} values increased relatively. The lowest ρ_{con} value observed was of the sample dried and cured in the firing furnace resulting in ρ_{con} of 0.4 mohm.cm^2. The optimization experiments indicate that the drying step is one of the important processes to achieve lower ρ_{con} values. Before this optimization study, there was no drying process, and contact resistivity was approximately 10 mohm.cm^2. Significant improvement was observed after optimization of low-temperature Ag.

The finger width results are provided in Figure 6.8. The width of fingers varied between 65 to 90 µm. The shorter width values were observed in sample B3. Samples dried and cured in the conveyor belt had narrower fingers, and less solvent spreading was detected. There was no clear correlation between curing temperature and the width of fingers. It should be noted that the issue with solvent leakage could not be resolved during the optimization study.

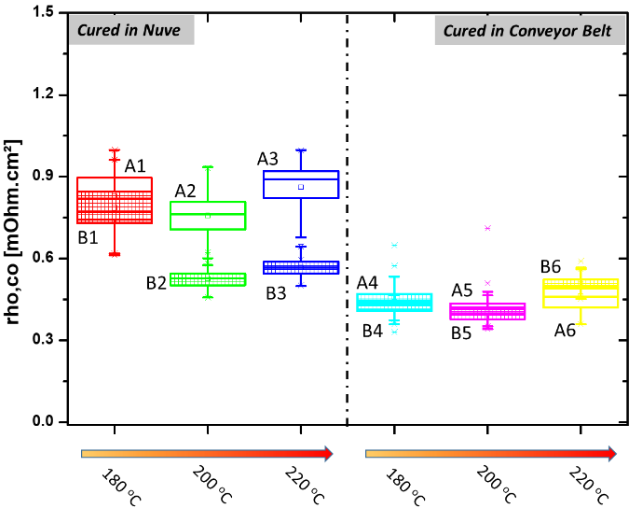

Figure 6. 7. Results of contact resistivity measurements between Ag/ITO by TLM for various curing and drying temperatures.

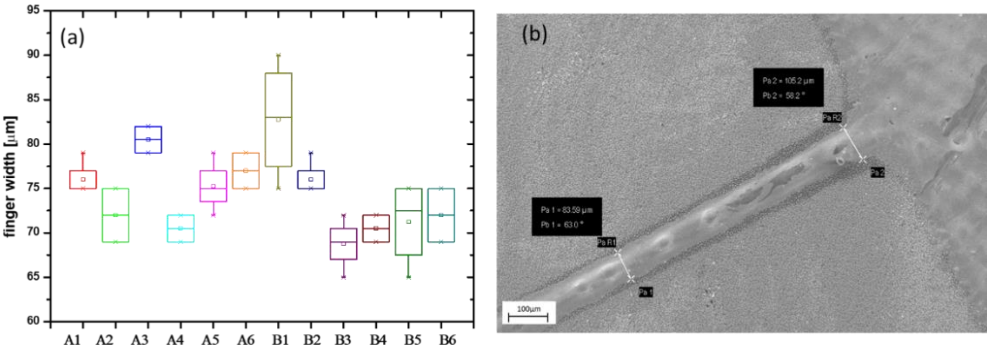

Figure 6. 8. (a) Finger width measurements and (b) SEM image of the sample A1.

6.3.3 Effect of ITO Layer Properties on SHJ Cell Performance

The experimental flow of reactive ITO sputtering application on SHJ solar cells is illustrated in Figure 6.9. Three full-size (156.75x156.75 mm^2) bifacial SHJ solar cells were fabricated under various conditions. The ITO layer was deposited without oxygen partial pressure in the first fabrication run of the SHJ cell called SHJ-1. Moreover, the thickness of the (n) a-Si:H layer was increased by 0.5 nm. Reactive ITO sputtering with 0.6% oxygen partial pressure was used for the ITO layer depositions in the second fabrication run of the SHJ solar cell (SHJ-2). Meanwhile, the other process parameters were kept the same as parameters used in the fabrication of SHJ-1. For the last fabrication run of SHJ solar cell (SHJ-3), the thickness of (n) a-Si:H was increased to 13 nm, while other deposition parameters were the same.

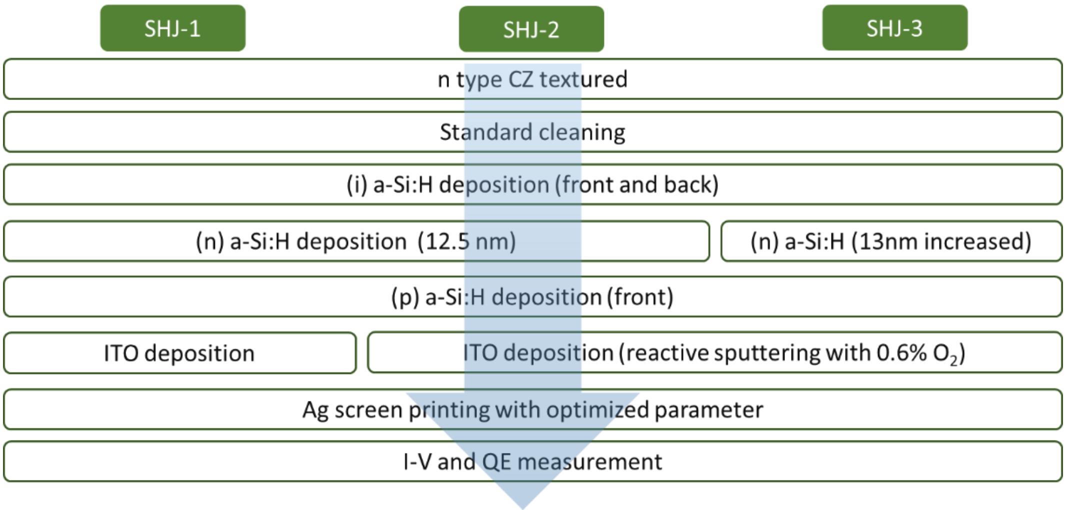

Figure 6. 9. Experimental flow chart of the reactive ITO sputtering application on SHJ solar cell.

Current density-Voltage, J-V measurement results of bifacial SHJ solar cells under the illumination of 1000 W/m^2 were given in Figure 6.10, and solar cell parameters obtained from these J-V variations are listed in Table 6.6. When the thickness of (n) aSi:H increased by 0.5 nm, FF and J_{SC} values increased slightly compared to the SHJ solar cell parameters obtained in the previous section. Series resistance was almost the same, and the efficiency value had risen to 20.17%. When the oxygen partial pressure was fixed to 0.6% during ITO depositions (SHJ-2), FF and J_{SC} values increased slightly. Moreover, series resistance decreased significantly compared to ITO growth without reactive sputtering, and the efficiency value increased to 20.56%. In the last SHJ solar cell, the thickness of (n) a-Si:H layer was increased by 1 nm compared to the previous study (SHJ-3). J_{SC} value improved by almost 0.4 mA/cm^{2,} and FF also improved slightly. The record efficiency achieved in bifacial SHJ solar cells was measured as 20.76% in 170 cm^2.

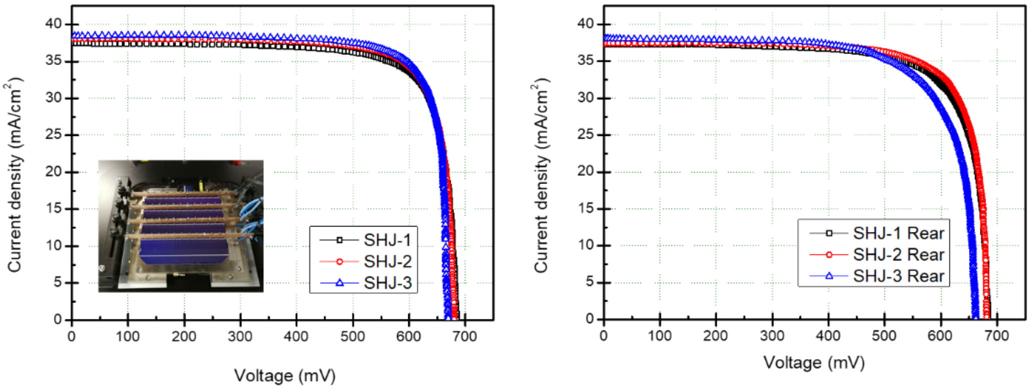

Figure 6. 10. J-V results of SHJ solar cells for front and rear illuminations of 1000 W/m^2.

Table 6. 6. Solar cell parameters of bifacial SHJ solar cells for front and rear illuminations of 1000 W/m^2.

Sample	**V_{OC} (mV)**	**J_{SC} (mA/cm^2)**	**FF (%)**	**η (%)**	**R_S (Ω.cm^2)**	**R_{SH} (Ω.cm^2)**
SHJ-1	685	37.45	78.63	20.17	0.75	108000
SHJ-2	681	38.06	79.38	20.56	0.31	106000
SHJ-3	670	38.40	80.72	20.76	0.38	135200
SHJ-1 rear	685	37.24	75.50	19.26	0.90	96000
SHJ-2 rear	681	37.43	78.09	19.91	0.68	60000
SHJ-3 rear	662	38.09	72.45	18.27	0.39	57000

The effect of the improvement in the electrical properties of the ITO layer properties on SHJ cells can be observed from EQE results, as shown in Figure 6.11. In the first fabrication run of SHJ solar cell, the measured free carrier and parasitic absorption losses were higher than the SHJ solar cell with ITO prepared by reactive sputtering. The decrease in free carrier absorption in NIR was due to the reduced carrier density of ITO film deposited with oxygen [167]–[169]. Similarly, the blue response improved with reduced parasitic absorption in the blue region due to the lower absorption coefficient of the reactive sputtered ITO layer. However, the increment in carrier density led to pushing the Fermi level to higher energy, resulting in an enlargement in the optical band gap known as the Burstein Moss Shift. Due to this effect, in the wavelength range between 300-340 nm, parasitic absorption of the second run cell was slightly higher than that of the ITO layer grown without oxygen partial pressure since the optical band gap value of the ITO layer deposited by reactive sputtering was lower than the one without oxygen partial pressure [167]. Decreasing the carrier density of the ITO layers might cause a slight reduction of parasitic absorption. Reducing absorption edges in both NIR and blue regions led to a slight influence on J-V characteristics. The current density of the SHJ-1 solar cell was 37.45 mA/cm^2, while the current density of the second SHJ-2 solar cell was 38.06 mA/cm^2. The enhancement in the J_{SC} value with oxygen partial pressure was nearly 0.6 mA/cm^2, which is directly related to the reduction in the free carrier and parasitic absorption losses. The passivation properties of all SHJ solar cells before ITO deposition were almost in the same range.

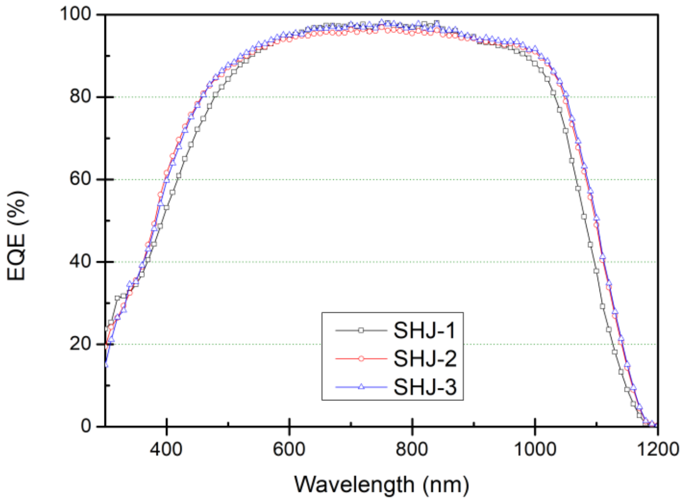

Figure 6. 11. EQE results of bifacial SHJ solar cells.

6.3.3.1 Investigation of Solvent Leakage Problem

The low-temperature Ag paste used during the fabrication of previous SHJ solar cells was Sol 580 from Heraeus company for the formation of metal contacts. Later, we used the upgraded version of this low-temperature Ag paste, known as Sol 590. After switching, the solvent leakage problem was highly aggravated. The picture and a representative sketch of the solar cell with a spot of EQE measurement setup can be observed in Figure 6.12. Due to the solvent leakage, the spot of the setup was in direct interaction with the dark area. Figure 6.12 reveals the EQE results of the solar cells metalized by two different Ag pastes. The solar cell named “record SHJ” and “SHJ 3-1” in the figure were those printed by Sol 580 and Sol 590 low-temperature pastes, respectively. We found that the area where solvent leaked showed parasitic absorption in the UV and IR spectrum, resulting in a considerable amount of current losses.

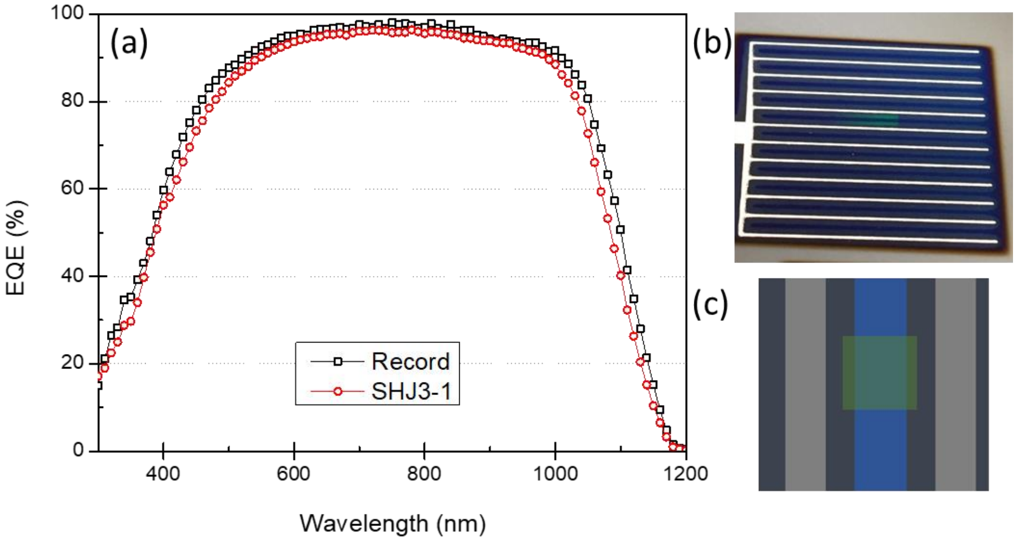

Figure 6. 12. (a) EQE comparison of two SHJ solar cells printed with low-temperature Ag paste: Sol 580 and Sol 590, (b) image of screen-printed SHJ solar cell, and (c) representative sketch of EQE spot, fingers, and the dark area.

Furthermore, with the usage of Sol 590, the FF values decreased, and R_S increased. The change in series resistance was directly related to contact resistivity between ITO and Ag and the relatively higher line resistance of Ag busbar and fingers. Therefore, to understand the behavior of low-temperature Ag paste, small area SHJ solar cells were fabricated since the PECVD cluster system has a limited fabrication capacity.

6.3.4 Fabrication of Small Area SHJ Solar Cell

The experimental flow chart for the fabrication of SHJ solar cells with a 4 cm^2 area is given in Figure 6.13. The difference from previous work is the shadow mask deposition of the ITO layer on both sides instead of full coverage. Accordingly, during the ITO sputtering, a shadow mask from the mc-Si wafer designed with 4 cm^2 openings was used (see Figure 6.13). Moreover, on the rear side, instead of Ag screen-printing, the thermal evaporation technique was used for complete coverage of Ag with a thickness of 300 nm. In this configuration, screen-printing parameters were explored.

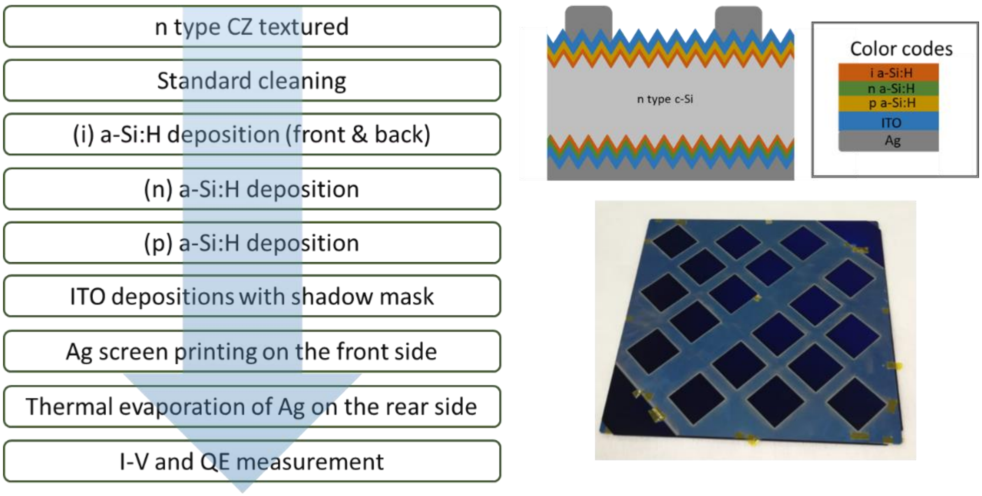

Figure 6. 13. Experimental flow chart for the fabrication of SHJ solar cells with a 4 cm^2 area.

The impact of the annealing duration and temperature on SHJ solar cell parameters was investigated. Three different curing temperatures were selected regarding contact resistivity results (190, 205, and 220°C), and results were taken for four different durations. The SHJ solar parameters can be found in Figure 6.14. Regarding the V_{OC} values, the passivation quality decreased when curing at 220°C, where V_{OC} values were continuously declining with respect to the increase in duration. On the other hand, passivation quality was almost the same for curing at 190 and 205°C for up to 60 minutes of annealing. Due to the shadowing effect of spreading metal and solvent, it was impossible to reach a conclusion regarding the J_{SC} values for different annealing temperatures. However, there was a decrease in J_{SC} for longer durations at all temperatures. Moreover, the FF movement helped us with a deduction; as the annealing duration increased, FF decreased except for annealing at 190°C for 10 minutes. The highest efficiency measured was 19.5%, curing at 190°C for 30 minutes. The optimum curing temperature and duration were thus selected as 190°C and 30 minutes, respectively.

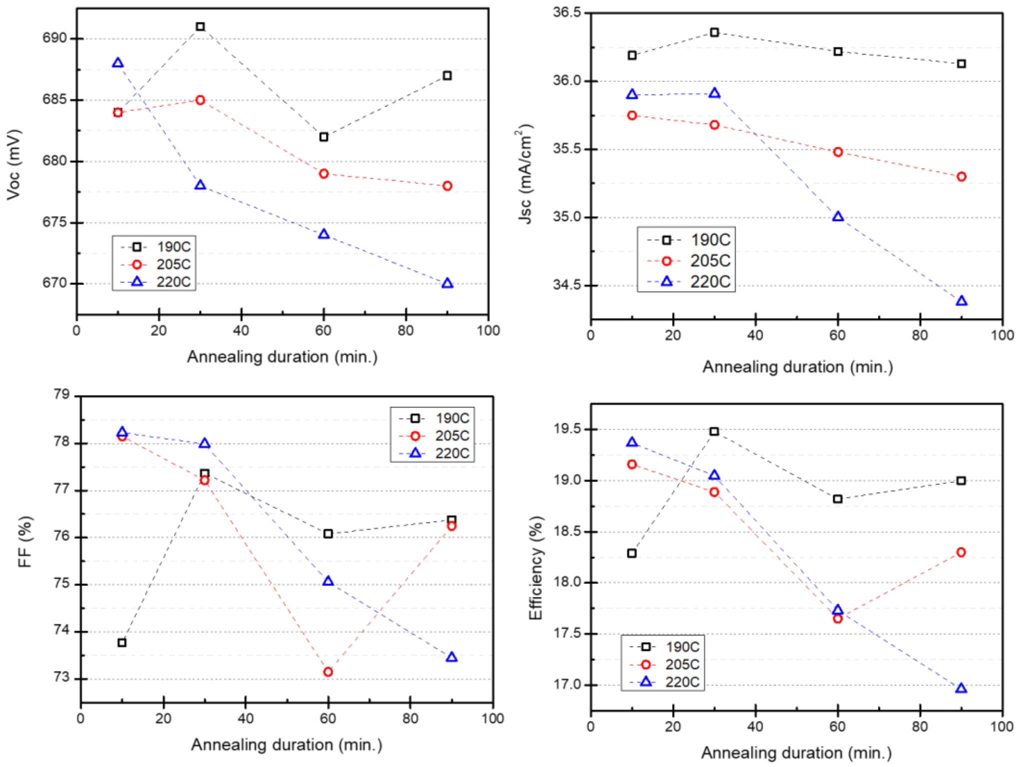

Figure 6. 14. Variation of SHJ solar cell parameters for various curing temperatures and durations.

After optimization of curing temperature and duration, four SHJ solar cells were fabricated under optimum deposition conditions. Device parameters for these SHJ solar cells are listed in Table 6.7.

Table 6. 7. Results for the SHJ solar cell parameters.

Sample code	V_{OC} (mV)	J_{SC} (mA/cm^2)	FF (%)	η (%)
SHJ4-2	704	38.34	71.48	19.30
SHJ4-4	698	38.10	72.72	19.34
SHJ4-5	706	38.63	73.24	19.99
SHJ4-6	713	38.53	74.31	20.41

The SHJ solar cells were still suffering from metallization problems resulting in relatively low FF values. Moreover, J_{SC} values were in the same range compared to the record solar cell. However, the spreading of solvent was still effective in shadowing losses. The highest V_{OC} value of 713 mV for an SHJ solar cell was noted. The highest efficiency measured was 20.41 at an area of 4 cm^2. From this set of fabrication, two SHJ solar cells were selected to be used in the degradation study. The solar cells were kept at 85°C for 66 h to understand the degradation profile of the SHJ solar cells. During this period, measurements of the SHJ solar cells were taken periodically via the SunsVoc setup. The degradation of two SHJ solar cells in terms of normalized V_{OC} variation is provided in Figure 6.15. The V_{OC} difference in the first eight hours was less than 1%. After 66 hours of annealing, the decrease in V_{OC} was 1.03% for SHJ 4-2 and 0.86 for SHJ 4-6 coded solar cells, where SHJ solar cells were almost stabilized after 30h. One can conclude that SHJ solar cell technology is one of the proper technologies that would be able to operate in high-temperature climates.

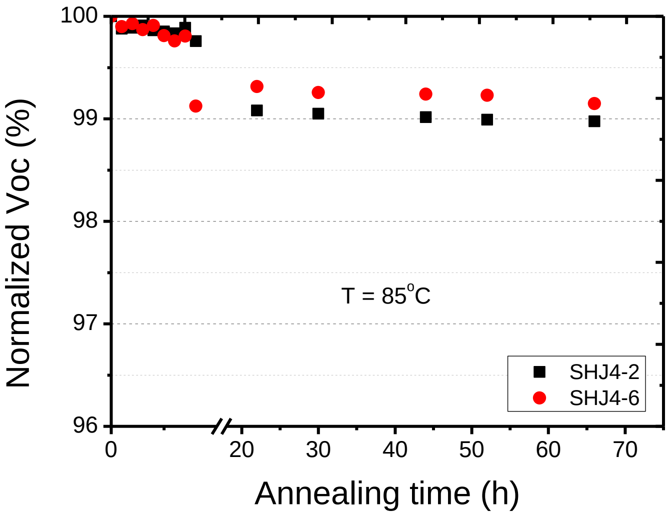

Figure 6. 15. Normalized V_{OC} of degraded SHJ solar cells.

6.3.4.1 Contact Resistivity Analysis

Contact resistivity of c-Si/aSi:H/ITO structure is one of the deterministic parameters on the performance of SHJ solar cells. For the calculation of ρ_{con}, two different methods were used: confined TLM [170] and spreading resistance modeling with four-point probe (4PP) method. The results of both approaches were compared. The experimental flow chart of contact resistivity studies is illustrated in Figure 6.16. The main idea was to correlate specific contact resistivity and thickness values of (i) a-Si:H and ITO layers. Therefore, two thicknesses of (i) a-Si:H, 7 and 14 nm; and two thicknesses of ITO, 75 and 210 nm, were selected to analyze the variation in the contact resistivities.

Moreover, ITO layers were grown on (n) a-Si:H layer with a shadow mask to form a confined TLM structure (see Figure 6.16). All depositions were done on one side of c-Si wafers. Later, the impact of higher oxygen partial pressure during ITO growth was examined by both confined TLM (between Ag/ITO) and the 4PP method (c-Si/aSi:H/ITO).

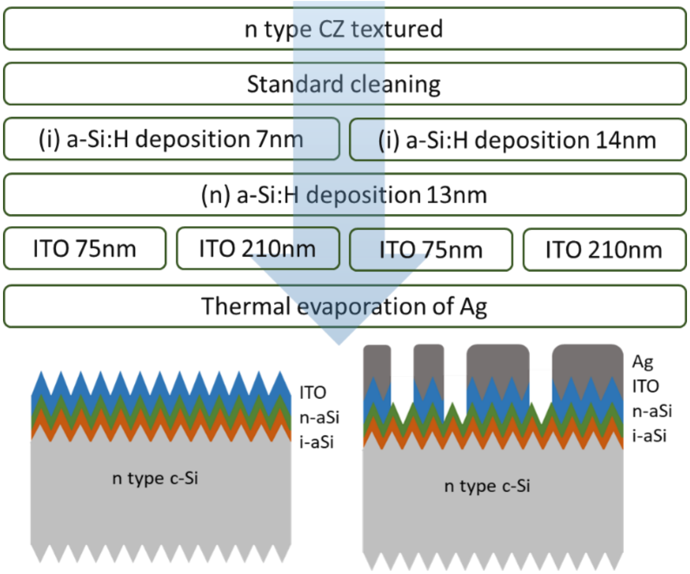

Figure 6. 16. Experimental flow chart of contact resistivity studies and cross-sectional views of structures.

In the first set, the thickness of (i) a-Si:H was increased to 14 nm. The resulting contact resistivity values were significantly high, in which two calculation methods were in good correlation (see Table 6.8). Moreover, the average ρ_{con} value was approximately 230 mΩ.cm^2.

Table 6. 8. Contact resistivity results of the first set with (i) a-Si:H and ITO thickness of 14 and 75 nm, respectively.

Sample codes	Structure	Confined TLM (mΩ.cm^2)	4PP (mΩ.cm^2)
40	(n) c-Si / 14nm (i) aSi:H / (n) aSi:H / 75nm ITO	-	191
41		-	198
45		-	290
39		190	-
42		291	-

In the second set, the thicknesses of ITO was increased to 210 nm from 75 nm, and the average ρ_{con} value was raised above 250 mΩ.cm^2. By comparing the two different ITO thicknesses, one can conclude that the resistivity contribution of ITO is almost negligible for the contact resistivity.

Table 6. 9. Contact resistivity results of the second set with (i) a-Si:H and ITO thickness of 14 and 210 nm, respectively.

Sample codes	Structure	Confined TLM (mΩ.cm^2)	4PP (mΩ.cm^2)
A-37	(n)c-Si / 14nm (i)aSi:H / (n)aSi:H / 210nm ITO	-	234
A-39		-	230
A-34		257	-
A-38		291	-

In the third experimental set, the contact resistivity value of the SHJ solar cell structure was measured, for which the results are listed in Table 6.10. In this structure, ρ_{con} values decreased to less than 100 mΩ.cm^2. However, the literature reports values lower than 50 mΩ.cm^2 [171]. The results indicate that even though the ρ_{con} values were in a compatible range with the literature, they should be decreased to achieve higher device performance. It could be possible by either changing the doping concentration of (n) a-Si:H or properties of the ITO layer.

Table 6. 10. Contact resistivity results of the third set with (i) a-Si:H and ITO thickness of 7 and 75 nm, respectively.

Sample code	Structure	Confined TLM (mΩ.cm^2)	4PP (mΩ.cm^2)
E-35	(n)c-Si / 7nm (i)aSi:H / (n)aSi:H / 75nm ITO	-	72
E-37		-	98
E-26		85	-
E-27		105	-

The contact resistivity for higher oxygen partial pressures was analyzed to understand the relationship between metal contacts, ITO, and (n) a-Si:H layers. In Figure 6.17, contact resistivity results of c-Si/a-Si/ITO structure from 4PP method (red triangle) and TLM results (black circle) for Ag/ITO are listed for different oxygen partial pressures. The standard deposition condition was with 0.6% oxygen partial pressure with superior contact properties than the higher oxygen partial pressure ones. The results indicated that higher oxygen partial pressure values were not applicable for SHJ solar cells due to the relatively high contact resistivity. Moreover, ρ_{con} between metal and ITO was less than 1 mΩ.cm^2 and ρ_{con} between ITO to c-Si was 50 mΩ.cm^{2,} which are values compatible with the results in the literature. An increase in the oxygen partial pressure led to a rise in contact resistivities.

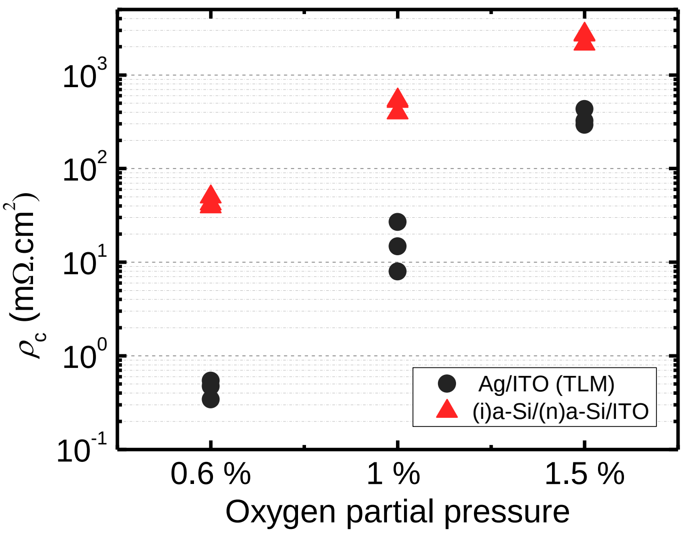

Figure 6. 17. Contact resistivity results for various oxygen partial pressures.

6.3.4.2 Comparison of Different Low-temperature Ag Pastes

The solvent leakage problem observed on printing with low-temperature Ag pastes Sol 580 and Sol 590 could not be resolved during the study. Therefore, we decided to try other commercially available products. Two low-temperature Ag pastes were selected from Pharos Materials and Namic Corporation. Except for the Ag paste, all fabrication steps were similar and in accordance with the optimum deposition conditions. In total, 10 SHJ solar cells were fabricated for each different Ag paste. The parameters of SHJ solar cells fabricated with different Ag pastes are given in Figure 6.18. All SHJ solar cells suffered from a lack of passivation, which was related to the low passivation quality of the (i) a-Si:H layer. Due to a mechanical problem in the i-chamber reactor, the distance between anode and cathode completely changed, resulting in a decreased passivation quality. Slightly higher J_{SC} values were achieved using Pharos Ag paste. The solvent spread was much less of a problem for Pharos than the other two low-temperature Ag pastes. This partial solution resulted in a slight increase in J_{SC} values. However, the Ag paste from Pharos showed a better performance in terms of FF and η results. Moreover, when metallization was done by Pharos Ag paste, the variation in the FF values was significantly lower. The highest efficiency was 20.32% for the sample metalized with Pharos Ag paste.

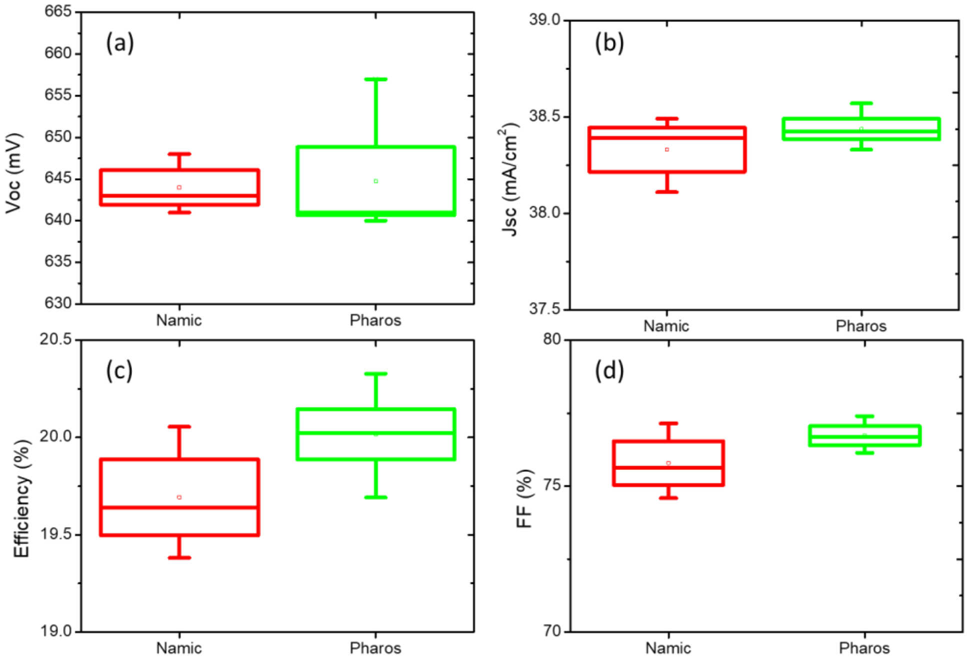

Figure 6. 18. Comparative results for SHJ solar cell parameters metalized by two different low-temperature Ag pastes.

Figure 6.19 represents the comparison of EQE results for both low-temperature Ag pastes. Slightly better performance was observed with Pharos paste for the wavelength range between 500 to 900 nm due to reduced solvent spread. Even though different low-temperature Ag pastes were used on SHJ solar cells, the problem with the solvent spread could not be solved completely.

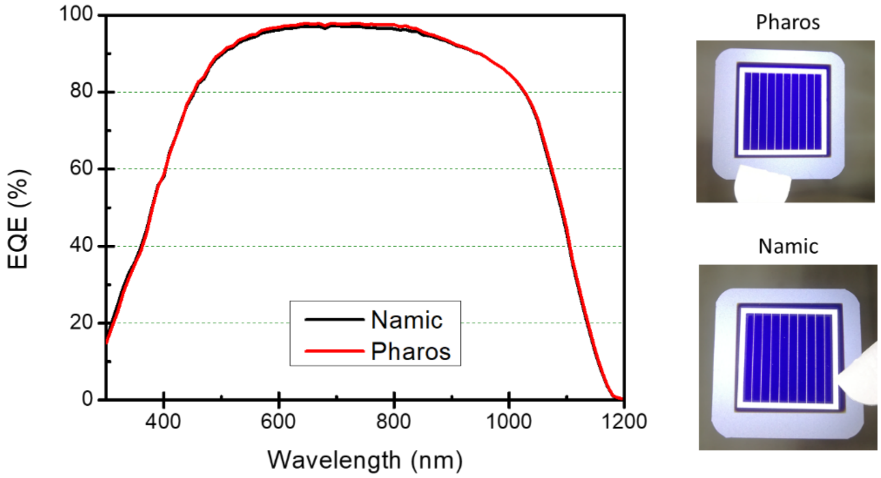

Figure 6. 19. EQE results of SHJ solar cells metalized by two different low-temperature Ag pastes and device images.

The comparison of different low-temperature Ag pastes revealed better performance from the Pharos paste. It was used for the metalization of SHJ solar cells after solving the mechanical problem with the i-chamber, and the passivation quality of (i) a-Si:H was recovered. After that, the V_{OC} value exceeded 700 mV. We achieved record SHJ solar cell efficiency of **21.22%** with an area of 4 cm^2, where the J-V curve and solar cell parameters are given in Figure 6.20.

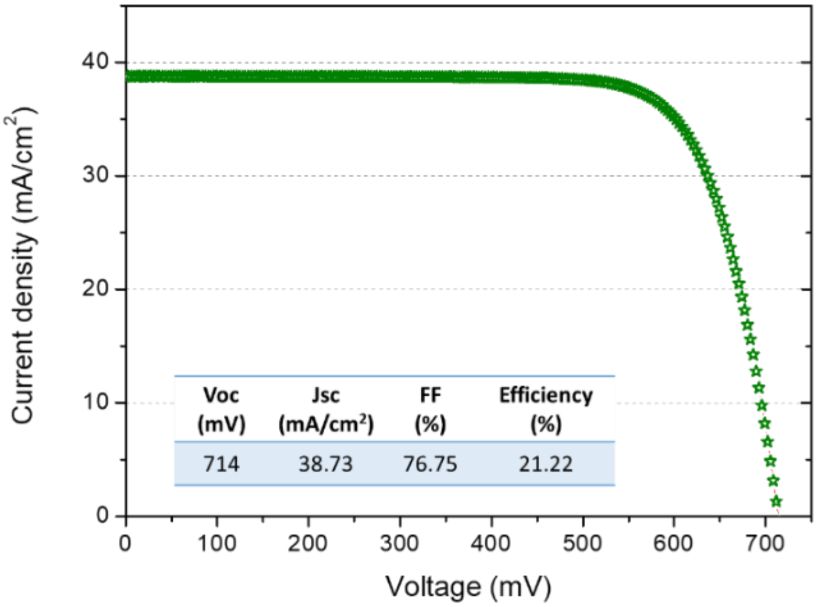

Voc (mV)	Jsc (mA/cm^2)	FF (%)	Efficiency (%)
714	38.73	76.75	21.22

Figure 6. 20. The J-V graph for the record SHJ solar cell.

6.3.5 Integration of Wide Band Gap Emitter to SHJ Solar Cells

SHJ solar cells suffer from parasitic absorption at the emitter side due to the relatively low band gap of the (p) a-Si:H layer. The optimization results for the (p) a-Si:H layer were discussed in the previous chapter. The band gap of (p) a-Si:H varies between 1.6 eV to 1.7 eV. One alternative to (p) a-Si:H is (p) a-SiC$_x$:H, where the band gap value can be tuned between 1.8 eV to 2.3 eV. Optimum band gap values were determined as 1.9 and 2.0 eV from the simulation results. Two deposition parameters were selected to be used in the fabrication of SHJ solar cells. Table 6.11 lists the deposition parameters of (p) a-SiC$_x$:H layer, which were selected with respect to conductivity, band gap, and activation energy. The selected layer's activation energy was 0.35 eV, conductivity value was approximately 1x10^{-4} S/cm and band gap of a-SiC$_x$:H was 1.9 eV (a-SiC$_x$:H-1) and 2.0 eV (a-SiC$_x$:H-2).

Table 6. 11. Deposition parameters of (p) a-SiC$_x$:H layers.

Deposition parameters	a-SiC$_x$:H-1	a-SiC$_x$:H-2
SiH_4 flow	20	20
B_2H_6 flow	30	30
H_2 flow	120	120
CH_4 flow	10	30
Deposition power	50	50

The thickness of (p) a-SiC$_x$:H used in SHJ solar cells was 12 nm. The parameters of SHJ solar cells fabricated with these deposition conditions are given in Table 6.12.

Table 6. 12. SHJ solar cell parameters with a-SiC$_x$:H emitter layer.

Sample	Voc (mV)	Jsc (mA/cm^2)	FF (%)	η (%)	R_S (Ω.cm)	R_{SH} (Ω.cm)
SHJ	665	38.49	71.09	18.19	1.83	5260
(p)aSiC$_x$1	657	37.28	67.92	16.63	2.45	5125
(p)aSiC$_x$2	650	37.10	67.38	16.24	2.63	7990

All SHJ solar cells were suffering from low passivation quality related to the aforementioned problem. There was a slight improvement in J_{SC} value for (p) a-SiC$_x$:H-1 compared to (p) a-SiC$_x$:H-2, where the emitters' band gap was 1.9 and 2 eV, respectively. Relatively low J_{SC} values were found for wide band gap emitter SHJ solar cells. Due to the higher resistivity of (p) a-SiC$_x$:H layers, the overall series resistance was significantly higher than (p) a-Si:H, resulting in a decrease in FF values. In Figure 6.21, EQE results for SHJ solar cells are presented. Surprisingly, there was no clear evidence of a high band gap emitter on EQE results. This could be explained by high resistivity and relatively high thickness of (p) a-SiC$_x$:H layers. The next step is to identify the impact of the (p) a-SiC$_x$:H thickness.

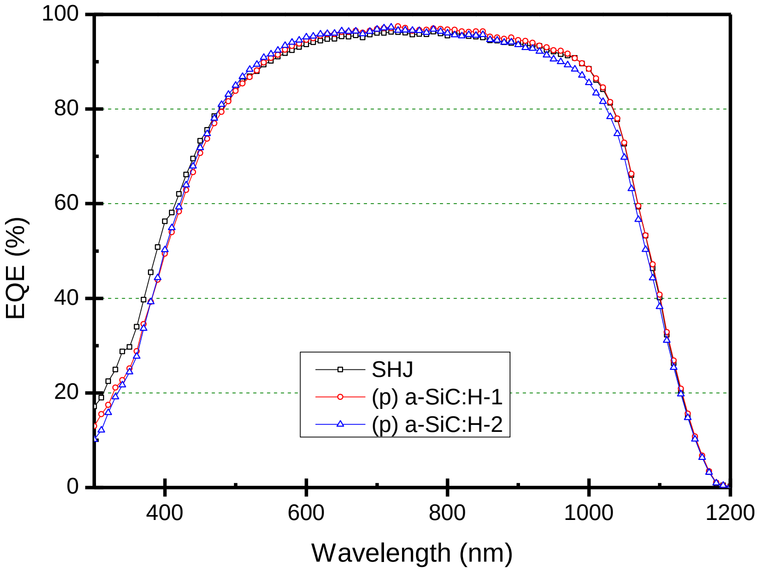

Figure 6. 21. Comparison of EQE results for wide band gap SHJ solar cells.

Thereafter, the thickness of (p) a-SiC_x:H layer was decreased to 10 nm, and two SHJ solar cells were fabricated. The SHJ solar cell parameters of the study can be found in Table 6. 13. The decrease in the thickness of (p) a-SiC_x:H layer led to a reduction of R_S and an increase in J_{SC}, FF, and η, compared to previous SHJ solar cell parameters. The highest efficiency recorded was 20% with (p) a-SiC_x:H SHJ solar cell structure. Figure 6.22 compares EQE results for standard and (p) a-SiC_x:H emitter SHJ solar cells. The spectral response of SHJ solar cells below 700nm was improved by integrating the wide band gap (p) a-SiC_x:H layer resulting in above 38.80 mA/cm^2 current density.

Table 6. 13. SHJ solar cell parameters with the 10 nm thick (p) a-SiC_x:H layer.

Sample code	V_{OC} (mV)	J_{SC} (mA/cm^2)	FF (%)	η (%)	R_S (Ω.cm)	R_{SH} (Ω.cm)
(p) aSiC_x:H-7	682	38.82	75.33	19.94	1.90	4000
(p) aSiC_x:H-8	679	38.86	75.79	20.00	1.85	3600

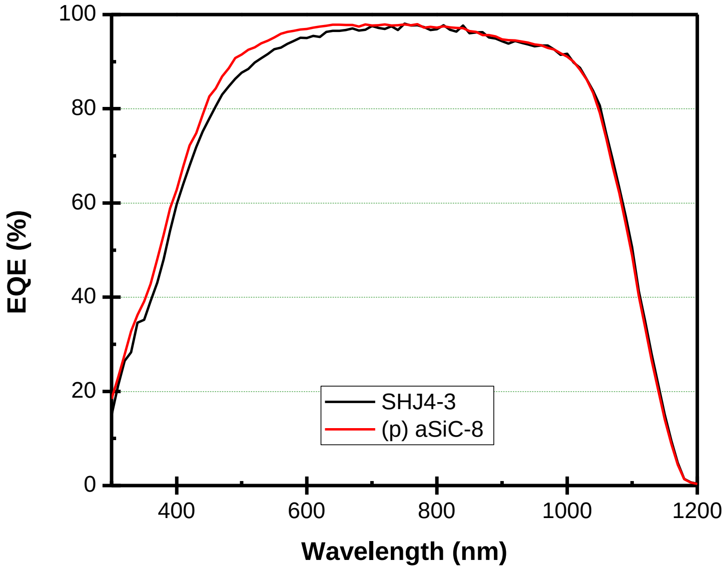

Figure 6. 22. EQE results of SHJ solar cells with standard and wide band gap emitter layers.

Integrating (p) a-SiC$_x$:H layer to the SHJ solar cell structure helped achieve SHJ solar cell efficiencies over 20%. One conclusion is that the parasitic absorption losses could be decreased by applying (p) a-SiC$_x$:H emitter to SHJ solar cell structure. However, due to the relatively high resistivity of the material, the thickness of (p) a-SiC$_x$:H should be decreased further to achieve better solar cell performance.

6.3.6 Carrier Selective Heterocontact Solar Cells

The application of carrier selective heterocontact (CSH) solar cells attracts significant attention through research groups. The main advantages of CSH on SHJ solar cells are the low-temperature and straightforward processes with tailored optical characteristics, which result in decreased parasitic absorption due to the high band gap properties. The optimized deposition conditions of carrier selective heterocontact layers were implanted to solar cell structures, as shown in Figure 6.23. Four different structures were examined. These were hole selective heterocontact

(HSH), electron selective heterocontact (ESH), carrier selective heterocontact (CSH), and standard SHJ solar cells.

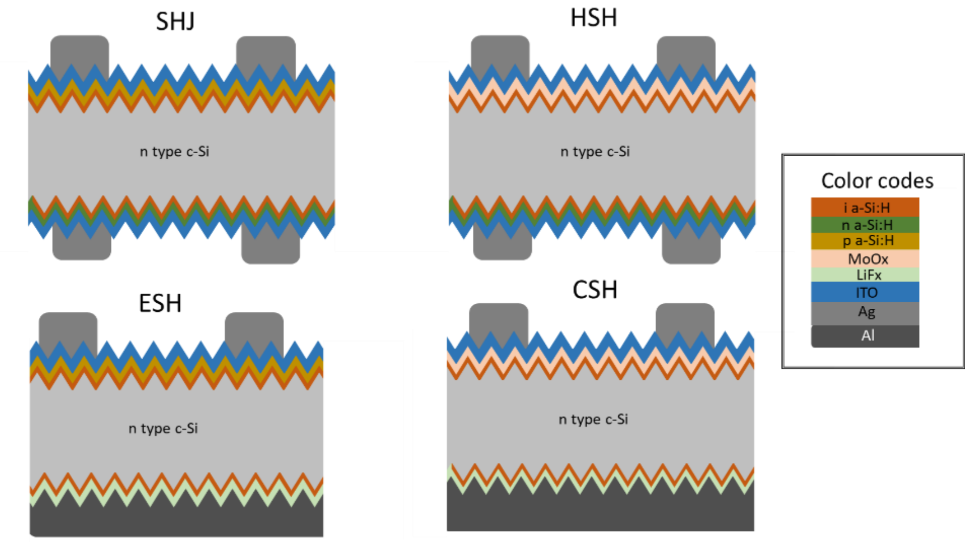

Figure 6. 23. Cross-sectional view of different CSH solar cell structures.

The experimental flow chart is provided in Figure 6.24. The standard SHJ solar cell and other structures were fabricated in successive processes. N-type CZ textured Si wafers were used with traditional cleaning recipes. MoO_x layers were thermally grown right after depositions of a-Si:H layers. ITO layers were deposited with 0.6% partial pressure of oxygen with a thickness of 75 nm on both sides. After ITO deposition, low-temperature Ag paste was used to form metal contacts on the front side. Rear sides were coated with thermally grown Ag on the SHJ and HSH solar cells. LiF_x/Al layers were formed via thermal evaporation technique with a thickness of 1 nm after forming metal contacts on the front side for ESH and CSH solar cell structures.

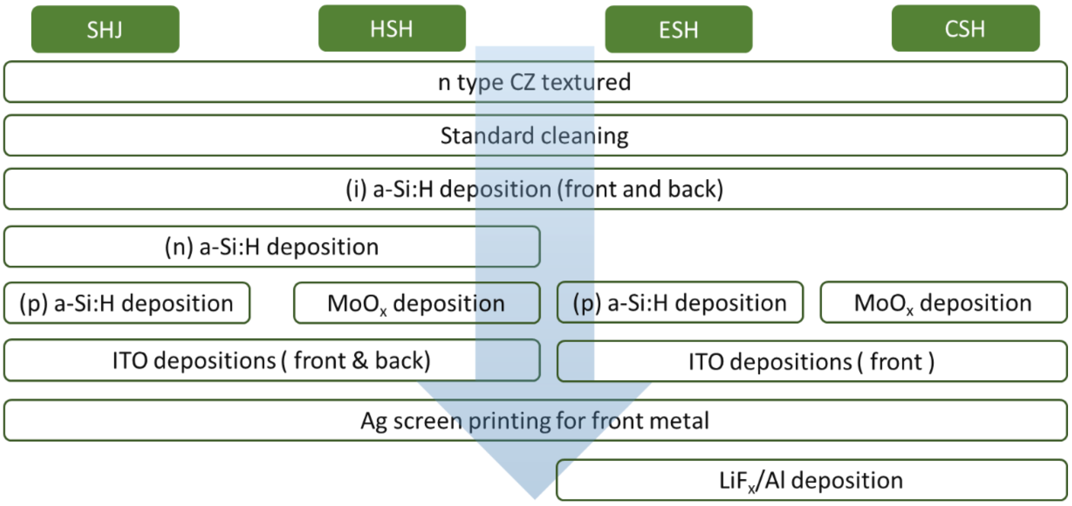

Figure 6. 24. Experimental flow chart for four different solar cell structures.

6.3.6.1 Hole Selective Heterocontact Solar Cells

HSH solar cells were fabricated using MoO$_x$ films of two different thicknesses, 8 and 12 nm. The solar cell results are listed in Table 6.14.

Table 6. 14. HSH solar cell parameters for different thicknesses of MoO$_x$.

MoO$_x$ thickness (nm)	V_{OC} (mV)	J_{SC} (mA/cm^2)	FF (%)	η (%)	R_S (Ω.cm)	R_{SH} (Ω.cm)
12 nm	671	37.21	73.05	18.24	2.58	6700
8 nm	694	39.21	75.20	20.46	2.24	8000
SHJ solar cell	670	38.40	80.72	20.76	0.38	6900

The variation in V_{OC} values is mainly related to the initial passivation quality of (i) a-Si:H layers. The thickness of the MoO$_x$ layer is essential for achieving better performance on solar cells. For the 12 nm thick MoO$_x$ sample, the HSH solar cell suffered from high series resistance and low FF value compared to the others. When the thickness of MoO$_x$ was decreased to 8 nm, J_{SC} improved significantly, resulting in a higher value compared to SHJ solar cells. The decrease in series resistance also increased the FF value. The highest efficiency achieved on HSH solar cell structure was 20.52% for the 8 nm thick MoO_x film. Figure 6.25 compares the EQE results of HSH and SHJ solar cells. A significant improvement was noted in the spectral response of HSH solar cells for below 600 nm. Due to the high band gap nature of MoO_x, parasitic absorption was less than SHJ solar cells. However, above 600 nm, there was a loss in the EQE results due to the parasitic sub-band gap absorption [172].

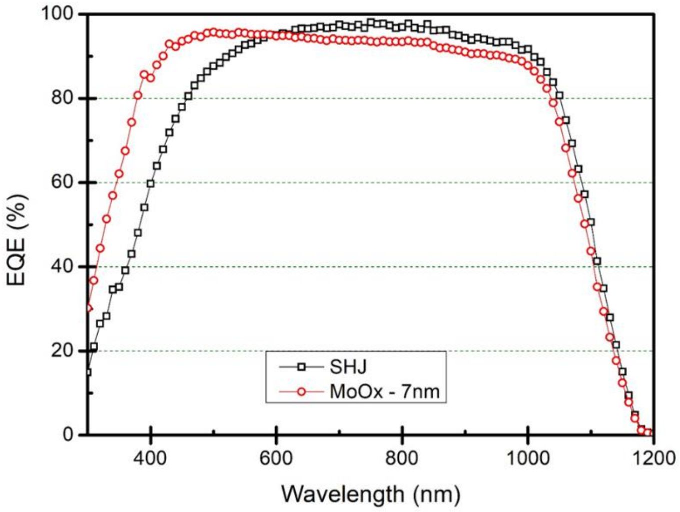

Figure 6. 25. Comparison of the EQE results of HSH and SHJ solar cells.

6.3.6.2 Electron Selective Heterocontact Solar Cells

The experimental flow chart (see Figure 6.24) includes an annealing step after the formation of front metal contacts. The set has a detrimental effect on the properties of solar cell performance. Since the rear side is covered with (i) a-Si:H, it is open to contaminants or damage during metallization and annealing processes. Five different annealing temperatures were selected to clarify the relationship between annealing temperature after the formation of front metals with ESH solar cell efficiencies. The results are presented in Figure 6.26 in normalized efficiency values with respect to the highest ESH solar cell efficiency. The optimum annealing temperature was identified as 190°C for 30 minutes. Below 190°C, the contact resistivity values between ITO and Ag were relatively high, as explained previously. On the other hand, the passivation quality of (i) a-Si:H degraded above 220°C.

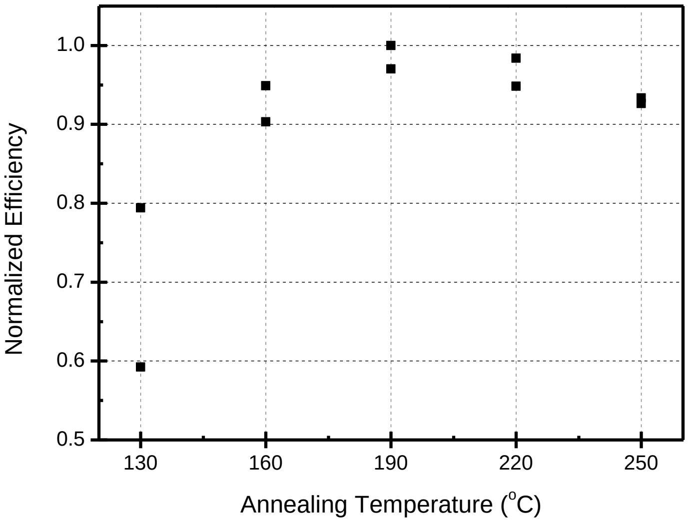

Figure 6. 26. The normalized efficiency values of ESH solar cells for different annealing temperatures.

After optimization of annealing temperature, four SHJ and ESH solar cells were fabricated; the results are provided in Figure 6.27. The main obstacle to applying the LiF_x/Al stack layer as an electron selective contact is the loss in the passivation properties of (i) a-Si:H [173]. Similar behavior was observed in the other cell results. The V_{OC} values decreased by almost 10 mV compared to the SHJ solar cells. The highest V_{OC} achieved for SHJ solar cell was 712 mV, while for ESH solar cell, this value was 703 mV. Relatively low J_{SC} due to the loss in the infrared part of the spectrum where EQE results are shown in Figure 6.28. The FF values were lower for ESC than SHJ solar cells due to relatively higher contact resistivity between LiF_x and c-Si wafers. It should be noted that the record solar cell efficiency for ESC solar cell structure was 19.4% without the usage of any interfacial layer between LiF_x and (i) a-Si:H layers [173]. The highest efficiency achieved for ESH solar cell structure during this study was 18.9%.

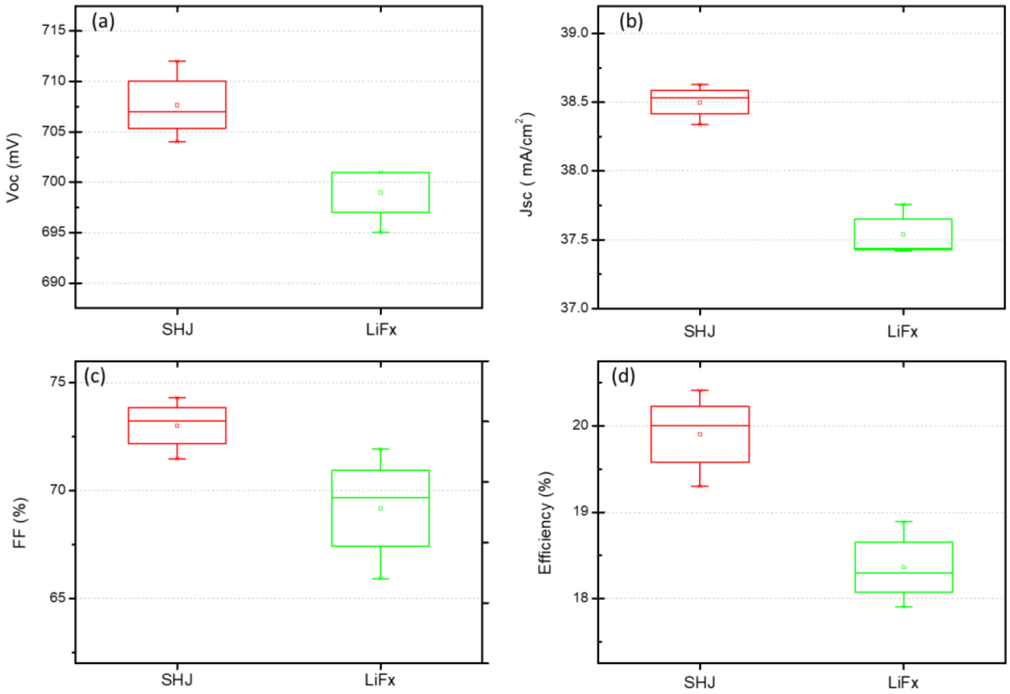

Figure 6. 27. (a) V_{OC}, (b) J_{SC}, (c) FF, and (d) η results of SHJ and ESH solar cells.

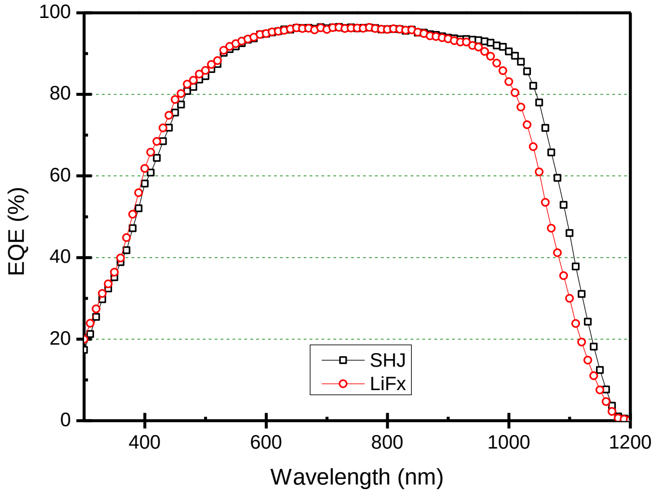

Figure 6. 28. Comparison of EQE results of HSH and SHJ solar cells.

6.3.6.3 Carrier Selective Heterocontact Solar Cell

The optimized fabrication parameters were applied to the fabrication of CSH solar cells. On the front side, two MoO_x layers with different thicknesses were used. The optimized annealing temperature and duration were used after the formation of metal contacts. The SHJ and CSH solar cell results are presented in Figure 6.29. The V_{OC} values decreased for the CSH solar cells. There was almost no difference between V_{OC} values for various thicknesses of the MoO_x layer. A significant loss was noted concerning J_{SC} values, and increasing MoO_x thickness led to a decrease in the J_{SC} value. An increase in the thickness of MoO_x led to a reduction of FF values, as discussed in the previous part. Overall, relatively low CSH solar cell efficiency values were obtained compared to SHJ solar cells. The highest efficiency achieved during this study was recorded as 17.5% for CSH solar cells.

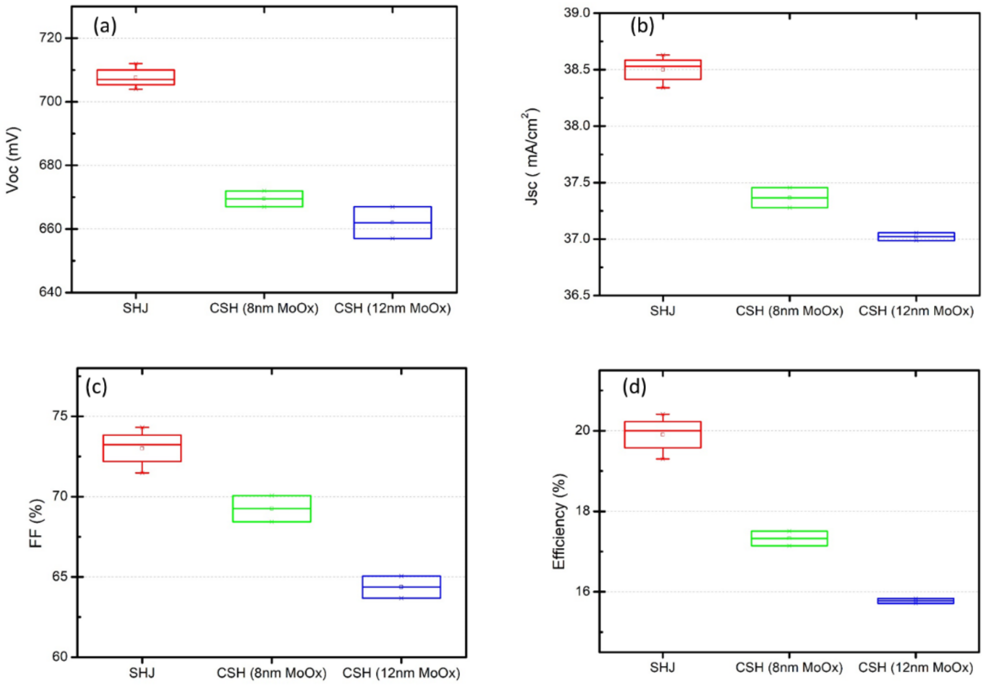

Figure 6. 29. (a) V_{OC}, (b) J_{SC}, (c) FF, and (d) η results of SHJ and CSH solar cells.

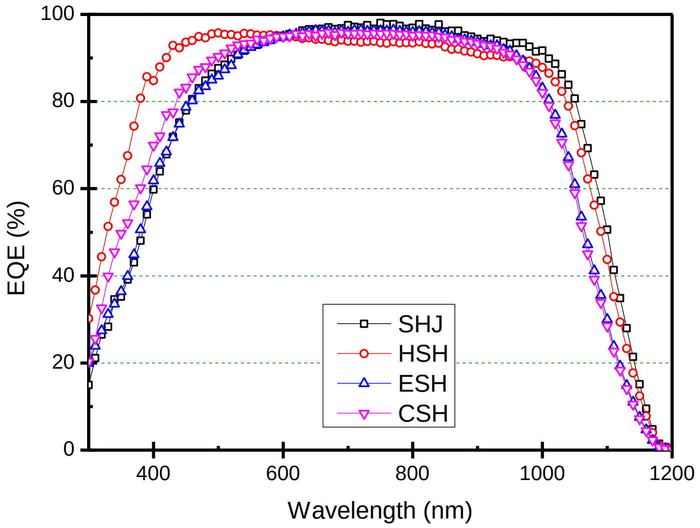

Figure 6. 30. Comparison of EQE results of all selective contact solar cells with SHJ solar cells.

In Figure 6.30, the comparison of EQE results for all different selective contact solar cells was given. There was an improvement in EQE results below 600 nm for the CSH solar cells, where spectral response decreased above 600 nm. In terms of spectral response, the efficient structure was found to be HSH solar cells. However, due to higher series resistance from the MoO_x layer and decreased passivation quality of the LiF_x/Al stack layer, the SHJ solar cell structure achieved the highest solar cell efficiency.

6.4 Conclusions

The impact of the TCO layer on solar cell parameters was clarified. It was found that the ITO layer had superiority over the AZO layer due to its optical and electrical properties. The deposition conditions of the ITO layer were a crucial step to determine its optical and electrical properties. In this study, 0.6% oxygen partial pressure was identified as the optimum deposition condition. By integrating reactive ITO sputtering, the J_{SC} value improved approximately 0.5 mA/cm^2. For over 0.6% oxygen partial pressure, the contact resistivity between ITO/Ag and c-Si/ITO increased significantly. The solvent spreading problem was strongly related to the composition of low-temperature Ag paste. Depending on the area of spread, the spectral response of solar cells could be decreased. The problem could not be fully resolved during the study. However, it was noted that reducing the spread area of the solvent drying step was crucial. After all optimization steps, the highest efficiencies achieved in SHJ solar cell structure were 20.7 and 21.2% at 170 cm^2 and 4 cm^2, respectively.

The wide band gap (p) a-SiC_x:H layer was applied to the SHJ solar cell structure. Due to the relatively high resistivity of the layer, SHJ solar cells suffered from series resistance and low FF. The highest efficiency with (p) a-SiC_x:H layer was 20.00% after optimizing the thickness.

MoO_x and LiF_x/Al layers were applied as carrier-selective contacts. It was noted that the MoO_x layer's thickness was crucial to decreasing parasitic absorption and series resistance losses. The optimum thickness was determined as 7 nm. Moreover, after forming front metal contacts for ESH solar cell structure, the annealing step has a detrimental role on the solar cell parameters. The highest solar cell efficiencies measured were: 20.5, 18.9, and 17.5% for HSH, ESH, and CSH solar cells, respectively.

CHAPTER 7

CONCLUSIONS

The relationship between solar cell parameters and thickness, emitter band gap, bulk wafer quality, and interface properties were analyzed by the AforsHet simulation program. The optimum doping concentrations of (p) a-Si:H and (n) a-Si:H were found as $5x10^{18}$ and $5x10^{17}$ cm^{-3}, respectively. Moreover, the effect of an increase in the band gap of (p) a-Si:H on SHJ solar cell performance was investigated and, the optimum band gap of the emitter layer was found as 2.0 eV. Above 2.0 eV, FF values decrease significantly due to an increase in the barrier height on the hole flow direction. Furthermore, the impact of the c-Si bulk quality on SHJ solar cell parameters was studied, and the simulation results showed that the bulk lifetime should be at least 2.5 ms or higher to achieve high-performance devices. The relation between D_{it} and passivation quality was also investigated, and it was found that D_{it} values should be lower than $1x10^{10}$ $cm^{-2}eV^{-1}$ to achieve good passivation with (i) a-Si:H layer. Finally, the impact of a-Si:H thicknesses on the device performance were studied, and the results showed that the thinner the a-Si:H, the better the SHJ solar cell performance due to a decrease in parasitic losses and improvement in FF values.

Different Si surface morphologies were studied to decrease the optical reflectance losses of solar cells. Alkaline texturing and Cu-ACE methods were analyzed and optimized. The correlation between the molarity of $Cu(NO_3)_2$ and Si surface morphology was identified, and four different and novel surface morphologies were obtained: porous-like, elliptical-shaped, IP, and star-shaped IP. The well-defined IPs are observed after 15 minutes of etching with 8 mM molarity of $Cu(NO_3)_2$, resulting in 3.74% average weighted reflectance. The impact of the molar concentration of the reductant and oxidant on the surface morphology, etching direction, and etch rate was also understood. We found that depending on the molarity of HF; the etching could behave like an isotropic etchant. The process temperature was one of the deterministic parameters on the surface morphology and pH of the solution. Next, by gradually increasing process temperature from 50°C to 55°C over 15 minutes, the novel tetragonal-star-shaped surface morphology was obtained, resulting in $R_{weighted}$ of 2.65%, the lowest spectral reflectance value obtained in the literature using this technique. Moreover, Al-BSF solar cells were fabricated on c-Si wafers with the tetragonal-star-shaped IPs and upright pyramids. The J_{SC} and efficiency values of Al-BSF Si solar cell were improved significantly with the help of tetragonal-star-shaped IPs by almost 3% compared to upright pyramids. After that, the oxidizing agent was changed from H_2O_2 to HNO_3 to enhance the controllability of the etchant. The IPs formed with the novel solution containing HNO_3, resulting in a slightly higher surface reflectivity than the previous solution. When using HNO_3, the IPs could form at 40°C, but it also enabled surface modification even at room temperature compatible surface reflectance with random pyramid texturing, resulting in around 10% weighted average reflectance. This was the first time room temperature texturing of Si with the Cu-ACE method was demonstrated.

Due to the dangling bond passivation properties, the excellent passivation quality has been achieved by (i) a-Si:H layer. For that reason, the relationship between passivation quality of (i) a-Si:H layer and film properties were studied in terms of "H" content and D_{it} as a function of various deposition conditions. The passivation quality of (i) a-Si:H layer was improved by increasing SiH_4/H_2 ratio due to a decrease in D_{it} value between c-Si and (i) a-Si:H layer. Furthermore, post-deposition HPT used after deposition of the (i) a-Si:H layer further improved passivation quality by decreasing dangling bonds at the interface and increasing "H" content of the film slightly. HPT allowed D_{it} to decreased up to 7.62×10^{10} $eV^{-1}cm^{-2}$. Moreover, the best passivation quality was obtained at 9.45% "H" content, resulting in 740 mV $_{imp}V_{oc}$ on DSP, n-type, 1-3 Ω.cm FZ wafers. Subsequently, an unexpected decrease in the passivation quality of (i) a-Si:H led us to focus on possible sources of this decrease. Firstly, the effect of the deposition holder, tweezers, and the showerhead of the PECVD system on the passivation quality was investigated. In accordance with the results, the contaminants from tweezers, the scratch problem caused by the deposition holder, and degas of thermal tape were found as some reasons for the low passivation quality. However, the lack of passivation could not be solved by the solution of these problems. Secondly, possible contaminants from wet chemical processes were traced by ToF-SIMS and ICP-MS measurements. It was detected that metallic contaminants coming from wet chemical processes have a detrimental impact on passivation quality. The reason for the metallic contaminants was found as metallic parts of the wet benches. The corrosion in the stainless steel parts of the wet benches decreased (i) a-Si:H passivation properties. At this stage, different beakers, made of PVDF and PFA, were compared in terms of contamination from wet chemical processes. Next, new and clean quartz beakers solved the contamination problem, resulting in (i) a-Si:H passivation quality over 710 mV $_{imp}V_{OC}$.

The parasitic absorption losses can be decreased by applying wide band gap materials where the optical band gap of a-SiC$_x$:H is increased up to 2.24 eV. The (i) a-SiC$_x$:H layers were fabricated by using CH$_4$ gasses under various deposition conditions. Due to the necessity of higher energy to decompose CH$_4$ molecules into radicals, the rise in power density increases E$_g$ values. The R_{H_2} and power density plays a deciding role in the decomposition of CH$_4$ molecules and resulting optical and electrical properties of the layer. Foundings showed that the H content of (i) a-SiC$_x$:H layers were lower than 5%, and the C content varied between 0.5% to 2% depending on deposition conditions. C content could be increased with an increase in deposition power. The interface quality was analyzed by conductance method, and the D$_{it}$ values were found between $1.2\text{x}10^{12}$ and $5.6\text{x}10^{12}$ eV^{-1}cm$^{-2,}$ which is a relatively high value for applying as a passivation layer. We identified the SI ratio between C and Si atoms encountered in the a-SiC$_x$:H formation as the tuning mechanism of the optical band gap and resistivity values from Tof-SIMS measurements. The preference between hydrogen bonding to the silicon or carbon atoms related to the deposition regime and the fixed charge density of the a-SiC$_x$:H layer correlated with the corporation of CH to the matrix. Moreover, SI ratios of C$^-$

$/Si^-$, $SiCH^-/SiC^-$ and CH^-/SiH^- had a significant impact on the interface in terms of passivation quality where these ratios should be decreased to achieve higher passivation quality. We found that relatively low passivation qualities were achieved with the a-SiC_x:H layers. Interface quality improved by a buffer ultra-thin (i) a-Si:H (3 nm) layer inserted between c-Si and a-SiC_x:H layer, and the highest effective lifetime value achieved in this structure was obtained as 100 µs resulting in 650 mV $_{imp}V_{oc}$.

The optical and electrical properties of doped a-Si:H layers play a crucial role in the formation of electric fields to improve carrier collection efficiency and decrease parasitic absorption losses. The impact of doping and hydrogen dilution ratios on electrical and optical properties of doped a-Si:H layers was studied. From the results, both phosphorous and boron-doped a-Si:H layers, the conductivity difference between dark and under illumination was less than one order of magnitude. From the conductivity results of (n) a-Si:H, the optimum deposition conditions for hydrogen dilution and doping ratio were determined to be 9 and 0.04, respectively, where the peak doping concentration was found to be $9.8x10^{19}$ atom/cm^{-3}. For (p) a-Si:H layer, the increase in the doping ratio led to a decrease in E_g. The largest E_g was found to be 1.68 eV obtained by $R_{B_2H_6}$ equal to 0.008. For the p-type doping, it was found that the optimum hydrogen dilution and doping ratio was 9 and 0.01, respectively, resulting in conductivity of $2.17x10^{-4}$ S/cm. For both n and p-type doped a-Si:H layer, we found that there was no direct impact of the doped a-Si:H layer on the passivation quality.

Two wide band gap materials, SiC_x:H and MoO_x, were analyzed in terms of their optical and electrical properties for the application as emitter layer in SHJ solar cells. The band gap of the emitter layer was enlarged up to 2.3 eV with the help of C incorporation to the a-Si:H matrix resulting in relatively high resistive (p) a-SiC_x:H layers. Interface properties of MoO_x with c-Si wafer passivation properties with the combination of different thicknesses of (i) a-Si:H were analyzed. It was found that the optimum thickness of (i) a-Si:H layer is 7 nm for the stack layer passivation with

MoO_x. As ESC, the properties of LiF_x, which has band gap of 13 eV, was investigated. It was concluded that LiF_x layer does not have any passivation property without any interfacial layer. When the (i) a-Si:H was inserted into the structure, it was found that the passivation quality decreased slightly compared to the structure with only (i) a-Si:H layer.

The impact of various TCO layers on SHJ solar cell parameters was investigated. It was found that the ITO layer had superiority over the AZO layer due to its optical and electrical properties. The deposition conditions of the ITO layer were a crucial step to determine parasitic absorption losses. In this study, it was found that 0.6% oxygen partial pressure was the optimum deposition condition in terms of mobility and carrier density. By the integration of reactive ITO sputtering, the J_{SC} value was improved by 0.5 mA/cm^2. Above 0.6% oxygen partial pressure, the contact resistivity between ITO/Ag and c-Si/ITO was increased significantly. Screen-printing metallization of SHJ solar cells has an impact on the shadowing losses and contribution in series resistance. During the study, SHJ solar cells were suffered from the solvent spreading problem, which was strongly related to the composition of low-temperature Ag paste and printing parameters. Depending on the spread area, the spectral response of solar cells could be decreased pretty much. The problem cannot be solved totally during the study. However, it was found that the spread area was decreased by adding a drying step before the curing of SHJ solar cells. After all optimization, the highest efficiencies achieved in SHJ solar cell structure were 20.7 and 21.2% at an area of 170 cm^2 and 4 cm^2, respectively.

The wide band gap (p) a-SiC_x:H layer was applied to the SHJ solar cell structure. Due to the relatively high resistivity of the layer, SHJ solar cells were suffered from series resistance and low FF. The highest efficiency in SHJ solar cells with (p) a-SiC_x:H emitter layer was found as 20.00% after optimization of the thickness.

MoO_x and LiF_x/Al layers were applied as carrier selective contacts. It was found that the thickness of MoO_x layer was crucial to decrease parasitic absorption and series resistance losses. The optimum thickness was found as 7 nm. Moreover, the annealing step after forming front metal contacts for ESH solar cell structure has a detrimental role on the solar cell parameters. The highest solar cell efficiencies were found as 20.5, 18.9, and 17.5% for HSH, ESH, and CSH solar cells, respectively.

REFERENCES

[1] Statistical Review of World Energy | Energy economics | Home, (n.d.). https://www.bp.com/en/global/corporate/energy-economics/statistical-review-of-world-energy.html (accessed Jul. 22, 2021).

[2] "World Energy Outlook 2020 – Analysis - IEA." https://www.iea.org/reports/world-energy-outlook-2020 (accessed Jul. 22, 2021).

[3] M. Höök and X. Tang, "Depletion of fossil fuels and anthropogenic climate change—A review," *Energy Policy*, vol. 52, pp. 797–809, Jan. 2013, doi: 10.1016/J.ENPOL.2012.10.046.

[4] "IEA World Energy Investment Report 2020 | World Coal Association." https://www.worldcoal.org/iea-world-energy-investment-report-2020/ (accessed Jul. 22, 2021).

[5] IPCC, "Climate Change 2007: Synthesis report Summary for Policymakers," *Hemisphere*, vol. 335, no. November, 2007.

[6] I. T. Baldwin *et al.*, Eds., "A History of Atmospheric CO2 and Its Effects on Plants, Animals, and Ecosystems," vol. 177, 2005, doi: 10.1007/B138533.

[7] A. J. (Arnold J. Bloom, "Global climate change : convergence of disciplines," p. 398, 2010.

[8] S. Yun *et al.*, "New-generation integrated devices based on dye-sensitized and perovskite solar cells," *Energy Environ. Sci.*, vol. 11, no. 3, pp. 476–526, Mar. 2018, doi: 10.1039/C7EE03165C.

[9] IRENA, *Renewable capacity statistics 2019*. 2019.

[10] J. Tersoff, "Schottky Barrier Heights and the Continuum of Gap States," *Phys. Rev. Lett.*, vol. 52, no. 6, p. 465, Feb. 1984, doi: 10.1103/PhysRevLett.52.465.

[11] D. M. Chapin, C. S. Fuller, and G. L. Pearson, "A new silicon p-n junction photocell for converting solar radiation into electrical power [3]," *Journal of Applied Physics*, vol. 25, no. 5. 1954, doi: 10.1063/1.1721711.

[12] "Best Research-Cell Efficiency Chart | Photovoltaic Research | NREL." https://www.nrel.gov/pv/cell-efficiency.html (accessed Sep. 28, 2021).

[13] Fraunhofer, "Fraunhofer ISE: Photovoltaics Report," *Fraunhofer ISE*, no. March, 2019.

[14] ITRPV, "International Technology Roadmap for Photovoltaic," *Itrpv*, vol. 11th Editi, no. April, 2020.

[15] N. Kouvaritakis, A. Soria, and S. Isoard, “Modelling energy technology dynamics: Methodology for adaptive expectations models with learning by doing and learning by searching,” *Int. J. Glob. Energy Issues*, vol. 14, no. 1–4, pp. 104–115, 2000, doi: 10.1504/IJGEI.2000.004384.

[16] Å. Lindman and P. Söderholm, “Wind power learning rates: A conceptual review and meta-analysis,” *Energy Econ.*, vol. 34, no. 3, pp. 754–761, May 2012, doi: 10.1016/J.ENECO.2011.05.007.

[17] M. Junginger, A. Faaij, and W. C. Turkenburg, “Global experience curves for wind farms,” *Energy Policy*, vol. 33, no. 2, pp. 133–150, Jan. 2005, doi: 10.1016/S0301-4215(03)00205-2.

[18] E. S. Rubin, M. L. Azevedo, P. Jaramillo, and S. Yeh, “A review of learning rates for electricity supply technologies,” *Energy Policy*, vol. 86, pp. 198–218, 2015, doi: 10.1016/j.enpol.2015.06.011.

[19] M. Junginger *et al.*, “Technological learning in bioenergy systems,” *Energy Policy*, vol. 34, no. 18, pp. 4024–4041, Dec. 2006, doi: 10.1016/J.ENPOL.2005.09.012.

[20] “Heterojunction Solar Technology 2019 Report | TaiyangNews.” Accessed: Jul. 24, 2021. [Online]. Available: http://taiyangnews.info/reports/heterojunction-solar-technology-2019-report/.

[21] M. Taguchi, E. Maruyama, and M. Tanaka, “Temperature Dependence of Amorphous/Crystalline Silicon Heterojunction Solar Cells,” *Jpn. J. Appl. Phys.*, vol. 47, no. 2R, p. 814, Feb. 2008, doi: 10.1143/JJAP.47.814.

[22] R. A. Street, “Hydrogenated Amorphous Silicon,” *Hydrog. Amorph. Silicon*, Aug. 1991, doi: 10.1017/CBO9780511525247.

[23] R. A. Street, “Doping and the fermi energy in amorphous silicon,” *Phys. Rev. Lett.*, vol. 49, no. 16, 1982, doi: 10.1103/PhysRevLett.49.1187.

[24] K. Okuda, H. Okamoto, and Y. Hamakawa, “Amorphous Si/polyctystalline Si Stacked Solar Cell Having more Than 12% Conversion Efficiency.,” *Japanese J. Appl. Physics, Part 2 Lett.*, vol. 22, no. 9, 1983, doi: 10.1143/jjap.22.l605.

[25] Y. Hamakawa, K. Fujimoto, K. Okuda, Y. Kashima, S. Nonomura, and H. Okamoto, “New types of high efficiency solar cells based on a-Si,” *Appl. Phys. Lett.*, vol. 43, no. 7, 1983, doi: 10.1063/1.94462.

[26] S. M. D. Nicolas, “a-Si : H/c-Si heterojunction solar cells : back side assessment and improvement,” 2012.

[27] M. Tanaka *et al.*, “Development of New a-Si/c-Si Heterojunction Solar Cells: ACJ-HIT (Artificially Constructed Junction-Heterojunction with Intrinsic

Thin-Layer)," *Jpn. J. Appl. Phys.*, vol. 31, no. 11R, p. 3518, Nov. 1992, doi: 10.1143/JJAP.31.3518.

[28] M. Taguchi *et al.*, "24.7% Record efficiency HIT solar cell on thin silicon wafer," *IEEE J. Photovoltaics*, vol. 4, no. 1, pp. 96–99, Jan. 2014, doi: 10.1109/JPHOTOV.2013.2282737.

[29] K. Masuko *et al.*, "Achievement of more than 25% conversion efficiency with crystalline silicon heterojunction solar cell," *IEEE J. Photovoltaics*, vol. 4, no. 6, pp. 1433–1435, Sep. 2014, doi: 10.1109/JPHOTOV.2014.2352151.

[30] K. Yoshikawa *et al.*, "Exceeding conversion efficiency of 26% by heterojunction interdigitated back contact solar cell with thin film Si technology," *Sol. Energy Mater. Sol. Cells*, vol. 173, pp. 37–42, Dec. 2017, doi: 10.1016/J.SOLMAT.2017.06.024.

[31] C. Buerhop, T. Pickel, M. Dalsass, H. Scheuerpflug, C. Camus, and C. J. Brabec, "AIR-PV-check: A quality inspection of PV-power plants without operation interruption," *2017 IEEE 44th Photovolt. Spec. Conf. PVSC 2017*, pp. 1752–1754, 2017, doi: 10.1109/PVSC.2017.8366365.

[32] J. Zhao *et al.*, "24% Silicon Heterojunction Solar Cells on Meyer Burger's on Mass Production Tools and How Wafer Material Impacts Cell Parameters," *2018 IEEE 7th World Conf. Photovolt. Energy Conversion, WCPEC 2018 - A Jt. Conf. 45th IEEE PVSC, 28th PVSEC 34th EU PVSEC*, pp. 1514–1519, Nov. 2018, doi: 10.1109/PVSC.2018.8547908.

[33] G. Condorelli *et al.*, "Initial Results of Enel Green Power Silicon Heterojunction Factory and Strategies for Improvements," *Conf. Rec. IEEE Photovolt. Spec. Conf.*, vol. 2020-June, pp. 1702–1705, Jun. 2020, doi: 10.1109/PVSC45281.2020.9300806.

[34] "25.11% efficiency silicon heterojunction solar cell with low deposition rate intrinsic amorphous silicon buffer layers - ScienceDirect." https://www.sciencedirect.com/science/article/pii/S0927024820302464?via%3Dihub (accessed Jul. 28, 2021).

[35] "25% Efficiency For Heterojunction Solar Cell | TaiyangNews." http://taiyangnews.info/technology/25-efficiency-for-heterojunction-solar-cell/ (accessed Jul. 30, 2021).

[36] "LONGi toasts new p-type TOPCon and commercial heterojunction cell efficiency records - PV Tech." https://www.pv-tech.org/longi-toasts-new-p-type-topcon-and-commercial-heterojunction-cell-efficiency-records/ (accessed Jul. 30, 2021).

[37] A. Tomasi *et al.*, "Simple processing of back-contacted silicon heterojunction solar cells using selective-area crystalline growth," *Nat. Energy 2017 25*, vol. 2, no. 5, pp. 1–8, Apr. 2017, doi: 10.1038/nenergy.2017.62.

[38] A. Tomasi *et al.*, “Back-contacted silicon heterojunction solar cells with efficiency >21%,” *IEEE J. Photovoltaics*, vol. 4, no. 4, pp. 1046–1054, 2014, doi: 10.1109/JPHOTOV.2014.2320586.

[39] J. Nakamura, N. Asano, T. Hieda, C. Okamoto, H. Katayama, and K. Nakamura, “Development of heterojunction back contact Si solar cells,” *IEEE J. Photovoltaics*, vol. 4, no. 6, pp. 1491–1495, 2014, doi: 10.1109/JPHOTOV.2014.2358377.

[40] M. Xu, “Lithography-free a-Si : H patterning methods for silicon heterojunction interdigitated back-contact solar cells,” no. December 2018, 2018.

[41] S. Y. Herasimenka, C. J. Tracy, W. J. Dauksher, C. B. Honsberg, and S. Bowden, “A simplified process flow for silicon heterojunction interdigitated back contact solar cells: Using shadow masks and tunnel junctions,” *2014 IEEE 40th Photovolt. Spec. Conf. PVSC 2014*, pp. 2486–2490, Oct. 2014, doi: 10.1109/PVSC.2014.6925434.

[42] H. S. Radhakrishnan *et al.*, “Simplified rear-side patterning for silicon heterojunction IBC solar cells: Development of the in situ ‘nano-envelope’ dry clean,” *2018 IEEE 7th World Conf. Photovolt. Energy Conversion, WCPEC 2018 - A Jt. Conf. 45th IEEE PVSC, 28th PVSEC 34th EU PVSEC*, pp. 1520–1523, Nov. 2018, doi: 10.1109/PVSC.2018.8548143.

[43] E. Simoen *et al.*, “Dry etch damage in n-type crystalline silicon wafers assessed by deep-level transient spectroscopy and minority carrier lifetime,” *J. Vac. Sci. Technol. B, Nanotechnol. Microelectron. Mater. Process. Meas. Phenom.*, vol. 36, no. 4, p. 041201, Jun. 2018, doi: 10.1116/1.5026529.

[44] J. Zhou, “Fabrication of Silicon Heterojunction Interdigitated Back-contacted (SHJ-IBC) solar cells,” p. 61, 2017.

[45] S. Ring *et al.*, “Emitter Patterning for Back-Contacted Si Heterojunction Solar Cells Using Laser Written Mask Layers for Etching and Self-Aligned Passivation (LEAP),” *IEEE J. Photovoltaics*, vol. 6, no. 4, pp. 894–899, Jul. 2016, doi: 10.1109/JPHOTOV.2016.2566882.

[46] D. Thibaut *et al.*, “Development of Interdigitated Back Contact Silicon Heterojunction (IBC Si-HJ) Solar Cells,” *Energy Procedia*, vol. 8, pp. 294–300, Jan. 2011, doi: 10.1016/J.EGYPRO.2011.06.139.

[47] D. Stüwe, D. Mager, D. Biro, and J. G. Korvink, “Inkjet Technology for Crystalline Silicon Photovoltaics,” *Adv. Mater.*, vol. 27, no. 4, pp. 599–626, Jan. 2015, doi: 10.1002/ADMA.201403631.

[48] T. Desrues, S. De Vecchi, F. Souche, D. Munoz, and P. J. Ribeyron, “SLASH concept: A novel approach for simplified interdigitated back contact solar cells fabrication,” *Conf. Rec. IEEE Photovolt. Spec. Conf.*, pp. 1602–1605,

2012, doi: 10.1109/PVSC.2012.6317901.

[49] M. Mikolášek *et al.*, “Capacitance study of carrier inversion at the amorphous/crystalline silicon heterojunction passivated by different thicknesses of i-layer,” *Appl. Surf. Sci.*, vol. 312, pp. 152–156, Sep. 2014, doi: 10.1016/J.APSUSC.2014.03.187.

[50] R. Stangl, C. Leendertz, and J. Haschke, “Numerical Simulation of Solar Cells and Solar Cell Characterization Methods: the Open-Source on Demand Program AFORS-HET,” *Sol. Energy*, Feb. 2010, doi: 10.5772/8073.

[51] R. Stangl, M. Kriegel, and M. Schmidt, “AFORS-HET, version 2.2, a numerical computer program for simulation of heterojunction solar cells and measurements,” *Conf. Rec. 2006 IEEE 4th World Conf. Photovolt. Energy Conversion, WCPEC-4*, vol. 2, pp. 1350–1353, 2006, doi: 10.1109/WCPEC.2006.279681.

[52] W. G.J.H.M. van Sark, L. Korte, and F. Roca (Eds.), *Physics and Technology of Amorphous-Crystalline Heterostructure Silicon Solar Cells*, vol. 53, no. 9. 1981.

[53] W. Shockley and J. W. T. Read, “Statistics of the Recombinations of Holes and Electrons,” *Phys. Rev.*, vol. 87, no. 5, p. 835, Sep. 1952, doi: 10.1103/PhysRev.87.835.

[54] R. N. Hall, “Electron-Hole Recombination in Germanium,” *Phys. Rev.*, vol. 87, no. 2, p. 387, Jul. 1952, doi: 10.1103/PhysRev.87.387.

[55] X. Wen, X. Zeng, W. Liao, Q. Lei, and S. Yin, “An approach for improving the carriers transport properties of a-Si:H/c-Si heterojunction solar cells with efficiency of more than 27%,” *Sol. Energy*, vol. 96, pp. 168–176, Oct. 2013, doi: 10.1016/J.SOLENER.2013.07.019.

[56] J. Meerwijk, “Analysis of electronic transport in HIT solar cells,” 2012.

[57] U. Gangopadhyay, “Comparative simulation study between n- type and p-type Silicon Solar Cells and the variation of efficiency of n- type Solar Cell by the application of passivation layer with different thickness using AFORS HET and PC1D.,” *IOSR J. Eng.*, vol. 02, no. 08, pp. 41–48, Aug. 2012, doi: 10.9790/3021-02814148.

[58] T. F. Schulze, H. N. Beushausen, C. Leendertz, A. Dobrich, B. Rech, and L. Korte, “Interplay of amorphous silicon disorder and hydrogen content with interface defects in amorphous/crystalline silicon heterojunctions,” *Appl. Phys. Lett.*, vol. 96, no. 25, p. 252102, Jun. 2010, doi: 10.1063/1.3455900.

[59] M. Moreno *et al.*, “A comparative study of wet and dry texturing processes of c-Si wafers for the fabrication of solar cells,” *Sol. Energy*, vol. 101, pp. 182–191, Mar. 2014, doi: 10.1016/j.solener.2014.01.004.

[60] S. C. Baker-Finch and K. R. McIntosh, “Reflection distributions of textured monocrystalline silicon: Implications for silicon solar cells,” *Prog. Photovoltaics Res. Appl.*, vol. 21, no. 5, pp. 960–971, Aug. 2013, doi: 10.1002/pip.2186.

[61] D. H. Macdonald *et al.*, “Texturing industrial multicrystalline silicon solar cells,” *Sol. Energy*, vol. 76, no. 1–3, pp. 277–283, Jan. 2004, doi: 10.1016/j.solener.2003.08.019.

[62] D. Zhang *et al.*, “Design and fabrication of a SiOx/ITO double-layer anti-reflective coating for heterojunction silicon solar cells,” *Sol. Energy Mater. Sol. Cells*, vol. 117, pp. 132–138, Oct. 2013, doi: 10.1016/j.solmat.2013.05.044.

[63] T. H. Fung *et al.*, “Improved emitter performance of RIE black silicon through the application of in-situ oxidation during POCl3 diffusion,” *Sol. Energy Mater. Sol. Cells*, vol. 210, p. 110480, Jun. 2020, doi: 10.1016/j.solmat.2020.110480.

[64] J. Yoo, G. Yu, and J. Yi, “Black surface structures for crystalline silicon solar cells,” *Mater. Sci. Eng. B Solid-State Mater. Adv. Technol.*, vol. 159–160, no. C, pp. 333–337, Mar. 2009, doi: 10.1016/j.mseb.2008.10.019.

[65] M. Halbwax *et al.*, “Micro and nano-structuration of silicon by femtosecond laser: Application to silicon photovoltaic cells fabrication,” *Thin Solid Films*, vol. 516, no. 20, pp. 6791–6795, Aug. 2008, doi: 10.1016/j.tsf.2007.12.117.

[66] L. L. Ma *et al.*, “Wide-band ‘black silicon’ based on porous silicon,” *Appl. Phys. Lett.*, vol. 88, no. 17, p. 171907, Apr. 2006, doi: 10.1063/1.2199593.

[67] H. Han, Z. Huang, and W. Lee, “Metal-assisted chemical etching of silicon and nanotechnology applications,” *Nano Today*, vol. 9, no. 3. Elsevier B.V., pp. 271–304, Jun. 01, 2014, doi: 10.1016/j.nantod.2014.04.013.

[68] M. Otto *et al.*, “Black silicon photovoltaics,” *Advanced Optical Materials*, vol. 3, no. 2. Wiley-VCH Verlag, pp. 147–164, Feb. 01, 2015, doi: 10.1002/adom.201400395.

[69] C. H. Hsu, J. R. Wu, Y. T. Lu, D. J. Flood, A. R. Barron, and L. C. Chen, “Fabrication and characteristics of black silicon for solar cell applications: An overview,” *Materials Science in Semiconductor Processing*, vol. 25. Elsevier Ltd, pp. 2–17, Sep. 01, 2014, doi: 10.1016/j.mssp.2014.02.005.

[70] P. Repo *et al.*, “Effective passivation of black silicon surfaces by atomic layer deposition,” *IEEE J. Photovoltaics*, vol. 3, no. 1, pp. 90–94, 2013, doi: 10.1109/JPHOTOV.2012.2210031.

[71] K. Peng *et al.*, “Metal-particle-induced, highly localized site-specific etching of Si and formation of single-crystalline Si nanowires in aqueous fluoride solution,” *Chem. - A Eur. J.*, vol. 12, no. 30, pp. 7942–7947, Oct. 2006, doi:

10.1002/chem.200600032.

[72] K. Q. Peng, X. Wang, and S. T. Lee, “Gas sensing properties of single crystalline porous silicon nanowires,” *Appl. Phys. Lett.*, vol. 95, no. 24, p. 243112, Dec. 2009, doi: 10.1063/1.3275794.

[73] Z. G. Hu *et al.*, “The high cycling performance of ultra-thin Si nanowires fabricated by metal-assisted chemical etching method as lithium-ion batteries anode,” *J. Electroanal. Chem.*, vol. 878, p. 114567, Dec. 2020, doi: 10.1016/j.jelechem.2020.114567.

[74] C. Huo *et al.*, “Metal-Assisted Chemical Etching of Silicon in Oxidizing HF Solutions: Origin, Mechanism, Development, and Black Silicon Solar Cell Application,” *Advanced Functional Materials*, vol. 30, no. 52. Wiley-VCH Verlag, p. 2005744, Dec. 01, 2020, doi: 10.1002/adfm.202005744.

[75] Z. Huang, N. Geyer, P. Werner, J. De Boor, and U. Gösele, “Metal-assisted chemical etching of silicon: A review,” *Advanced Materials*, vol. 23, no. 2. John Wiley & Sons, Ltd, pp. 285–308, Jan. 11, 2011, doi: 10.1002/adma.201001784.

[76] M. A. Green, “The path to 25% silicon solar cell efficiency: History of silicon cell evolution,” *Prog. Photovoltaics Res. Appl.*, vol. 17, no. 3, pp. 183–189, May 2009, doi: 10.1002/pip.892.

[77] Y. Wang *et al.*, “Maskless inverted pyramid texturization of silicon,” *Sci. Rep.*, vol. 5, no. 1, pp. 1–6, Jun. 2015, doi: 10.1038/srep10843.

[78] Y. Wang, Y. Liu, L. Yang, W. Chen, X. Du, and A. Kuznetsov, “Micro-structured inverted pyramid texturization of Si inspired by self-assembled Cu nanoparticles,” *Nanoscale*, vol. 9, no. 2, pp. 907–914, Jan. 2017, doi: 10.1039/c6nr08126f.

[79] Y. Zhao *et al.*, “Regulation of surface texturization through copper-assisted chemical etching for silicon solar cells,” *Sol. Energy*, vol. 201, pp. 461–468, May 2020, doi: 10.1016/j.solener.2020.03.013.

[80] L. Yang *et al.*, “18.87%-efficient inverted pyramid structured silicon solar cell by one-step Cu-assisted texturization technique,” *Sol. Energy Mater. Sol. Cells*, vol. 166, pp. 121–126, Jul. 2017, doi: 10.1016/j.solmat.2017.03.017.

[81] M. K. Basher, R. Mishan, S. Biswas, M. Khalid Hossain, M. A. R. Akand, and M. A. Matin, “Study and analysis the Cu nanoparticle assisted texturization forming low reflective silicon surface for solar cell application,” *AIP Adv.*, vol. 9, no. 7, p. 2572, Jul. 2019, doi: 10.1063/1.5109003.

[82] E. Lie and T. Welander, “Influence of dissolved oxygen and oxidation-reduction potential on the denitrification rate of activated sludge,” in *Water Science and Technology*, Sep. 1994, vol. 30, no. 6 pt 6, pp. 91–100, doi: 10.2166/wst.1994.0256.

[83] R. Akan, K. Parfeniukas, C. Vogt, M. S. Toprak, and U. Vogt, “Reaction control of metal-assisted chemical etching for silicon-based zone plate nanostructures,” *RSC Adv.*, vol. 8, no. 23, pp. 12628–12634, Apr. 2018, doi: 10.1039/c8ra01627e.

[84] S. Kwon, J. Yi, S. Yoon, J. S. Lee, and D. Kim, “Effects of textured morphology on the short circuit current of single crystalline silicon solar cells: Evaluation of alkaline wet-texture processes,” *Curr. Appl. Phys.*, vol. 9, no. 6, pp. 1310–1314, Nov. 2009, doi: 10.1016/j.cap.2008.12.014.

[85] A. J. Ellis, “823. The effect of temperature on the ionization of hydrofluoric acid,” *J. Chem. Soc.*, no. 0, pp. 4300–4304, Jan. 1963, doi: 10.1039/JR9630004300.

[86] A. H. S. K. Jäger, O. Isabella, and R. A. van S. Miro, *Solar Energy The physics and engineering of photovoltaic conversion, technologies and systems*, vol. 20. 2012.

[87] S. DeWolf, A. Descoeudres, Z. C. Holman, and C. Ballif, “High-efficiency silicon heterojunction solar cells: A review,” *Green*, vol. 2, no. 1. Walter de Gruyter GmbH, pp. 7–24, 2012, doi: 10.1515/green-2011-0018.

[88] H. J. Park *et al.*, “Passivation quality control in poly-Si/SiOx/c-Si passivated contact solar cells with 734 mV implied open circuit voltage,” *Sol. Energy Mater. Sol. Cells*, vol. 189, pp. 21–26, Jan. 2019, doi: 10.1016/j.solmat.2018.09.013.

[89] K. Gotoh *et al.*, “Hydrogen concentration at a-Si:H/c-Si heterointerfaces - The impact of deposition temperature on passivation performance,” *AIP Adv.*, vol. 9, no. 7, p. 075115, Jul. 2019, doi: 10.1063/1.5100086.

[90] J. Chen *et al.*, “Establishment of a novel functional group passivation system for the surface engineering of c-Si solar cells,” *Sol. Energy Mater. Sol. Cells*, vol. 195, pp. 99–105, Jun. 2019, doi: 10.1016/j.solmat.2019.02.039.

[91] A. B. Gougam, B. Rajab, and A. Bin Afif, “Investigation of c-Si surface passivation using thermal ALD deposited HfO 2 films,” *Mater. Sci. Semicond. Process.*, vol. 95, pp. 42–47, Jun. 2019, doi: 10.1016/j.mssp.2019.02.012.

[92] L. Korte, E. Conrad, H. Angermann, R. Stangl, and M. Schmidt, “Advances in a-Si:H/c-Si heterojunction solar cell fabrication and characterization,” *Sol. Energy Mater. Sol. Cells*, vol. 93, no. 6–7, pp. 905–910, Jun. 2009, doi: 10.1016/J.SOLMAT.2008.10.020.

[93] “Ultraclean Surface Processing of Silicon Wafers,” *Ultraclean Surf. Process. Silicon Wafers*, 1998, doi: 10.1007/978-3-662-03535-1.

[94] H. Lignier, E. Picard, and S. Dubois, “Controlling surface contamination issues in the fabrication environment of high efficiency crystalline silicon-based homojunction solar cells,” *Energy Procedia*, vol. 124, pp. 745–751,

Sep. 2017, doi: 10.1016/J.EGYPRO.2017.09.078.

[95] Y. Noguchi and T. Nagase, “Amorphous Silicon Carbide / Crystalline Silicon Heterojunction Solar Cells : A Comprehensive Study of the Photocarrier Collection.”

[96] E. Dönerçark, “Surface preparation passivation and patterning techniques used in silicon based heterojunction solar cells,” Middle East Technical University, 2017.

[97] M. Boccard and Z. C. Holman, “Amorphous silicon carbide passivating layers for crystalline-silicon-based heterojunction solar cells,” *J. Appl. Phys.*, vol. 118, no. 6, p. 065704, Aug. 2015, doi: 10.1063/1.4928203.

[98] A. Descoeudres *et al.*, “Improved amorphous/crystalline silicon interface passivation by hydrogen plasma treatment,” *Appl. Phys. Lett.*, vol. 99, no. 12, p. 123506, Sep. 2011, doi: 10.1063/1.3641899.

[99] A. H. M. Smets, W. M. M. Kessels, and M. C. M. van de Sanden, “The effect of ion-surface and ion-bulk interactions during hydrogenated amorphous silicon deposition,” *J. Appl. Phys.*, vol. 102, no. 7, p. 073523, Oct. 2007, doi: 10.1063/1.2786873.

[100] L. Zhang *et al.*, “Investigation of positive roles of hydrogen plasma treatment for interface passivation based on silicon heterojunction solar cells,” *J. Phys. D. Appl. Phys.*, vol. 49, no. 16, p. 165305, Mar. 2016, doi: 10.1088/0022-3727/49/16/165305.

[101] C. Madumelu *et al.*, “Investigation of light-induced degradation in N-Type silicon heterojunction solar cells during illuminated annealing at elevated temperatures,” *Sol. Energy Mater. Sol. Cells*, vol. 218, Dec. 2020, doi: 10.1016/j.solmat.2020.110752.

[102] E. Kobayashi *et al.*, “Light-induced performance increase of silicon heterojunction solar cells,” *Appl. Phys. Lett.*, vol. 109, no. 15, p. 153503, Oct. 2016, doi: 10.1063/1.4964835.

[103] M. Ohsawa *et al.*, “The role of hydrogen in the Staebler-Wronski effect of a-si:H,” *Jpn. J. Appl. Phys.*, vol. 24, no. 10, pp. L838–L840, 1985, doi: 10.1143/JJAP.24.L838.

[104] H. Dersch, J. Stuke, and J. Beichler, “Light-induced dangling bonds in hydrogenated amorphous silicon,” *Appl. Phys. Lett.*, vol. 38, no. 6, pp. 456–458, 1981, doi: 10.1063/1.92402.

[105] A. V. Shah, *Thin-film silicon solar cells*. 2010.

[106] E. Donercark, S. Guler, E. H. Ciftpinar, I. Kabacelik, and R. Turan, “Enhanced Passivation Properties of a-Si:H and Reactive ITO Sputtering for SHJ Solar Cells,” in *Conference Record of the IEEE Photovoltaic Specialists*

Conference, Jun. 2020, vol. 2020-June, pp. 2308–2312, doi: 10.1109/PVSC45281.2020.9300669.

[107] P. M. Kaminski, A. Abbas, K. Bass, and G. Claudio, “Passivation of silicon wafers by Silicon Carbide (SiC x) thin film grown by sputtering,” in *Energy Procedia*, Jan. 2011, vol. 10, pp. 71–75, doi: 10.1016/j.egypro.2011.10.155.

[108] Z. Yu, I. Pereyra, and M. N. P. Carreno, “Wide optical band gap window layers for solar cells,” *Sol. Energy Mater. Sol. Cells*, vol. 66, no. 1–4, pp. 155–162, Feb. 2001, doi: 10.1016/S0927-0248(00)00168-9.

[109] R. Saleh, L. Munisa, and W. Beyer, “The diffusion of hydrogen and inert gas in sputtered a-SiC:H alloys: Microstructure study,” *Sol. Energy Mater. Sol. Cells*, vol. 90, no. 18–19, pp. 3449–3455, Nov. 2006, doi: 10.1016/j.solmat.2006.04.013.

[110] O. Maslova, “Capacitance spectroscopy in hydrogenated amorphous silicon Schottky diodes and high efficiency silicon heterojunction solar cells,” *undefined*, 2013.

[111] H. García *et al.*, “Electrical Characterization of Amorphous Silicon MIS-Based Structures for HIT Solar Cell Applications,” 2016, doi: 10.1186/s11671-016-1545-z.

[112] A. Descoeudres *et al.*, “Improved amorphous/crystalline silicon interface passivation by hydrogen plasma treatment,” *Appl. Phys. Lett.*, vol. 99, no. 12, p. 123506, Sep. 2011, doi: 10.1063/1.3641899.

[113] M. Mews, T. F. Schulze, N. Mingirulli, and L. Korte, “Hydrogen plasma treatments for passivation of amorphous-crystalline silicon-heterojunctions on surfaces promoting epitaxy,” *Appl. Phys. Lett.*, vol. 102, no. 12, p. 122106, Mar. 2013, doi: 10.1063/1.4798292.

[114] S. De Wolf, B. Demaurex, A. Descoeudres, and C. Ballifécole, “Very fast light-induced degradation of a-Si:H/c-Si(100) interfaces,” *Phys. Rev. B*, vol. 83, p. 233301, 2011, doi: 10.1103/PhysRevB.83.233301.

[115] A. Tabata, M. Kuroda, M. Mori, T. Mizutani, and Y. Suzuoki, “Band gap control of hydrogenated amorphous silicon carbide films prepared by hot-wire chemical vapor deposition,” in *Journal of Non-Crystalline Solids*, Jun. 2004, vol. 338–340, no. 1 SPEC. ISS., pp. 521–524, doi: 10.1016/j.jnoncrysol.2004.03.033.

[116] A. A. Langford, M. L. Fleet, B. P. Nelson, W. A. Lanford, and N. Maley, “Infrared absorption strength and hydrogen content of hydrogenated amorphous silicon,” *Phys. Rev. B*, vol. 45, no. 23, p. 13367, Jun. 1992, doi: 10.1103/PhysRevB.45.13367.

[117] A. S. Lenshin, V. M. Kashkarov, P. V. Seredin, Y. M. Spivak, and V. A. Moshnikov, “XANES and IR spectroscopy study of the electronic structure

and chemical composition of porous silicon on n- and p-type substrates," *Semicond. 2011 459*, vol. 45, no. 9, pp. 1183–1188, Sep. 2011, doi: 10.1134/S1063782611090168.

[118] U. Kroll, J. Meier, A. Shah, S. Mikhailov, and J. Weber, "Hydrogen in amorphous and microcrystalline silicon films prepared by hydrogen dilution," *J. Appl. Phys.*, vol. 80, no. 9, p. 4971, Aug. 1998, doi: 10.1063/1.363541.

[119] H. H. Wieder, "MOS (Metal Oxide Semiconductors) Physics and Technology by E. H. Nicollian and J. R. Brews," *J. Vac. Sci. Technol.*, 1982, doi: 10.1116/1.571867.

[120] B. Tataroğlu, Ş. Altindal, and A. Tataroğlu, "The C-V-f and G/ω-V-f characteristics of Al/SiO2/p-Si (MIS) structures," *Microelectron. Eng.*, vol. 83, no. 10, pp. 2021–2026, Oct. 2006, doi: 10.1016/j.mee.2006.04.002.

[121] Z. Zolnai *et al.*, "Room temperature micro-photoluminescence measurements for monitoring defects in low-energy high-dose As and B implanted silicon," *ASMC (Advanced Semicond. Manuf. Conf. Proc.*, vol. 2021-May, May 2021, doi: 10.1109/ASMC51741.2021.9435658.

[122] "Metallic Impurities in Mono and Multi-crystalline Silicon and Their Gettering by Phosphorus Diffusion," *ECS Meet. Abstr.*, 2008, doi: 10.1149/ma2008-02/26/1995.

[123] J. Tauc, "Optical Properties of Amorphous Semiconductors," in *Amorphous and Liquid Semiconductors*, Springer US, 1974, pp. 159–220.

[124] A. Belfar, "Simulation study of the a-Si: H/nc-Si: H solar cells performance sensitivity to the TCO work function, the band gap and the thickness of i-a-Si: H absorber layer," *Sol. Energy*, vol. 114, pp. 408–417, Apr. 2015, doi: 10.1016/j.solener.2015.02.010.

[125] W. Beyer and H. Mell, "Composition and thermal stability of glow-discharge a-SiC:H and a-Si:N:H alloys.," *Disord Semicond*, pp. 641–658, 1987, doi: 10.1007/978-1-4613-1841-5_68.

[126] S. Janz geb in Leoben, "Amorphous Silicon Carbide for Photovoltaic Applications," 2007.

[127] Y. H. Wang, J. Lin, and C. H. A. Huan, "Multiphase structure of hydrogenated amorphous silicon carbide thin films," *Mater. Sci. Eng. B Solid-State Mater. Adv. Technol.*, vol. 95, no. 1, pp. 43–50, Jul. 2002, doi: 10.1016/S0921-5107(02)00204-0.

[128] G. Ambrosone, P. Capezzuto, S. Catalanotti, U. Coscia, and S. Mormone, "Philosophical Magazine B Optical, electrical and structural properties of hydrogenated amorphous Si-C alloys deposited by different hydrocarbon gas mixtures," 2009, doi: 10.1080/13642810008209757.

[129] W. L. Lin, H. K. Tsai, S. C. Lee, W. J. Sah, and W. J. Tzeng, "Identification of infrared absorption peaks of amorphous silicon-carbon alloy by thermal annealing," *Appl. Phys. Lett.*, vol. 51, no. 25, pp. 2112–2114, Dec. 1987, doi: 10.1063/1.98963.

[130] M. Li, L. Jiang, Y. Sun, T. Xiao, P. Xiang, and X. Tan, "Silicon content influence on structure and photoluminescence properties of carbon rich hydrogenated amorphous silicon carbide thin films," *J. Alloys Compd.*, vol. 753, pp. 320–328, Jul. 2018, doi: 10.1016/j.jallcom.2018.04.226.

[131] U. Kroll,) J Meier, A. Shah, S. Mikhailov, and J. Weber, "Hydrogen in amorphous and microcrystalline silicon films prepared by hydrogen dilution," 1996. Accessed: Mar. 28, 2021. [Online]. Available: http://ojps.aip.org/japo/japcr.jsp.

[132] M. M. Kamble *et al.*, "Hydrogenated Silicon Carbide Thin Films Prepared with High Deposition Rate by Hot Wire Chemical Vapor Deposition Method," *J. Coatings*, vol. 2014, pp. 1–11, Feb. 2014, doi: 10.1155/2014/905903.

[133] M. Mews, T. F. Schulze, N. Mingirulli, and L. Korte, "Hydrogen plasma treatments for passivation of amorphous-crystalline silicon-heterojunctions on surfaces promoting epitaxy," *Appl. Phys. Lett.*, vol. 102, no. 12, p. 122106, Mar. 2013, doi: 10.1063/1.4798292.

[134] D. K. Simon, P. M. Jordan, T. Mikolajick, and I. Dirnstorfer, "On the Control of the Fixed Charge Densities in Al 2 O 3-Based Silicon Surface Passivation Schemes," 2015, doi: 10.1021/acsami.5b06606.

[135] W. K. Choi, L. J. Han, and F. L. Loo, "Electrical characterization of radio frequency sputtered hydrogenated amorphous silicon carbide films," *J. Appl. Phys.*, vol. 81, no. 1, pp. 276–280, Jan. 1997, doi: 10.1063/1.363845.

[136] M. M. Rahman *et al.*, "Analysis of the Amorphous Silicon Carbide/Crystalline Silicon Interface," *MRS Proc.*, vol. 192, 1990, doi: 10.1557/proc-192-213.

[137] F. Demichelis, F. Giorgis, C. F. Pirri, E. Tresso, G. Amato, and U. Coscia, "Density of gap states in a-SiC:H films by means of photoconductive and photothermal spectroscopies," *Phys. B Phys. Condens. Matter*, vol. 205, no. 2, pp. 169–174, Feb. 1995, doi: 10.1016/0921-4526(94)00233-L.

[138] M. A. Ouadfel *et al.*, "SIMS and auger investigation of thin a-SiC and a-SiC:H films by Up-Down sputtering DC magnetron, impact on optical properties," Dec. 2014, doi: 10.1109/NAWDMPV.2014.6997619.

[139] Z. Deniz Eygi, U. Das, S. Hegedus, and R. Birkmire, "Optimizing emitter-buffer layer stack thickness for p-type silicon heterojunction solar cells," in *Journal of Renewable and Sustainable Energy*, 2013, vol. 5, no. 1, doi:

10.1063/1.4792510.

[140] S. Y. Lee *et al.*, “Analysis of a-Si:H/TCO contact resistance for the Si heterojunction back-contact solar cell,” *Sol. Energy Mater. Sol. Cells*, vol. 120, no. PART A, 2014, doi: 10.1016/j.solmat.2013.06.026.

[141] A. Chen and K. Zhu, “Computer simulation of a-Si/c-Si heterojunction solar cell with high conversion efficiency,” *Sol. Energy*, vol. 86, no. 1, 2012, doi: 10.1016/j.solener.2011.10.015.

[142] M. Vaněček, J. Kočka, J. Stuchlík, Z. Kožíšek, O. Štika, and A. Tříska, “Density of the gap states in undoped and doped glow discharge a-Si:H,” *Sol. Energy Mater.*, vol. 8, no. 4, 1983, doi: 10.1016/0165-1633(83)90006-0.

[143] C. Battaglia *et al.*, “Hole selective MoOx contact for silicon solar cells,” *Nano Lett.*, vol. 14, no. 2, 2014, doi: 10.1021/nl404389u.

[144] Y. Wan *et al.*, “Conductive and Stable Magnesium Oxide Electron-Selective Contacts for Efficient Silicon Solar Cells,” *Adv. Energy Mater.*, vol. 7, no. 5, 2017, doi: 10.1002/aenm.201601863.

[145] J. Bullock *et al.*, “Efficient silicon solar cells with dopant-free asymmetric heterocontacts,” *Nat. Energy*, vol. 1, no. 3, 2016, doi: 10.1038/nenergy.2015.31.

[146] Y. Wan *et al.*, “Magnesium Fluoride Electron-Selective Contacts for Crystalline Silicon Solar Cells,” *ACS Appl. Mater. Interfaces*, vol. 8, no. 23, 2016, doi: 10.1021/acsami.6b03599.

[147] X. Xu *et al.*, “Chemical Bath Deposition of p-Type Transparent, Highly Conducting (CuS)x:(ZnS)1-x Nanocomposite Thin Films and Fabrication of Si Heterojunction Solar Cells,” *Nano Lett.*, vol. 16, no. 3, 2016, doi: 10.1021/acs.nanolett.5b05124.

[148] D. Zielke, A. Pazidis, F. Werner, and J. Schmidt, “Organic-silicon heterojunction solar cells on n-type silicon wafers: The BackPEDOT concept,” *Sol. Energy Mater. Sol. Cells*, vol. 131, 2014, doi: 10.1016/j.solmat.2014.05.022.

[149] D. S. Frolov, G. E. Yakovlev, and V. I. Zubkov, “Technique for the Electrochemical Capacitance–Voltage Profiling of Heavily Doped Structures with a Sharp Doping Profile,” *Semicond. 2019 532*, vol. 53, no. 2, pp. 268–272, Apr. 2019, doi: 10.1134/S1063782619020076.

[150] K. Carstens and M. Dahlinger, “Surface passivation of heavily boron or phosphorus doped crystalline silicon utilizing amorphous silicon,” *J. Appl. Phys.*, vol. 119, no. 18, 2016, doi: 10.1063/1.4948945.

[151] Arghavan Salimi, “Analysis of Boron Doped Hydrogenated Amorphous Silicon Carbide Thin Film for Silicon Heterojunction Solar Cells,” Middle

East Technical University, 2019.

[152] H. Nasser *et al.*, "On the application of hole-selective MoOx as full-area rear contact for industrial scale p-type c-Si solar cells," *Prog. Photovoltaics Res. Appl.*, vol. 29, no. 3, pp. 281–293, Mar. 2021, doi: 10.1002/PIP.3363.

[153] "Huasun achieves 25.26% efficiency for heterojunction solar cell – pv magazine International." https://www.pv-magazine.com/2021/07/13/huasun-achieves-25-26-efficiency-for-heterojunction-solar-cell/ (accessed Sep. 18, 2021).

[154] X. Ru *et al.*, "25.11% efficiency silicon heterojunction solar cell with low deposition rate intrinsic amorphous silicon buffer layers," *Sol. Energy Mater. Sol. Cells,* vol. 215, p. 110643, Sep. 2020, doi: 10.1016/J.SOLMAT.2020.110643.

[155] D. Adachi, J. L. Hernández, and K. Yamamoto, "Impact of carrier recombination on fill factor for large area heterojunction crystalline silicon solar cell with 25.1% efficiency," *Appl. Phys. Lett.*, vol. 107, no. 23, p. 233506, Dec. 2015, doi: 10.1063/1.4937224.

[156] E. Fortunato, D. Ginley, H. Hosono, and D. C. Paine, "Transparent conducting oxides for photovoltaics," *MRS Bull.*, vol. 32, no. 3, pp. 242–247, 2007, doi: 10.1557/mrs2007.29.

[157] A. Cruz *et al.*, "Effect of front TCO on the performance of rear-junction silicon heterojunction solar cells: Insights from simulations and experiments," *Sol. Energy Mater. Sol. Cells,* vol. 195, pp. 339–345, Jun. 2019, doi: 10.1016/j.solmat.2019.01.047.

[158] W. R. Fahrner, "Amorphous silicon / crystalline silicon heterojunction solar cells," *SpringerBriefs Appl. Sci. Technol.*, no. 9783642370380, pp. 1–97, 2013, doi: 10.1007/978-3-642-37039-7_1.

[159] H. Park *et al.*, "Front and Back TCO Research Review of a-Si/c-Si Heterojunction with Intrinsic Thin Layer (HIT) Solar Cell," *Trans. Electr. Electron. Mater.*, vol. 19, pp. 165–172, 2018, doi: 10.1007/s42341-018-0026-8.

[160] L. Kerkache, A. Layadi, E. Dogheche, and D. Rémiens, "Physical properties of RF sputtered ITO thin films and annealing effect," *J. Phys. D. Appl. Phys.*, vol. 39, no. 1, p. 184, Dec. 2005, doi: 10.1088/0022-3727/39/1/027.

[161] H. H. Berger, "Contact Resistance and Contact Resistivity," *J. Electrochem. Soc.*, vol. 119, no. 4, p. 507, 1972, doi: 10.1149/1.2404240.

[162] D. Turkay, K. Tsoi, E. Donercark, R. Turan, and S. Yerci, "Spreading resistance modeling for rapid extraction of contact resistivity with a four-point probe," *Sol. Energy Mater. Sol. Cells,* vol. 230, p. 111272, Sep. 2021, doi: 10.1016/J.SOLMAT.2021.111272.

[163] E. Özkol, “Modeling and optimization of PECVD processes and equipment used for manufacturing thin film photovoltaic devices,” 2014, Accessed: Sep. 19, 2021. [Online]. Available: https://open.metu.edu.tr/handle/11511/24328.

[164] S. Güler, “Characterization and contact resistivity studies of ito thin films for use in silicon heterojunction solar cells,” Middle East Technical University, 2020.

[165] T. Pisarkiewicz, K. Zakrzewska, and E. Leja, “Scattering of charge carriers in transparent and conducting thin oxide films with a non-parabolic conduction band,” *Thin Solid Films*, vol. 174, no. PART 1, pp. 217–223, 1989, doi: 10.1016/0040-6090(89)90892-4.

[166] H. C. Lee and O. O. Park, “Behaviors of carrier concentrations and mobilities in indium-tin oxide thin films by DC magnetron sputtering at various oxygen flow rates,” *Vacuum*, vol. 77, no. 1, pp. 69–77, Dec. 2004, doi: 10.1016/j.vacuum.2004.08.006.

[167] Z. C. Holman *et al.*, “Current losses at the front of silicon heterojunction solar cells,” *IEEE J. Photovoltaics*, vol. 2, no. 1, pp. 7–15, 2012, doi: 10.1109/JPHOTOV.2011.2174967.

[168] J. Schube *et al.*, “Low-Resistivity Screen-Printed Contacts on Indium Tin Oxide Layers for Silicon Solar Cells with Passivating Contacts,” *IEEE J. Photovoltaics*, vol. 8, no. 5, pp. 1208–1214, Sep. 2018, doi: 10.1109/JPHOTOV.2018.2859768.

[169] J. Haschke *et al.*, “Annealing of Silicon Heterojunction Solar Cells: Interplay of Solar Cell and Indium Tin Oxide Properties,” *IEEE J. Photovoltaics*, vol. 9, no. 5, pp. 1202–1207, Sep. 2019, doi: 10.1109/JPHOTOV.2019.2924389.

[170] H. H. Berger, “Contact Resistance and Contact Resistivity,” *J. Electrochem. Soc.*, vol. 119, no. 4, p. 507, Apr. 1972, doi: 10.1149/1.2404240.

[171] G. Nogay *et al.*, “Nanocrystalline Silicon Carrier Collectors for Silicon Heterojunction Solar Cells and Impact on Low-Temperature Device Characteristics,” *IEEE J. Photovoltaics*, vol. 6, no. 6, pp. 1654–1662, Nov. 2016, doi: 10.1109/JPHOTOV.2016.2604574.

[172] L. Neusel, M. Bivour, and M. Hermle, “Selectivity issues of MoOx based hole contacts,” *Energy Procedia*, vol. 124, pp. 425–434, Sep. 2017, doi: 10.1016/J.EGYPRO.2017.09.268.

[173] J. Bullock *et al.*, “Efficient silicon solar cells with dopant-free asymmetric heterocontacts,” 2016, doi: 10.1038/NENERGY.2015.31.

APPENDICES

A. The Density of States for Simulation

The DOS distribution in the band gap is shown in Figure A.1 for different a-Si:H layers and input parameters of DOS are given in Table A.1. Moreover, the interface DOS and input parameters are given in Figure A.2 and Table A.2, respectively.

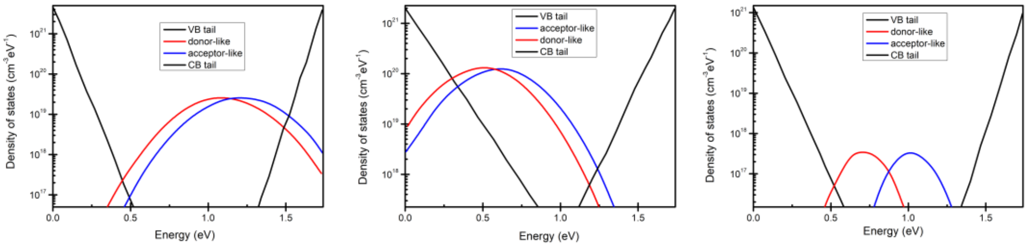

Figure A. 1. Density of states in n-aSi:H (a), p-aSi:H (b) and i-aSi:H (c).

Table A. 1. Defined parameters for DOS.

Characteristic energy (ev) for donors and acceptors	0.045-0.037	0.35-0.05	0.94-0.68
Capture cross-section for donor states, e, h (cm^2)	7x10^{-16}	1x10^{-12}	7x10^{-16}
Capture cross-section for acceptor states, e, h (cm^2)	7x10^{-16}	1x10^{-14}	7x10^{-16}
Defect DOS at Gaussian peak energy (eV)	1x10^{-16}-1x10^{-18}	1x10^{-15}-1x10^{-17}	1x10^{-17}-3x10^{-19}
Standard deviation (eV)	1.2-0.21	0.725-1.025	0.5-0.21
Capture cross-section for donor states, e, h (cm^2)	3x10^{-15}, 3x10^{-14}	1x10^{-12}, 1x10^{-14}	3x10^{-15}, 3x10^{-14}
Capture cross-section for acceptor states, e, h (cm^2)	3x10^{-15}, 3x10^{-14}	1x10^{-12}, 1x10^{-12}	3x10^{-15}, 3x10^{-14}

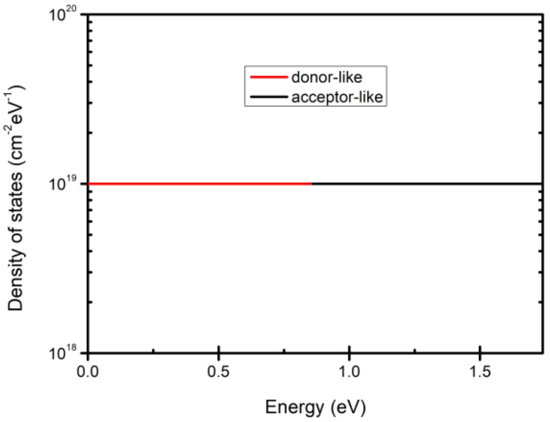

Figure A.2. The DOS distribution between c-Si and a-Si:H layer at the interface.

Table A. 2. Input parameters for interface DOS.

Parameters	i-aSi:H/c-Si
Capture cross-section for donor states, e,h (cm^2)	1x10^{-12},1x10^{-14}
Capture cross-section for acceptor states, e,h (cm^2)	1x10-12,1x10^{-12}

B. Screen Designs

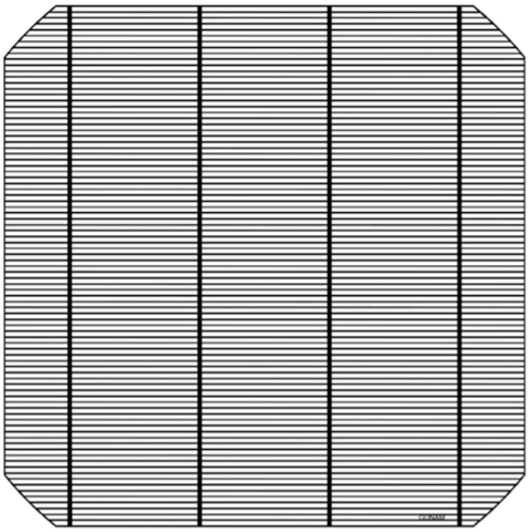

# of busbars: 4
# of fingers: 89
finger width: 35um
busbar width: 0.9mm
distance btw fingers: 1.75mm

Figure B 1. Industrial H-grid screen design.

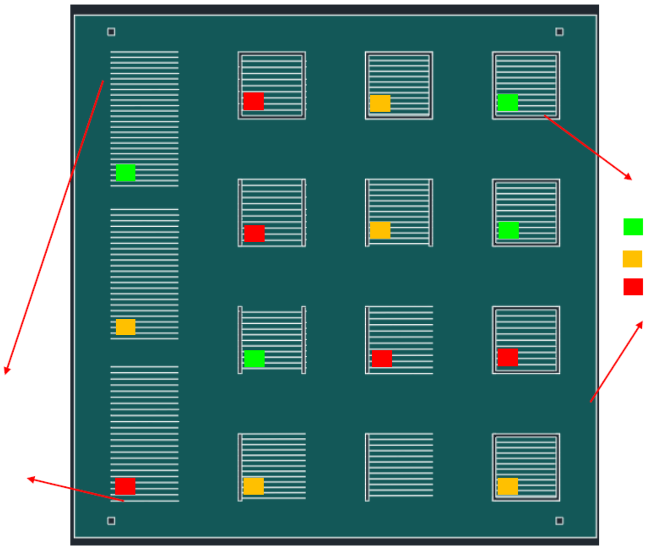

2x2 cm test cell :
🟩 -pitch 0: 1.35 mm
🟨 -pitch 1: 1.54 mm
🟥 -pitch 3 : 1.75mm

TLM patterns :
🟩 -pitch 0: 1.35 mm
🟨 -pitch 1: 1.54 mm
🟥 -pitch 3 : 1.75mm

Figure B 2. Small size screen design.

CURRICULUM VITAE

PERSONAL INFORMATION

Surname, Name: Dönerçark, Ergi
Nationality: Turkish (TC)
Date and Place of Birth: 21 April 1989, Ankara
Adress: ODTÜ-GÜNAM, Department of Physics, Middle East Technical University, Ankara/TURKEY
Phone: +90 543 930 8873
e-mail: ergi@metu.edu.tr

EDUCATION

Degree	**Institution**	**Year of Graduation**
MS	METU Physics	2017
BS	METU Physics	2013
High School	Işıklar Military	2007

WORK EXPERIENCE

Year	**Place**	**Enrollment**
2021-Present	ODTÜ - GÜNAM	Team Leader
2016 – 2021	GÜNAM, METU	Scientific Project Specialist
2014 – 2016	GÜNAM, METU	Project Scholar
2014 – 2015	imec	Project Scholar
2011 August	Eldaş Test ve Kalibrasyon Laboratuvarı	Intern Student

FOREIGN LANGUAGES

Advanced English

PUBLICATIONS

Articles

1. **E. Dönerçark**, A. Salimi, E.H. Çiftpınar, M. Koç, R. Turan,” Improved device performance of silicon heterojunction solar cells by application of wide band gap p-aSiCx:H.”, (manuscript under preparation).
2. **E. Dönerçark**, T. Çolakoğlu, M. Terlemezoğlu, M.K. Abak, E.H. Çiftpınar, A. Bek, R. Turan, “Formation of tetragonal-star-shaped inverted pyramids on p-type silicon for solar cell application.”, (manuscript under preparation).
3. **E. Dönerçark**, S. Güler, E.H. Çiftpınar, I. Kabaçelik, M. Koç, A.C. Erçelebi, R. Turan,”Impact of oxygen partial pressure during indium tin oxide sputtering on the performance of silicon heterojunction solar cells.”, (manuscript submitted to Materials Science & Engineering B).
4. E.H. Çiftpınar, **E. Dönerçark**, S.H. Sedani, R. Turan,” A Study on contamination detection and trace for various cell structures fabricated in clean room environment.”, (manuscript submitted to Applied Surface Science).
5. **E. Dönerçark**, S.H. Sedani, I. Kabaçelik, A. Salimi, R. Turan, “ Interface and material properties of wide band gap a-SiCx:H thin films for solar cell applications.”, (manuscript submitted to Renewable Energy).
6. D. Turkay, K. Tsoi, **E. Donercark**, R. Turan, S. Yerci, “Spreading Resistance Modeling for Contact Resistivity Extraction in Ohmic Multilayer Structures With Circular Electrodes.”, IEEE Trans. Electron Devices. (2021) 1–8. https://doi.org/10.1109/TED.2021.3117187.
7. D. Türkay, K. Tsoi, **E. Dönerçark**, R. Turan, and S. Yerci, “Spreading resistance modeling for rapid extraction of contact resistivity with a four-point probe,” *Sol. Energy Mater. Sol. Cells*, vol. 230, p. 111272, Sep. 2021.

8. M. Ünal, Z. Demircioğlu, **E. Dönerçark**, E. Özkol, and R. Turan, "Aluminum induced texturing of sandy and prism glasses: Combination of micro/nano texture with macro texture," *Phys. status solidi*, vol. 214, no. 8, p. 1600856, Aug. 2017.

Conference Presentations

1. D. Türkay, K. Tsoi, **E. Dönerçark**, R. Turan, S. Yerci, "Spreading resistance modeling for rapid extraction of contact resistivity with a four-point probe" *Oral presentation*, MRS Fall Meeting, Boston, USA, 2021.
2. **E. Dönerçark**, E. H. Çiftpınar, M. Terlemezoğlu, T. Çolakoğlu, and R. Turan, "A Study on Tetragonal-star Like Shaped Inverted Pyramid Texturing," *Oral presentation*, 48th IEEE Photovoltaic Specialists Conference, virtual meeting, 2021.
3. B. Altınsoy, **E. Dönerçark**, A. Aliefendioğlu, and R. Turan, "Single Step Inverted Pyramid Texturing of n-type Silicon by Copper Assisted Chemical Etching," 48th IEEE Photovoltaic Specialists Conference, virtual meeting, 2021 (*best poster award*).
4. **E. Dönerçark**, H. Nasser, E.H. Çiftpınar, A. Salimi, R. Turan, " Formation of wide band gap emitters for silicon heterojunction solar cells" 8th SiliconPV, virtual meeting, 2021.
5. **E. Dönerçark**, S. Güler, E. H. Çiftpınar, I. Kabaçelik, and R. Turan, "Enhanced Passivation Properties of a-Si:H and Reactive ITO Sputtering for SHJ Solar Cells," 47th IEEE Photovoltaic Specialists Conference, virtual meeting, 2020.
6. **E. Dönerçark**, I. Kabaçelik, A. Salimi, S.H. Sedani, R. Turan, "Wide band gap a-SiCx:H passivation layer for the application of silicon heterojunction solar cells," International Conference on Photovoltaic Science and Technologies PVCON, Ankara, Turkey, 2020.
7. S.H. Sedani, **E. Dönerçark**, E.H. Çiftpınar, R. Turan, "Tailored doping profile with commercial nanosecond laser for low-cost PV industrial

applications," International Conference on Photovoltaic Science and Technologies PVCON, Ankara, Turkey, 2020.

8. E.H. Çiftpınar, **E. Dönerçark**, S.H. Sedani, R. Turan, "A study on contamination detection and trace for various cell structures fabricated in clean room environment," International Conference on Photovoltaic Science and Technologies PVCON, Ankara, Turkey, 2020.
9. **E. Dönerçark,** E.H. Çiftpınar, H. Nasser, A. Salimi, I. Kabaçelik, R. Turan, "Bifacial silicon hetero-contact solar cells," *Oral presentation*, International Conference on Photovoltaic Science and Technologies PVCON, Ankara, Turkey, 2020.
10. K. Tsoi, D. Türkay, **E. Dönerçark**, E.H. Ciftpinar, M. Ghasemi, R. Turan, S. Yerci, "Heterojunction silicon solar cells incorporating unpatterned MoOx and LiFx/Al op wet-chemically processed silicon surfaces," 37th EU PVSEC Lisbon, Porugal, 2020.
11. S. Güler, **E. Dönerçark**, A.E. Aytaç, A.Ç. Erçelebi, R. Turan, "Optimization studies on the material properties of ITO as window layer for silicon heterojunction solar cells", 36th EU PVSEC, Marseille, France, 2019.
12. **E. Dönerçark**, B. İmer, R. Turan, "Post-annealing Temperature Effect on Electrical Properties of Al_2O_3 Films on Silicon by Atomic Layer Deposition for Solar Cell Applications," *Oral presentation*, MRS Fall Meeting, Massachusetts, Boston, USA, 2018.
13. **E. Dönerçark**, T. Çolakoğlu, M. Terlemezoğlu, M.K. Abak, A. Bek, R. Turan "Wet Chemical Surface Finishing for Lithography-Free Inverted Pyramids," 35th EU PVSEC Brussels, Belgium, 2018.
14. A.E. Aytaç, G. Kökbudak, **E. Dönerçark**, R. Turan, "Enhanced Pasivation Quality of Crystallized Doped Amorphous Silicon Layer with Wet Chemical Oxide," 35th EU PVSEC, Brussels, Belgium, 2018.
15. S.H. Sedani, **E Dönerçark**, N. Avishan, A.E. Aytaç, I.M. Öztürk, A. Bek, R. Turan, "Aluminum Induced Laser Crystallization of Thin Amorphous

Silicon," International Conference on Photovoltaic Science and Technologies PVCON, Ankara, Turkey, 2018.

16. **E. Dönerçark**, A.E. Aytaç, F. Sarıhan, M. Aldemir, M. Atmaca, S. Görmez, E. Arıkan, A.Ç. Besen, R. Turan, "Characterization of a-Si:H Passivation Layer with Photoluminescence Imaging Technique in Heterojunction Solar Cells Production Flow," International Conference on Photovoltaic Science and Technologies PVCON, Ankara, Turkey, 2018.
17. A.E. Aytaç, **E. Dönerçark**, R. Turan, "Passivated Tunneling Oxide Layer with p-type Poly Silicon," International Conference on Photovoltaic Science and Technologies PVCON, Ankara, Turkey, 2018.
18. **E. Dönerçark**, T. Çolakoğlu, M. Terlemezoğlu, M.K. Abak, A. Bek, R. Turan,"Single Step Lithography Free Inverted Pyramids," *Oral presentation*, International Conference on Photovoltaic Science and Technologies PVCON, Ankara, Turkey, 2018.
19. K. Çınar, S.H. Sedani, **E. Dönerçark**, N. Avishan, A.E. Aytaç, A. Bek, "Laser Crystallization of Si Thin Film via Pulsed IR Laser for Ultra-Thin Crystalline Solar Cells," International Conference on Photovoltaic Science and Technologies PVCON, Ankara, Turkey, 2018 (*best poster award*).
20. F. Sarıhan, **E. Dönerçark**, M. Atmaca, S. Görmez, E. Arıkan, A.Ç. Besen, R. Turan, "Simulation of a-S:H/c-Si Heterojunction Solar Cel*ls*," International Conference on Photovoltaic Science and Technologies PVCON, Ankara, Turkey, 2018.
21. **E. Dönerçark**, T. Çolakoğlu, M.K. Abak, M. Terlemezoğlu, A. Bek, R. Turan, "Enhanced Optical Properties of Lithography Free Inverted Pyramids with Tetragonal Star Shape Surface Morphology," 8th SiliconPV, Lausanne, Sweden, 2018.
22. **E. Dönerçark**, R. Turan, "Enhanced Passivation Quality of Intrinsic Amorphous Silicon by Hydrogen Plasma for Silicon Heterojunction Solar Cell Application," E-MRS Spring, Strasbourg, France, 2017.

Projects

1. Türkiye Fotovoltaik Teknolojileri Platformu (2021-present) - Scholar
2. Tubitak Joint Research Project - Advanced Heterojunction Si Solar Cells with SiC and Metal Oxides Thin Films - SiMOX (2018-2020).
3. Amorf Si and doping free selective heterojunction (Mositix)" (2018-2020) – Scholar.
4. Fabrication of Crystalline Silicon Bifacial Heterojunction Solar Cell and Prototype Glass to Glass Module (2017-2019) – Researcher.
5. Smart PV Skin: Grid-Non-Planar Photovoltaic Systems (2016-2017) - Scientific Project Specialist.
6. Fotovoltaik Enerji Sistemleri için Nano Ölçekte Desenlenmiş Üstün Performans Camların Geliştirilmesi (2014 – 2016) - Scholar.